

# **ANALYSIS OF RESISTIVE-VEE DIPOLE ANTENNAS FOR PRODUCING POLARIZATION DIVERSITY**

A Dissertation  
Presented to  
The Academic Faculty

By

James William Sustman

In Partial Fulfillment  
of the Requirements for the Degree  
Doctor of Philosophy  
in  
Electrical and Computer Engineering



School of Electrical and Computer Engineering  
Georgia Institute of Technology  
August 2014

Copyright © 2014 by James William Sustman

Report Documentation Page		Form Approved OMB No. 0704-0188
Public reporting burden for the collection of information is estimated to average 1 hour per response, including the time for reviewing instructions, searching existing data sources, gathering and maintaining the data needed, and completing and reviewing the collection of information. Send comments regarding this burden estimate or any other aspect of this collection of information, including suggestions for reducing this burden, to Washington Headquarters Services, Directorate for Information Operations and Reports, 1215 Jefferson Davis Highway, Suite 1204, Arlington VA 22202-4302. Respondents should be aware that notwithstanding any other provision of law, no person shall be subject to a penalty for failing to comply with a collection of information if it does not display a currently valid OMB control number.		
1. REPORT DATE <b>01 AUG 2014</b>	2. REPORT TYPE <b>Final</b>	3. DATES COVERED <b>1 Aug 2010 - 31 Dec 2016</b>
4. TITLE AND SUBTITLE <b>Analysis of Resistive-Vee Dipole Antennas for Producing Polarization Diversity / PhD Dissertation</b>		5a. CONTRACT NUMBER <b>N/A</b>
		5b. GRANT NUMBER <b>N00014-10-1-0958</b>
		5c. PROGRAM ELEMENT NUMBER <b>N/A</b>
6. AUTHOR(S) <b>James W. Sustman Electrical &amp; Computer Engineering Georgia Institute of Technology</b>		5d. PROJECT NUMBER <b>N/A</b>
		5e. TASK NUMBER <b>N/A</b>
		5f. WORK UNIT NUMBER <b>N/A</b>
7. PERFORMING ORGANIZATION NAME(S) AND ADDRESS(ES) <b>School of Electrical and Computer Engineering Georgia Institute of Technology 777 Atlantic Drive NW Atlanta, GA 30332-0250</b>		8. PERFORMING ORGANIZATION REPORT NUMBER <b>63</b>
9. SPONSORING/MONITORING AGENCY NAME(S) AND ADDRESS(ES) <b>Office of Naval Research (ONR) 875 North Randolph Street - Suite 1425 Code 03R Arlington, VA 22203-1995</b>		10. SPONSOR/MONITOR'S ACRONYM(S) <b>ONR</b>
		11. SPONSOR/MONITOR'S REPORT NUMBER(S) <b>N/A</b>
12. DISTRIBUTION/AVAILABILITY STATEMENT <b>Approved for public release, distribution unlimited</b>		
13. SUPPLEMENTARY NOTES <b>N/A, The original document contains color images.</b>		

## 14. ABSTRACT

This thesis presents a new dual circularly polarized antenna for ground penetrating radar applications. The new antenna design uses four crossed Resistive-Vee Dipoles (RVD) operating in bistatic mode to measure multiple polarizations. The antenna system is able to distinguish radially symmetric and linear targets with its ability to transmit right-hand circularly polarized (RHCP) fields and receive both left-hand circularly polarized (LHCP) and RHCP scattered fields. The type of target can be identified by comparing the relative amplitudes of the received LHCP fields and RHCP fields. For example, linear targets such as wires may be identified by equal amounts of scattered LHCP and RHCP fields. Numerical modeling was used to optimize the arrangement of the four RVDs in the RVD-based CP antenna to have low coupling and good circular polarization at close range. The resulting antenna design is shown to be very effective at finding buried wire targets without being costly. Additional modeling was performed to improve the circular polarization by changing the arm shape and resistive profile of the RVDs. Three methods are developed for estimating the spatial orientation angle of a detected wire target. The first method involves synthesizing transmission and reception of linear polarization at many angles to find the angle that matches the angle of the wire target. The second and third methods involve directly computing the angle of the wire target from the phase difference in the co-polarization and cross-polarization responses. All three methods provide accurate estimates. The RVD-based CP antenna enables strong detection of subsurface targets along with geometry-based classification of targets. The RVD-based CP antenna is well suited for finding buried wires and rejecting miscellaneous clutter that may be present in the ground.

## 15. SUBJECT TERMS

## 16. SECURITY CLASSIFICATION OF:

a. REPORT  
**unclassified**

b. ABSTRACT  
**unclassified**

c. THIS PAGE  
**unclassified**

17. LIMITATION  
OF ABSTRACT  
**SAR**

18. NUMBER  
OF PAGES  
**199**

19a. NAME OF  
RESPONSIBLE PERSON

# **ANALYSIS OF RESISTIVE-VEE DIPOLE ANTENNAS FOR PRODUCING POLARIZATION DIVERSITY**

Approved by:

Dr. Greg Durgin, Committee Chair  
*Professor, School of ECE*  
*Georgia Institute of Technology*

Dr. James McClellan  
*Professor, School of ECE*  
*Georgia Institute of Technology*

Dr. Waymond R. Scott Jr., Advisor  
*Professor, School of ECE*  
*Georgia Institute of Technology*

Dr. Albert Sheffer  
*Principle Research Scientist, GTRI*  
*Georgia Institute of Technology*

Dr. Andrew Peterson  
*Professor, School of ECE*  
*Georgia Institute of Technology*

Date Approved: August 2014

*To my parents, **James E. Sustman and Dr. Jane T. St. Clair**  
and my brothers, **Edward A. Sustman and George F. Sustman***

## ACKNOWLEDGMENTS

I would like to acknowledge my research advisor, Prof. Waymond R. Scott, Jr. I appreciate his guidance, his insights, and help through all of my research. He has made many helpful suggestions for my work.

I would like to thank my thesis committee members Dr. Gregory Durgin, Dr. Andrew Peterson, Dr. James McClellan, and Dr. Albert Sheffer. I would also like to acknowledge my fellow researchers in the Electromagnetics Lab, Michael McFadden, Mu-Hsin Wei, Yoni Gabbay, Mark Reed and Ricardo Lopez. Their wisdom, advice, and generosity have greatly helped me and my research.

I would like to acknowledge the support of my friends, especially Curtis Roe and Matt Hobbs.

I am very thankful for my parents, James E. Sustman and Dr. Jane T. St. Clair. They have been very encouraging and are responsible for much of my success. I would like to thank my brothers Edward and George. I especially thank Edward for his support and valuable advice. I would like to thank my sister-in-law, Anne Michael, for all of her thoughtfulness and generosity.

This work is supported in part by the U.S. Office of Naval Research as a Multi-disciplinary University Research Initiative on Sound and Electromagnetic Interacting Waves under grant number N00014-10-1-0958, in part by the US Army REDCOM CERDEC Night Vision and Electronic Sensors Directorate, Science and Technology Division, Countermeasure Branch and in part by the U. S. Army Research Office under grant number W911NF-11-1-0153.

# TABLE OF CONTENTS

<b>ACKNOWLEDGMENTS</b> . . . . .	iv
<b>LIST OF TABLES</b> . . . . .	vii
<b>LIST OF FIGURES</b> . . . . .	viii
<b>SUMMARY</b> . . . . .	1
<b>CHAPTER 1 INTRODUCTION</b> . . . . .	2
1.1 Synthesis of Circular Polarization . . . . .	3
1.2 Existing Circular Polarization GPR Technologies . . . . .	4
1.2.1 Crossed-Dipole Antennas . . . . .	4
1.2.2 Dual CP Bow-tie Antennas . . . . .	6
1.2.3 Dual CP Vivaldi Antennas . . . . .	7
1.2.4 Sinuous Antennas . . . . .	7
1.2.5 Spiral Antennas . . . . .	8
1.3 Proposed Circular Polarization GPR System . . . . .	10
1.4 Outline . . . . .	15
<b>CHAPTER 2 NUMERICAL MODELING FOR THE DUAL CP ANTENNA</b> .	17
2.1 Optimization of RVD Configuration . . . . .	17
2.1.1 Physical Interference . . . . .	17
2.1.2 Coupling . . . . .	19
2.2 Modeling of Targets in Free Space . . . . .	22
2.2.1 False Color Map Representation . . . . .	34
<b>CHAPTER 3 EXPERIMENTAL RESULTS FOR THE DUAL CP ANTENNA</b>	43
3.1 Targets in Air . . . . .	45
3.1.1 Wire Targets and Loop . . . . .	46
3.1.2 Metal Sphere Target . . . . .	48
3.2 Targets in Ground . . . . .	49
3.2.1 Wire and Loop Targets . . . . .	50
3.2.2 Metal Sphere Target . . . . .	53
3.3 Targets in Ground with Clutter . . . . .	55
3.3.1 Buried Sphere . . . . .	55
3.3.2 Buried Rocks . . . . .	59
3.3.3 Buried Wooden Board . . . . .	63
3.3.4 Buried Aluminum Can . . . . .	67
3.3.5 Buried Land mine . . . . .	70
3.3.6 Summary . . . . .	72
3.4 Wire Thickness Analysis . . . . .	74
3.5 Ground Surface Roughness Analysis . . . . .	80

<b>CHAPTER 4</b>	<b>RVD IMPROVEMENT FOR OFF-BORESIGHT CP</b>	88
4.1	RVD Reshaping	89
4.2	Resistive Profile Analysis	95
4.3	Numerical Results of Dual CP Antenna with Improved RVD	102
4.4	Experimental Results from Improved RVD	106
4.4.1	Targets in Air with Improved RVD	109
4.4.2	Buried Targets with Improved RVD	113
4.5	Alternate Cross-Polarization Calculation	116
<b>CHAPTER 5</b>	<b>WIRE TARGET ORIENTATION ANGLE ESTIMATION</b>	123
5.1	Linear Polarization Sweep Method	123
5.1.1	Numerical Results	125
5.1.2	Experimental Results	127
5.2	Dual CP Phase Comparison Method	130
5.2.1	Numerical Results	131
5.2.2	Experimental Results	134
5.3	Instantaneous Phase Method	137
5.3.1	Numerical Results	138
5.3.2	Experimental Results	140
5.4	Method Comparison	143
<b>CHAPTER 6</b>	<b>RESISTIVELY LOADED MODULATED SCATTERERS</b>	144
6.1	Modulated Scatterer Design Optimization	146
6.1.1	Measurement Setup	152
6.1.2	Resolving Time-Domain Reflected Signal	153
6.2	Experimental Results	156
6.2.1	Biasing Network Analysis	156
6.2.2	Thin Substrate RLMS	157
6.2.3	Resistive Vee Dipole Analysis	159
6.2.4	Ground Penetrating Radar Hydrology Analysis	161
6.3	RLMS Measurements with the RVD-based CP Antenna	165
6.3.1	RLMS in Air	166
6.3.2	RLMS in Ground	169
<b>CHAPTER 7</b>	<b>CONCLUSIONS</b>	172
<b>REFERENCES</b>		175
<b>VITA</b>		183



## LIST OF TABLES

Table 1	Resistance values (in Ohms) for resistors along the RVD arms of the optimized and Kim RVDs. . . . .	107
Table 2	Average angle estimate errors for the three angle estimation methods. . .	143
Table 3	Chosen resistor values and resistor positions along the arms for the RLMS.	151

## LIST OF FIGURES

Figure 1	A diagram of orthogonal linearly polarized antennas for producing circular polarization. . . . .	4
Figure 2	A diagram of a crossed-dipole antenna. . . . .	5
Figure 3	A diagram of a bow-tie antenna. . . . .	6
Figure 4	A diagram of a Vivaldi antenna. . . . .	7
Figure 5	A diagram of a bistatic dual CP target detection. . . . .	9
Figure 6	A photograph of the Resistive-Vee Dipole (RVD) antenna. . . . .	11
Figure 7	Diagram of the four resistive-vee dipole antenna setup for transmitting and receiving circularly polarized radiation. . . . .	11
Figure 8	A diagram showing the effects of $P_1$ and $P_2$ on the RVD configuration. .	18
Figure 9	Contour graph of minimum distance (in meters) between points on adjacent RVDs versus $P_1$ and $P_2$ . . . . .	19
Figure 10	Antenna coupling strength in dB versus antenna positions. . . . .	21
Figure 11	Coupling strength in dB versus antenna separation. $S_{21}$ , the measurement between a parallel pair of antennas, is shown on the solid line. $S_{23}$ , the measurement between an orthogonal pair of antennas, is shown on the dashed line. . . . .	22
Figure 12	A 2-dimensional top-down view of the antenna geometry. . . . .	22
Figure 13	Antenna time-domain responses from a horizontally oriented 10 cm long straight wire target. The wire was moved from 0.5 cm in front of the RVD-based CP antenna to 10 cm in front of the antenna in 0.5 cm steps. The bottom curve on each figure corresponds to a wire distance of 0.5 cm, and each subsequent curve corresponds to a wire distance 0.5 cm farther than the curve beneath it. . . . .	24
Figure 14	Antenna time-domain responses from a 5 cm diameter circular loop target. The loop was moved from 0.5 cm in front of the antennas to 10 cm in front of the antennas in 0.5 cm steps. The bottom curve on each figure corresponds to a loop distance of 0.5 cm, and each subsequent curve corresponds to a wire distance 0.5 cm farther than the curve beneath it. .	25

Figure 15	Received signal strength from a $0^\circ$ wire. Co-polarized signal strength is shown in Figure 15a. Cross-polarized signal strength is shown in Figure 15b. The wire was positioned 10 cm in front of the RVDs in the minus Z-direction. The wire was then moved in the X-Y plane. At each position the received signal strength is given in dB. . . . .	27
Figure 16	The difference between Figures 15a and 15b. . . . .	28
Figure 17	Received signal strength from a $22.5^\circ$ wire. Co-polarized signal strength is shown in Figure 15a. Cross-polarized signal strength is shown in Figure 15b. The wire was positioned 10 cm in front of the RVDs in the minus Z-direction. The wire was then moved in the X-Y plane. At each position the received signal strength is given in dB. . . . .	29
Figure 18	The difference between Figures 17a and 17b. . . . .	30
Figure 19	Received signal strength from a $45^\circ$ wire. Co-polarized signal strength is shown in Figure 19a. Cross-polarized signal strength is shown in Figure 19b. The wire was positioned 10 cm in front of the RVDs in the minus Z-direction. The wire was then moved in the X-Y plane. At each position the received signal strength is given in dB. . . . .	31
Figure 20	The difference between Figures 19a and 19b. . . . .	32
Figure 21	Received signal strength from a circular wire loop. Co-polarized signal strength is shown in Figure 21a. Cross-polarized signal strength is shown in Figure 21b. The loop was positioned 10 cm in front of the RVDs in the minus Z-direction. The loop was then moved in the X-Y plane. At each position the received signal strength is given in dB. . . . .	33
Figure 22	The difference between Figures 21a and 21b. . . . .	34
Figure 23	A key for the false color map showing how a ratio of co-polarization to cross-polarization affects the resulting polarization and color. . . . .	37
Figure 24	Numerical results for wire targets rotated $0^\circ$ , $22.5^\circ$ and $45^\circ$ , as well as a loop target. The left-most column figures are the co-polarized signals in dB. The center column figures are the cross-polarized signals in dB. The right-most column figures are the false color mapped signals. . . . .	40
Figure 25	Examples of normal, Hilbert transform, and enveloped signals. These examples are from measurements of a wire target in air. . . . .	41
Figure 26	False color maps indicating the detection of targets. White indicates that no target is detected, blue indicates that a linear type of target has been detected, and red indicates that a radially symmetric type of target has been detected. . . . .	42

Figure 27	Photograph of the RVD-based circularly polarized antenna. . . . .	43
Figure 28	Photograph of the setup for the air experiments. . . . .	45
Figure 29	Results for scans over targets in air. The first column of figures has pseudocolor graphs in dB for the co-polarization responses. The second column of figures has pseudocolor graphs in dB for the cross-polarization responses. The third column of figures has false color maps. . . . .	47
Figure 30	False color maps for a $0^\circ$ wire, a $22.5^\circ$ wire, a $45^\circ$ wire, and circular wire loop that were scanned in air. . . . .	48
Figure 31	Results for scans over the metal sphere target in air. . . . .	49
Figure 32	False color map for a metal sphere target in air. . . . .	49
Figure 33	Results for scans over targets in the ground. The first column of figures has pseudocolor graphs in dB for the co-polarization responses. The second column of figures has pseudocolor graphs in dB for the cross-polarization responses. The third column of figures has false color maps. . . . .	51
Figure 34	Results for scans over targets in the ground in the X-direction. . . . .	52
Figure 35	False color maps for a $0^\circ$ wire, a $22.5^\circ$ wire, a $45^\circ$ wire, and circular wire loop that were scanned in the ground. . . . .	53
Figure 36	Results for scans over the metal sphere target in the ground. . . . .	54
Figure 37	Y-direction scan over the buried loop target. . . . .	54
Figure 38	False color map for a metal sphere target in the ground. . . . .	55
Figure 39	A photograph of a metal sphere used in the clutter experiments. . . . .	56
Figure 40	A diagram for the buried sphere and wire experiment. . . . .	57
Figure 41	Results for scans over the sphere and wire targets in the ground. . . . .	57
Figure 42	A diagram for the experiment with multiple buried spheres and wires. . . . .	58
Figure 43	Results for scans over the sphere targets and wire targets buried together in the ground. . . . .	58
Figure 44	A photograph of a rock used in the clutter experiments. . . . .	59
Figure 45	Results for scans over the rock target in the ground. . . . .	60
Figure 46	False color map for a rock target in the ground. . . . .	60
Figure 47	A diagram for the buried rock and wire experiment. . . . .	61

Figure 48	Results for scans over the single rock target and wire target together in the ground. . . . .	61
Figure 49	A diagram for the experiment with multiple buried rocks and wires. . . .	62
Figure 50	Results for scans over the multiple rock targets and wire targets buried together in the ground. . . . .	62
Figure 51	A diagram for the experiment with multiple buried rocks but without the wires. . . . .	63
Figure 52	Results for scans over the multiple rock targets without the wire targets. .	63
Figure 53	A photograph of a wooden block used in the clutter experiments. . . . .	64
Figure 54	Results for scans over the wooden block target in the ground. . . . .	65
Figure 55	Results for scans over the wooden block target in the ground. The narrow side of the wooden block was facing upwards towards the antenna. . . . .	66
Figure 56	A diagram for the buried wooden block and wire experiment. . . . .	66
Figure 57	Results for scans over the wooden block and wire targets in the ground. .	67
Figure 58	A photograph of an aluminum can used in the clutter experiments. . . . .	67
Figure 59	Results for scans over the aluminum can target in the ground. . . . .	68
Figure 60	Results for scans over the aluminum can in the ground. The top of the can faced upwards towards the antenna. . . . .	69
Figure 61	A diagram for the buried can and wire experiment. . . . .	70
Figure 62	Results for scans over the aluminum can and wire targets in the ground. .	70
Figure 63	A photograph of a land mine used in the clutter experiments. . . . .	71
Figure 64	A diagram for the buried land mine and wire experiment. . . . .	71
Figure 65	Results for scans over the land mine and wire targets in the ground. . . .	72
Figure 66	Scatter plot of relative co-polarization and cross-polarization response strength for targets in air. . . . .	73
Figure 67	Scatter plot of relative co-polarization and cross-polarization response strength for targets in the ground. . . . .	74
Figure 68	Results for scans over the buried 30 Gauge wire target. . . . .	75
Figure 69	Results for scans over the buried 24 Gauge wire target. . . . .	76

Figure 70	Results for scans over buried cylinder targets. The first row of figures is from results for the 6.35 mm cylinder. The second row of figures is from results for the 9.53 mm cylinder. The third row of figures is from results for the 12.70 mm cylinder. . . . .	77
Figure 71	Results for scans over buried cylinder targets. The first row of figures is from results for the 19.05 mm cylinder. The second row of figures is from results for the 25.40 mm cylinder. The third row of figures is from results for the 38.10 mm cylinder. . . . .	78
Figure 72	Scatter plot of relative co-polarization and cross-polarization response strength for cylinder and wire targets. . . . .	79
Figure 73	Four photographs of the sand surface in the first surface roughness experiment. . . . .	81
Figure 74	Co-polarization and cross-polarization responses from the first surface roughness experiment. The wire target is aligned with the scanning lane. . . . .	82
Figure 75	False color maps of the first surface roughness experiment. The wire target runs across the width of the scanning area in the X-direction at approximately $Y = 0\text{ cm}$ . . . . .	83
Figure 76	Four photographs of the sand surface in the second surface roughness experiment. . . . .	84
Figure 77	Co-polarization and cross-polarization responses from the second surface roughness experiment. The wire target is aligned with the scanning lane. . . . .	85
Figure 78	False color maps of the second surface roughness experiment. The wire target runs across the width of the scanning area in the X-direction at approximately $Y = 0\text{ cm}$ . . . . .	86
Figure 79	S-parameter measurements of the second surface roughness experiment. . . . .	87
Figure 80	A diagram showing the parameters that define the geometry of the RVD. . . . .	89
Figure 81	A diagram of the optimized RVD shape. . . . .	92
Figure 82	Near fields for the optimized and old RVDs. . . . .	92
Figure 83	Metric values versus $z_0$ . The black curve uses a metric that compares field values with 25 cm of boresight, the green curve uses a metric that compares field values with 20 cm of boresight, the red curve uses a metric that compares field values with 15 cm of boresight, and the blue curve uses a metric that compares field values with 10 cm of boresight. . . . .	93

Figure 84	Numerical results for reshaped RVD scans of wire targets a loop target. The left-most column figures are the co-polarized signals in dB. The center column figures are the cross-polarized signals in dB. The right-most column figures are the false color mapped signals. . . . .	94
Figure 85	False color maps for the reshaped RVD scans of wire and loop targets. . .	95
Figure 86	Vector maps of the near field patterns based on the original Kim RVD. . .	97
Figure 87	Example rectangular pulses. The blue pulse has a width of 1 and a height of 1. The red pulse has a width of $\frac{1}{2}$ and a height of $\sqrt{2}$ . . . . .	100
Figure 88	A scatter plot of metric values for the candidate RVDs with $X_0 > X_{0kim} = 0.0037$ . The color of the circles on the scatter plot vary with $R_1$ , and the size of the circles vary with $z_0$ . The original Kim RVD is marked with the *. The reshaped RVD with the Kim resistive profile is marked by the square. . . . .	101
Figure 89	Time-domain pulses at boresight for the Kim RVD (blue) and the optimized RVD (red). . . . .	102
Figure 90	Co-polarization and cross-polarization contours for scans over a small loop target. Results are shown for both the Kim RVD and the optimized RVD. Contours are in dB. . . . .	103
Figure 91	Co-polarization to cross-polarization ratio contours for scans over a small loop target. . . . .	104
Figure 92	False color maps for scans over a small loop target. Red indicates a high co-polarization to cross-polarization ratio, and blue indicates a low co-polarization to cross-polarization ratio. . . . .	105
Figure 93	Radiation patterns for the optimized RVD and Kim RVD. Each RVD is directed in the negative-X direction. X-Z plane radiation patterns are in the first row. X-Y plane radiation patterns are in the second row. . . . .	105
Figure 94	Photograph of the optimized RVD. . . . .	106
Figure 95	Photograph of the optimized RVD CP antenna experimental setup. . . . .	107
Figure 96	Time-domain responses for scattering from the the optimized RVD and Kim RVD CP antennas. A metal plate target and the CP antenna back piece are shown for reference. . . . .	109
Figure 97	False Color Maps for 20 cm long wire targets at $0^\circ$ , $22.5^\circ$ and $45^\circ$ , as well as a 5 cm diameter loop target. The targets are measured in air. . . . .	111
Figure 98	False color maps of experimental 2D scans indicating the detection of targets in air. . . . .	112

Figure 99	False color maps for 20 cm long wire targets at $0^\circ$ , $22.5^\circ$ and $45^\circ$ , as well as a 5 cm diameter loop target. The targets were buried in the sand. .	114
Figure 100	False color maps from buried target experiments. . . . .	115
Figure 101	Scatter plot of metric values for the candidate RVDs with $X_0 > X_{0kim} = 0.0037$ . The color of the circles on the scatter plot vary with $R_1$ , and the size of the circles vary with $z_0$ . In Figure 101a the original method for computing the cross-polarization is used for calculating $M$ , and the RVD chosen with the alternate method is shown with the $X$ marker. In Figure 101b the alternate method for computing the cross-polarization is used, and the $X$ marks the RVD chosen with the original method. . . . .	117
Figure 102	Alternate cross-polarization contours for scans over a small loop target. Results are shown for both the Kim RVD and the optimized RVD. Contours are in dB. . . . .	118
Figure 103	Co-polarization to cross-polarization ratio contours for scans over a small loop target. The alternate cross-polarization calculation was used to produce the data. . . . .	119
Figure 104	False color maps for scans over a small loop target. This data uses the alternate cross-polarization calculation. Red indicates a high alternate cross-polarization to co-polarization ratio, and blue indicates a low alternate cross-polarization to co-polarization ratio. . . . .	120
Figure 105	Contour graphs for scans over a small loop target. These results are from the reciprocity model for the optimized RVD. The averaging method for calculating the co-polarization and cross-polarization is used. The top row of figures are in dB. . . . .	121
Figure 106	False color maps indicating the detection of targets obtained using the cross-polarization of Equation 39 and the co-polarization of Equation 41. White indicates that no target is detected, blue indicates that a linear type of target has been detected, and red indicates that a radially symmetric type of target has been detected. . . . .	122
Figure 107	A diagram for the LP sweep method. The transmitting and receiving antennas have both been rotated by $\phi$ . The linear target is at angle $\theta$ . . .	124
Figure 108	Orientation angle LP sweep estimates (in degrees) for wire targets from numerical results. . . . .	126
Figure 109	Orientation angle estimates for wire targets in air from experimental results. . . . .	128
Figure 110	Orientation angle estimates (in degrees) for wire targets under ground from experimental results. . . . .	129



Figure 111	Orientation angle phase comparison estimates (in degrees) for wire targets from numerical results. . . . .	133
Figure 112	Orientation angle phase comparison estimates (in degrees) for wire targets in air from experimental results. . . . .	135
Figure 113	Orientation angle phase comparison estimates (in degrees) for wire targets under ground from experimental results. . . . .	136
Figure 114	Time-domain pulses and the corresponding Instantaneous Phase of a $0^\circ$ wire target. . . . .	138
Figure 115	Orientation angle estimates (in degrees) with the Instantaneous Phase Method for wire targets from numerical results. . . . .	139
Figure 116	Orientation angle Instantaneous Phase Method estimates (in degrees) for wire targets in air from experimental results. . . . .	141
Figure 117	Orientation angle Instantaneous Phase Method estimates (in degrees) for wire targets under ground from experimental results. . . . .	142
Figure 118	Scattering Diagram. . . . .	145
Figure 119	Resistively-Loaded Modulated Scatterer (RLMS) designs. . . . .	147
Figure 120	Time-domain scattered fields for a) unloaded modulated scatterer, b) $R_1 = R_2 = 10 \Omega$ , c) $R_1 = R_2 = 20 \Omega$ , and d) $R_1 = R_2 = 60 \Omega$ . . . . .	149
Figure 121	Reflected time-domain signals for the candidate resistor values. $R_1 = 40 \Omega$ and $R_2 = 100 \Omega$ (solid line) are chosen as the optimum parameter pair. . . . .	149
Figure 122	Contour plot of $PP/C^{2.2}$ . The circle markers indicate the parameters for the resistive profiles selected in Figure 121. . . . .	150
Figure 123	A diagram of the SN74LS193N binary counter and 2N 3904 transistor used to control the terminal voltage on the RLMS. . . . .	151
Figure 124	A photograph of the SN74LS193N binary counter and 2N 3904 transistor used to control the terminal voltage on the RLMS. . . . .	152
Figure 125	Measurement Timing Diagram. . . . .	154
Figure 126	$S_{21}$ magnitude measured at 2.5 GHz, RLMS 0.1016 m from antennas with the RLMS modulating. . . . .	154
Figure 127	A diagram for an experiment with an RLMS positioned 0.254 m from the RVDs. . . . .	155

Figure 128	A Time-domain reflected signal from an RLMS positioned 0.254 m from the antennas. . . . .	155
Figure 129	Time-domain reflected signals for the 10.5 Volt RLMS (solid blue line) and the 30 Volt RLMS (dashed red line) obtained from the NEC model. .	156
Figure 130	Time-domain reflected signals for the 10.5 Volt RLMS (solid blue line) and the 30 Volt RLMS (dashed red line) obtained experimentally. . . . .	157
Figure 131	Photograph of the thin substrate Resistively-Loaded Modulated Scatterer	158
Figure 132	Time-domain reflected signals for the thin RLMS from an experiment (dashed red line) and a NEC model (solid blue line). . . . .	158
Figure 133	Time-domain reflected signals for the thick RLMS from an experiment (dashed red line) and a NEC model (solid blue line). . . . .	159
Figure 134	Experimental setup used for RVD radiation pattern measurements. . . . .	160
Figure 135	Experimental time-domain responses (blue) and simulation time-domain responses (red) for RVD radiation pattern measurements. . . . .	161
Figure 136	Experimental setup used for miniature hydrology experiment. . . . .	163
Figure 137	Experimental results from miniature hydrology experiment. The color scale goes from -130 dB to -90 dB. . . . .	164
Figure 138	A timing diagram of the CP RLMS measurement. . . . .	167
Figure 139	Four S-parameter time-domain responses of the RLMS. . . . .	168
Figure 140	Co-polarization (blue) and cross-polarization (green) time-domain responses of the RLMS. . . . .	168
Figure 141	Co-polarization and cross-polarization responses versus time and position for the RLMS. . . . .	169
Figure 142	Four S-parameter time-domain responses of the buried RLMS. . . . .	170
Figure 143	Co-polarization (blue) and cross-polarization (green) time-domain responses of the buried RLMS. . . . .	170
Figure 144	Co-polarization and cross-polarization responses versus time and position for the buried RLMS. . . . .	171

## SUMMARY

This thesis presents a new dual circularly polarized antenna for ground penetrating radar applications. The new antenna design uses four crossed Resistive-Vee Dipoles (RVD) operating in bistatic mode to measure multiple polarizations. The antenna system is able to distinguish radially symmetric and linear targets with its ability to transmit right-hand circularly polarized (RHCP) fields and receive both left-hand circularly polarized (LHCP) and RHCP scattered fields. The type of target can be identified by comparing the relative amplitudes of the received LHCP fields and RHCP fields. For example, linear targets such as wires may be identified by equal amounts of scattered LHCP and RHCP fields.

Numerical modeling was used to optimize the arrangement of the four RVDs in the RVD-based CP antenna to have low coupling and good circular polarization at close range. The resulting antenna design is shown to be very effective at finding buried wire targets without being costly. Additional modeling was performed to improve the circular polarization by changing the arm shape and resistive profile of the RVDs.

Three methods are developed for estimating the spatial orientation angle of a detected wire target. The first method involves synthesizing transmission and reception of linear polarization at many angles to find the angle that matches the angle of the wire target. The second and third methods involve directly computing the angle of the wire target from the phase difference in the co-polarization and cross-polarization responses. All three methods provide accurate estimates.

The RVD-based CP antenna enables strong detection of subsurface targets along with geometry-based classification of targets. The RVD-based CP antenna is well suited for finding buried wires and rejecting miscellaneous clutter that may be present in the ground.

# CHAPTER 1

## INTRODUCTION

This dissertation presents an antenna for finding buried linear targets with geometry-based target classification. Many buried targets of interest are linear, such as wires and pipes. There are many applications for the ability to tell the difference between a buried linear target and targets with other symmetries, such as rocks, soil inhomogeneities, trash, and other buried clutter. One of these application is utility detection, where the antenna could be used for finding buried communications wires and buried pipes. Utility companies could benefit from being able to easily find their buried utility wires and pipes. Construction and road workers could also benefit from knowing where the buried wires and pipes are to avoid digging into them. One military application is the detection of buried wires used to trigger the detonation of an explosive device. Finding these buried wires could indicate that a buried explosive device is nearby and may prevent injuries and deaths.

Ground Penetrating Radar (GPR) is often used for finding buried objects. Seismic sensing can also be used for finding buried objects, but seismic sensors must be in contact with the ground in order to be effective. One particularly important reason that GPR is useful to find the wires leading to buried explosive devices is that GPR allows the detection of buried objects without disturbing the surface of the ground. GPR radar is also useful because it allows large areas to be scanned for targets relatively rapidly [1].

Circular polarization (CP) has several properties that make it useful in GPR. First, a circularly polarized antenna receives no power from waves polarized with the opposite handedness of circular polarization. Second, a circularly polarized antenna can be rotated arbitrarily around its bore-sight axis without affecting its reception of scattered waves. Third, a circularly polarized wave reverses its handedness as it scatters off of a smooth surface, making it invisible to the circularly polarized antenna that transmitted the wave. Finally, thin wires scatter linearly polarized waves when excited by circular polarization [2]. The

last two properties make circular polarization an attractive option for finding buried wires when other types of targets may also be present.

This research uses circular polarization to recover information about the geometry of a buried target. The main contribution of this research is the development of a new dual circular polarization antenna. The antenna is capable of transmitting and receiving both senses of circular polarization. The antenna is well suited for geometry-based classification of buried targets.

The antenna is composed of four orthogonal and linearly polarized elements, so the antenna may synthesize the transmission and reception of circular polarization. A resistive-vee dipole (RVD) was chosen for each of the linearly polarized elements for the antenna. The RVD has low self clutter, a low radar cross-section, and wide-band performance. For the antenna, four RVDs are arranged in a close configuration that has low coupling between the RVDs. The RVDs are used bistatically to avoid the large reflections from monostatic measurements. The antenna supports dual circular polarization while retaining the advantages of the RVD.

By receiving both RHCP and LHCP, the antenna is able to detect a target and determine the type of geometry of the target. Information gathered by the antenna is used to distinguish between linear targets, including wires and pipes, and radially symmetric targets, including flat surfaces, discs, and rings.

## **1.1 Synthesis of Circular Polarization**

In this research circular polarization is synthesized from orthogonal linearly polarized antennas that are in phase quadrature. This method allows the handedness of circular polarization on the antenna to be switched both quickly and easily. This method can be used in GPR to distinguish between linear targets like wires and pipes, and radially symmetric targets like rocks [3].

An alternative option for measuring circular polarization with linearly polarized antennas is mechanical rotation [1]. In this method a measurement from a linearly polarized antenna is made, and then the antenna is rotated  $90^\circ$  so that a second measurement can be made with the antenna in the orthogonal position. The main disadvantage of this approach is that it takes a long time to complete the measurements as a result of the need for slow and precise rotations between measurements.

A diagram of orthogonal linearly polarized antennas is shown in Figure 1 to illustrate circular polarization synthesis. In Figure 1 antenna A is responsible for transmitting the X-component electric fields, and antenna B is responsible for transmitting the Y-component electric fields. By applying equal amplitude voltages with a positive  $90^\circ$  phase difference between antennas B and A, the antennas transmit left-hand circular polarization in the positive Z-direction. Applying equal amplitude voltages with a negative  $90^\circ$  phase difference between antennas B and A causes the antennas to transmit right-hand circular polarization.

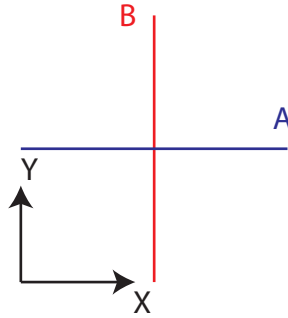


Figure 1: A diagram of orthogonal linearly polarized antennas for producing circular polarization.

## 1.2 Existing Circular Polarization GPR Technologies

### 1.2.1 Crossed-Dipole Antennas

A crossed-dipole antenna is made from two orthogonal dipole antennas. The dipole antennas are oriented orthogonally to each other, and they are typically given a  $90^\circ$  phase difference by using a  $90^\circ$  hybrid. Since the crossed-dipole antenna is made from dipole

antennas, it inherits many performance characteristics of the dipole antennas. A dipole antenna consists of two arms, which are typically pointed in opposite directions. The dipole antenna operates primarily in a narrow band that depends on the total length of the dipole antenna. A diagram for a crossed-dipole antenna is shown in Figure 2.

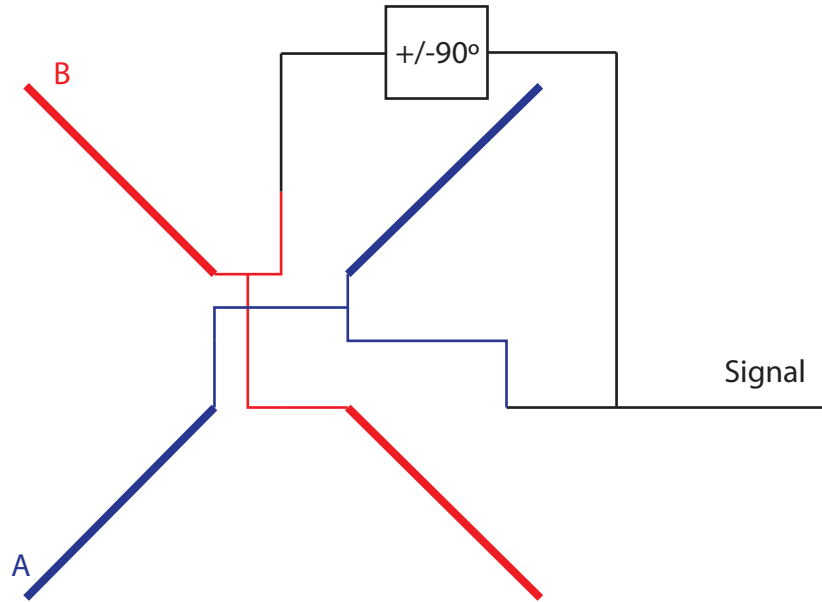


Figure 2: A diagram of a crossed-dipole antenna.

Crossed-dipole antennas have been analyzed and developed for many applications [1,4–13]. Sometimes arrays of crossed-dipole antennas are used to provide uniform illumination of circular polarization over a larger area [5, 8, 12].

The main disadvantage of the crossed-dipole antenna is its narrow bandwidth. Wide bandwidth measurements collect much more information on the target responses and allow target responses to be viewed in the time-domain. Time-domain responses can reveal information on the distance of a target and possibly the material of a target. With a crossed-dipole antenna, it is only possible to measure both senses of circular polarization at or very near to a single frequency. Yoon et al. developed a crossed-dipole antenna with an impedance bandwidth of 1.95-2.75 GHz and circular polarization bandwidth of 2.05-2.27 GHz [10]. Baik et al. developed a broadband crossed-dipole antenna, but its frequency

range is limited between 2.1 GHz and 2.8 GHz [6].

Another issue, which is not specific to crossed-dipole antennas, is the narrow bandwidth of  $90^\circ$  hybrids. It is difficult to get a  $90^\circ$  hybrid that works well over a large frequency range [1]. This could result in poor synthesis of circular polarization.

### 1.2.2 Dual CP Bow-tie Antennas

Bow-tie antennas have also been used to synthesize circular polarization [14–18]. A bow-tie antenna consists of two triangular patches connected to the antenna feed. Bow-tie antennas are linearly polarized and have a large bandwidth. The large bandwidth of the bow-tie antenna is achieved with the scaling and truncation principles [19]. A bow-tie antenna with infinitely long triangular patches would have a geometry that is completely determined by angles. In this case the behavior of the antenna is wavelength invariant. For finite sized bow-tie antennas, the low frequency limit is determined by the lengths of the triangular patches, and the high frequency limit is determined by the size of the feed. A diagram of a bow-tie antenna is shown in Figure 3.

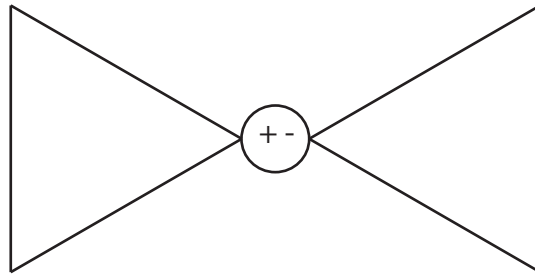


Figure 3: A diagram of a bow-tie antenna.

Circular polarization may be synthesized with bow-tie antennas by applying a  $90^\circ$  phase difference between orthogonal bow-tie antennas.

One problem with bow-tie antennas is the ringing that occurs at the ends of the bow tie, which makes it difficult for the bow-tie antenna to transmit a narrow time-domain pulse [1]. Resistive loading has been used to help this problem [20,21]. The antenna in this work also uses resistive loading but maintains a larger bandwidth than the resistively loaded bow-tie



antennas.

### 1.2.3 Dual CP Vivaldi Antennas

Vivaldi antennas can be used for circular polarization synthesis. A Vivaldi antenna is broadband and linearly polarized. Vivaldi antennas are made from a planar surface conductor. The antenna has a tapered slot cut out of it. The feed voltage is applied across both sides of the slot. It is possible to use orthogonal Vivaldi antennas together with a  $90^\circ$  phase difference to synthesize circular polarization. A diagram of a Vivaldi antenna is shown in Figure 4.

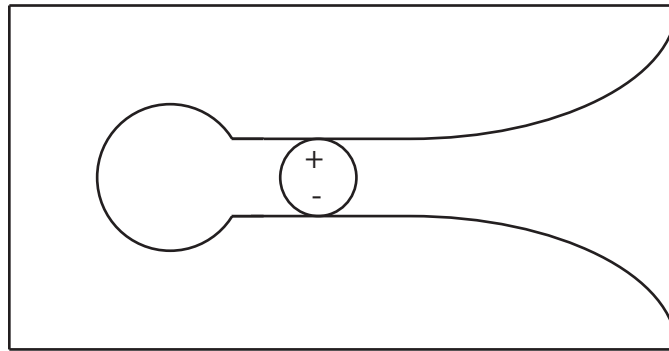


Figure 4: A diagram of a Vivaldi antenna.

In some instances orthogonal Vivaldi antennas have been used to transmit and receive orthogonal directions of linear polarization [22, 23]. Vivaldi antennas have been used to produce circular polarization with some success [24, 25].

### 1.2.4 Sinuous Antennas

The sinuous antenna is a broadband antenna that has multiple long sinuous arms. The sinuous antenna achieves its large bandwidth by taking advantage of the scaling and truncation principles [19]. The frequency limits of the sinuous antenna are determined by the lengths of the sinuous arms and the size of the feed. Each arm of a sinuous antenna produces linear polarization. With four arms  $90^\circ$  apart, the antenna is capable of synthesizing dual circular polarization. The arms of a sinuous antenna are like those of an equiangular

spiral antenna, except that the arms on the sinuous antenna change direction periodically. Although the sinuous antenna is typically a planar antenna, it is sometimes shaped around the surface of a cone.

The patent for the sinuous antenna was introduced by DuHamel [26]. Sinuous antennas are often used for producing circular polarization [27, 28].

The sinuous antenna is an antenna that has issues with high radar cross-section. It is also very dispersive because the high frequencies radiate from near the center of the antenna, and the low frequencies radiate from the outer parts of the antenna. The sinuous antenna also has a polarization tilt that varies with frequency [29]. Polarization tilt refers to the angle between the semi-major axis of the polarization ellipse and a reference line. This results in a frequency dependent phase error.

### **1.2.5 Spiral Antennas**

Another option for circular polarization is a spiral antenna. Spiral antennas are already circularly polarized, so it is not necessary to perform any circular polarization synthesis, and the feeding network is much simpler. Spiral antennas have been shown to be useful as circularly polarized GPR antennas [30–34].

In 1959 Dyson introduced the equiangular spiral antenna [35]. It is a frequency independent circularly polarized antenna. Dyson's antenna was based on the theory by Rumsey that an antenna would be frequency independent if its geometry were completely determined by angles and not lengths [19]. Such an antenna would necessarily have to be infinitely large, but Dyson discovered that a finite size equiangular spiral antenna could have frequency independent performance over a wide range of frequencies. Dyson found that frequency independence could be achieved if the arm lengths on equiangular spiral antenna were only one wavelength long at the lowest frequency. The antenna has an upper limit on its frequency range from the termination of the spiral in the center at the feed. Dyson later developed a unidirectional equiangular spiral by shaping the equiangular spiral antenna around a cone [36]. The unidirectional equiangular antenna showed the same level

of frequency independent performance as the planar equiangular spiral antenna.

Many others have used spiral antennas for GPR [30–34]. Usually these spiral antenna systems use transmit and receive antennas with opposite senses of CP. However, it is possible to use the two spirals to perform measurements for both co-polarization and cross-polarization. The spiral antennas would be used to simultaneously perform monostatic and bistatic measurements. By following this method, one handedness of circular polarization can be received with the monostatic measurement, and the other handedness can be received by the bistatic measurement. Buried targets that reject one handedness of circular polarization can still be detected. The main issue with spiral antennas is that they are not capable of co-located dual circular polarization. The first antenna transmits and receives RHCP while the second antenna receives LHCP. The geometry of this measurement makes it difficult to make accurate comparisons between the polarizations and would result in poor target classification. The separation between the antennas causes the scattering angles, path lengths, and amplitude responses to be different for the two receive antennas. A diagram of the monostatic and bistatic path lengths is shown in Figure 5.

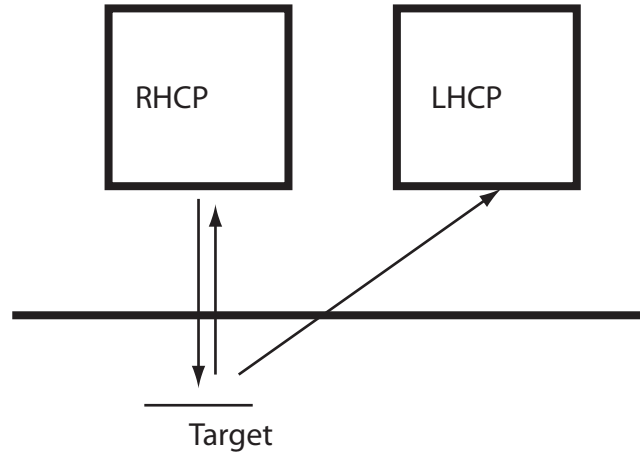


Figure 5: A diagram of a bistatic dual CP target detection.

Another issue with spiral antennas is dispersion [1]. Since higher frequencies are transmitted from near the center of the spiral and lower frequencies are transmitted near the outer

limit of the spiral, the higher frequencies are transmitted earlier than the lower frequencies.

### **1.3 Proposed Circular Polarization GPR System**

The linearly polarized elements used in the antenna for this research were chosen to be Resistive-Vee Dipole (RVD) antennas. The RVD is characterized by its ‘V’ shaped dipole arms and resistive profiles along the dipole arms. Each RVD follows the design from Kim [37]. This RVD design has curved arms and a modified Wu-King resistive profile [38]. The RVD was chosen because it has low self clutter, a low radar cross-section (RCS), and wide-band performance [37]. The RVD can transmit short pulses in the time-domain. The RVD has already been shown to be effective in GPR applications [39].

The RVD can operate between 2 GHz and 8 GHz. The resistive profile dampens reflections off of the ends of the RVD arms to reduce the self clutter.

The RVD has the disadvantage of a low radiation efficiency. The low radiation efficiency would cause problems for detecting distant targets; however in this research the targets are typically less than 1 meter from the RVDs, so the radiation efficiency does not present any difficulties.

A photograph of the RVD is shown in Figure 6. The double-Y balun designed by Venkatesan is on an FR4 substrate [40]. The RVD antenna is on a thin Kapton substrate that is adhered to the FR4. The resistive profile is approximated with 14 surface-mount resistors.

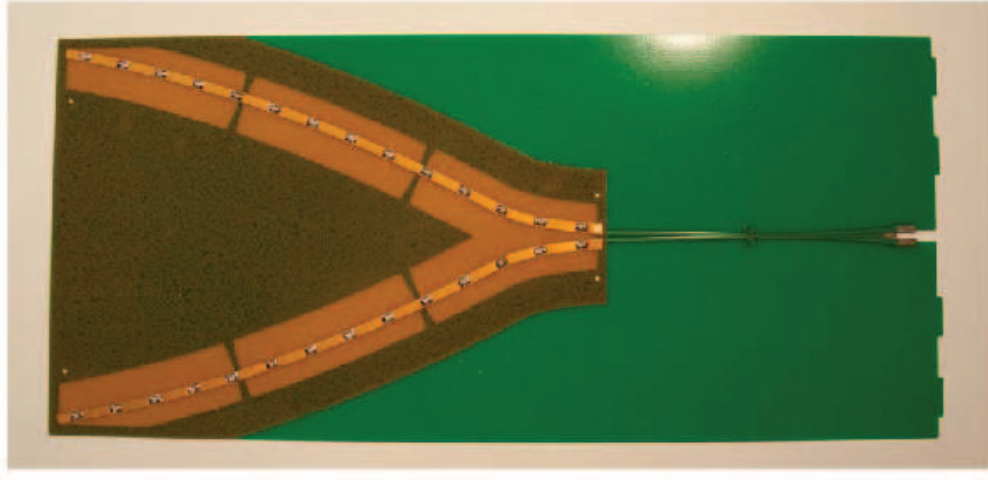


Figure 6: A photograph of the Resistive-Vee Dipole (RVD) antenna.

To begin to synthesize the transmission and reception of circularly polarized radiation with linearly polarized RVD antennas, the RVDs are arranged according to Figure 7.

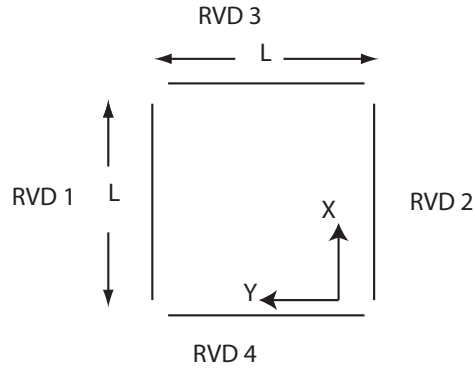


Figure 7: Diagram of the four resistive-vee dipole antenna setup for transmitting and receiving circularly polarized radiation.

RVDs 1 and 3 are the transmitting antennas and RVDs 2 and 4 are the receiving antennas. RVDs 1 and 2 transmit E fields polarized in the  $\hat{x}$  direction on the z-axis, and RVDs 3 and 4 transmit E fields polarized in the  $\hat{y}$  direction on the z-axis. The transmitted E fields

from RVDs 1 and 3 at the position of a scatterer on the z-axis are defined respectively as

$$E_1 = \begin{bmatrix} E_{X1} \\ E_{Y1} \end{bmatrix} = \begin{bmatrix} \alpha_1 \\ 0 \end{bmatrix} \frac{V_1}{L} \quad (1)$$

$$E_3 = \begin{bmatrix} E_{X3} \\ E_{Y3} \end{bmatrix} = \begin{bmatrix} 0 \\ \alpha_3 \end{bmatrix} \frac{V_3}{L}, \quad (2)$$

Where  $\alpha_1$  and  $\alpha_3$  describe the radiation from the RVDs to the scatterer. For identical RVDs,  $\alpha_1 = \alpha_3$ . With  $V_1$  and  $V_3$  as the feed voltages,  $E_1$  and  $E_3$  describe radiated fields that are proportional to  $V_1$  or  $V_3$  and linearly polarized orthogonal directions. Although RVDs 2 and 4 are receiving antennas, their E fields as transmitting antennas can still be used for the reciprocity relation. The transmitted E fields of RVDs 2 and 4,  $E_2$  and  $E_4$ , are given by

$$E_2 = \begin{bmatrix} E_{X2} \\ E_{Y2} \end{bmatrix} = \begin{bmatrix} \alpha_2 \\ 0 \end{bmatrix} \frac{V_2}{L} \quad (3)$$

$$E_4 = \begin{bmatrix} E_{X4} \\ E_{Y4} \end{bmatrix} = \begin{bmatrix} 0 \\ \alpha_4 \end{bmatrix} \frac{V_4}{L}. \quad (4)$$

If the scatterer is assumed to be small, then the scatterer has an electric dipole moment that is related linearly to the transmitted field. From reciprocity, it is possible to compute the received voltage on antenna  $m$  when transmitting with antenna  $k$  with

$$V_{Rmk} = -\frac{j\omega Z_c (\epsilon E_m^T P_e E_k)}{2V_m}, \quad k = 1 \text{ or } 3, m = 2 \text{ or } 4, \quad (5)$$

where  $Z_c$  is the impedance of the feeding line, and  $P_e$  is the polarizability matrix for the scatterer [34]. Here, the magnetic polarizability is assumed to be negligibly small. For this development the tensor product is treated as a matrix product. A generic polarizability matrix,  $P_e$ , for a scatterer in the X-Y plane can be written as

$$P_e = \begin{bmatrix} p_{xx} & p_{xy} \\ p_{yx} & p_{yy} \end{bmatrix}. \quad (6)$$

If the set of antennas are treated as a 4-port network, then the scattering parameters of the signal received on antenna  $m$  from the signal transmitted from antenna  $k$  may be represented as

$$S_{mk} = \frac{V_{Rmk}}{V_k} = -\frac{j\omega Z\epsilon(E_m^T P_e E_k)}{2V_m V_k}, \quad m = 2 \text{ or } 4, k = 1 \text{ or } 3. \quad (7)$$

If all four antennas are made to be identical, then  $\alpha_1 = \alpha_2 = \alpha_3 = \alpha_4 = \alpha$ . There are 2 transmitting antennas and 2 receiving antennas, so the four relevant S-parameters are

$$S_{21} = b \begin{bmatrix} \alpha_2 & 0 \end{bmatrix} \begin{bmatrix} p_{xx} & p_{xy} \\ p_{yx} & p_{yy} \end{bmatrix} \begin{bmatrix} \alpha_1 \\ 0 \end{bmatrix} = b\alpha_1\alpha_2 p_{xx} = b\alpha^2 p_{xx} \quad (8)$$

$$S_{23} = b \begin{bmatrix} \alpha_2 & 0 \end{bmatrix} \begin{bmatrix} p_{xx} & p_{xy} \\ p_{yx} & p_{yy} \end{bmatrix} \begin{bmatrix} 0 \\ \alpha_3 \end{bmatrix} = b\alpha_3\alpha_2 p_{xy} = b\alpha^2 p_{xy} \quad (9)$$

$$S_{41} = b \begin{bmatrix} 0 & \alpha_4 \end{bmatrix} \begin{bmatrix} p_{xx} & p_{xy} \\ p_{yx} & p_{yy} \end{bmatrix} \begin{bmatrix} \alpha_1 \\ 0 \end{bmatrix} = b\alpha_1\alpha_4 p_{yx} = b\alpha^2 p_{yx} \quad (10)$$

$$S_{43} = b \begin{bmatrix} 0 & \alpha_4 \end{bmatrix} \begin{bmatrix} p_{xx} & p_{xy} \\ p_{yx} & p_{yy} \end{bmatrix} \begin{bmatrix} 0 \\ \alpha_3 \end{bmatrix} = b\alpha_3\alpha_4 p_{yy} = b\alpha^2 p_{yy}, \quad (11)$$

where  $b = \frac{-j\omega Z_c \epsilon}{2L^2}$ . Antennas 1 and 3 are able to synthesize circular polarization if they are driven together with the appropriate input voltages. The transmission of left-hand circularly polarized radiation is done by taking the X-polarized radiation and adding  $j$  times an equal Y-polarized radiation to obtain radiation with a  $90^\circ$  phase difference between the X- and Y-components. In the established notation, the left-hand circular polarization transmitted E field matrix is given by

$$E_{LHCP} = \frac{E_1 + jE_3}{\sqrt{2}} = \begin{bmatrix} \alpha \\ j\alpha \end{bmatrix} \frac{V}{\sqrt{2}L}. \quad (12)$$

Co-polarization refers to the transmission and reception of circular polarizations of the same handedness. Cross-polarization refers to the transmission and reception of circular

polarizations of opposite handednesses. Antennas 2 and 4 can be used together to receive left-hand and right-hand circular polarization. The co-polarization E field matrix is given by

$$E_{copol} = \frac{E_2 + jE_4}{\sqrt{2}} = \begin{bmatrix} \alpha \\ j\alpha \end{bmatrix} \frac{V}{\sqrt{2}L}. \quad (13)$$

Antennas 2 and 4 can switch from LHCP to RHCP simply by introducing a  $-90^\circ$  phase shift in place of the  $90^\circ$  phase shift. The reception of left-hand circularly polarized radiation is done by taking the X-direction E field matrix and subtracting  $j$  times the Y-direction E field matrix. In the established notation, the cross-polarization E field matrix is

$$E_{xpol} = \frac{E_2 - jE_4}{\sqrt{2}} = \begin{bmatrix} \alpha \\ -j\alpha \end{bmatrix} \frac{V}{\sqrt{2}L}. \quad (14)$$

By using the circular polarization E field matrices with Equation 5, the co-polarization S-parameter can be calculated by

$$\begin{aligned} S_{copol} &= \frac{b}{2} \begin{bmatrix} \alpha & j\alpha \end{bmatrix} \begin{bmatrix} p_{xx} & p_{xy} \\ p_{yx} & p_{yy} \end{bmatrix} \begin{bmatrix} \alpha \\ j\alpha \end{bmatrix} \\ &= \frac{b\alpha^2 p_{xx} - b\alpha^2 p_{yy}}{2} + \frac{j(b\alpha^2 p_{xy} + b\alpha^2 p_{xy})}{2} \\ &= \frac{S_{21} - S_{43}}{2} + j \frac{(S_{23} + S_{41})}{2}. \end{aligned} \quad (15)$$

Similarly, the cross-polarization S-parameter can be calculated by

$$\begin{aligned} S_{xpol} &= \frac{b}{2} \begin{bmatrix} \alpha & -j\alpha \end{bmatrix} \begin{bmatrix} p_{xx} & p_{xy} \\ p_{yx} & p_{yy} \end{bmatrix} \begin{bmatrix} \alpha \\ j\alpha \end{bmatrix} \\ &= \frac{b\alpha^2 p_{xx} + b\alpha^2 p_{yy}}{2} + \frac{j(b\alpha^2 p_{xy} - b\alpha^2 p_{xy})}{2} \\ &= \frac{S_{21} + S_{43}}{2} + j \frac{(S_{23} - S_{41})}{2}. \end{aligned} \quad (16)$$

Using Equation 15 and Equation 16, an antenna system that transmits LHCP radiation and receives both RHCP and LHCP radiation can be synthesized using four linearly polarized antennas.



Although Equation 15 and Equation 16 can be used to calculate the transmission and reception of circular polarization, it is possible to use arbitrary polarizations for transmission and reception. A polarization can be defined by the relative amplitudes of the orthogonal field X- and Y-components and the phase difference between the field components. Given a transmitted field with relative component amplitudes  $T_X$  and  $T_Y$  and a phase difference  $\phi_T$ , the arbitrary polarization transmitted E field matrix becomes

$$E_{Tap} = T_X E_1 + T_Y e^{j\phi_T} E_3 = \begin{bmatrix} T_X \alpha \\ T_Y e^{j\phi_T} \alpha \end{bmatrix} \frac{V}{\sqrt{T_X^2 + T_Y^2} L}. \quad (17)$$

For a receiving an arbitrary polarization with relative X- and Y-component amplitudes  $R_X$  and  $R_Y$  and phase difference  $\phi_R$ , the corresponding transmitted E field matrix for the arbitrary polarization receiver becomes

$$E_{Rap} = R_X E_2 + R_Y e^{j\phi_R} E_4 = \begin{bmatrix} R_X \alpha \\ R_Y e^{j\phi_R} \alpha \end{bmatrix} \frac{V}{\sqrt{R_X^2 + R_Y^2} L}. \quad (18)$$

The received signal from transmitting one arbitrary polarization and receiving another can be calculated by

$$\begin{aligned} S_{ap} &= \frac{b}{\sqrt{(T_X^2 + T_Y^2)(R_X^2 + R_Y^2)}} \begin{bmatrix} R_X \alpha & R_Y e^{j\phi_R} \alpha \end{bmatrix} \begin{bmatrix} p_{xx} & p_{xy} \\ p_{yx} & p_{yy} \end{bmatrix} \begin{bmatrix} T_X \alpha \\ T_Y e^{j\phi_T} \alpha \end{bmatrix} \\ &= \frac{T_X R_X b \alpha^2 p_{xx} + T_Y R_Y e^{j(\phi_T + \phi_R)} b \alpha^2 p_{yy}}{\sqrt{(T_X^2 + T_Y^2)(R_X^2 + R_Y^2)}} + \frac{T_Y R_X e^{j\phi_T} b \alpha^2 p_{xy} + T_X R_Y e^{j\phi_R} b \alpha^2 p_{yx}}{\sqrt{(T_X^2 + T_Y^2)(R_X^2 + R_Y^2)}} \\ &= \frac{T_X R_X S_{21} + T_Y R_Y e^{j(\phi_T + \phi_R)} S_{43}}{\sqrt{(T_X^2 + T_Y^2)(R_X^2 + R_Y^2)}} + \frac{T_Y R_X e^{j\phi_T} S_{23} + T_X R_Y e^{j\phi_R} S_{41}}{\sqrt{(T_X^2 + T_Y^2)(R_X^2 + R_Y^2)}}. \end{aligned} \quad (19)$$

## 1.4 Outline

In Chapter 2 numerical results for the RVD-based CP antenna are presented. Numerical results were obtained with NEC2d (Numerical Electromagnetics Code), a method of moments program. First, the configuration of the RVDs was optimized. The goals of the

optimization were low coupling between the RVDs and close RVD spacing to ensure good circular polarization at short range. Next, targets were simulated to test the performance of the optimized RVD-based CP antenna. The targets include wires and circular loops.

In Chapter 3 experimental results for the RVD-based CP antenna are presented. Wire and loop targets were measured in both air and in the ground. Experiments were also performed with clutter objects in the ground.

In Chapter 4 changes to the RVD arm curvature and resistive profile are presented. The RVD was changed to improve the quality of off-boresight circular polarization.

In Chapter 5 three methods for estimating the orientation angle of a wire target are presented. The first method involves rotating linearly polarized waves to find the angle at which the transmitted linearly polarized wave is aligned with the wire target. The second method involves computing the angle of the wire target from the frequency-domain phase difference between the co-polarized and cross-polarized responses. The third method involves computing the time-domain instantaneous phase between the co-polarized and cross-polarized responses.

In Chapter 6 research on the resistively-loaded modulated scatterer (RLMS) is presented. The RLMS is a subsurface probe capable of modulating between two impedance states. The resistive profile of the RLMS was optimized for high strength and low ringing in the reflected signal. The RLMS was used to measure the radiation pattern of the RVD. The RLMS was used in a hydrology experiment to detect ground water.

In Chapter 7 conclusions are presented.

## **CHAPTER 2**

### **NUMERICAL MODELING FOR THE DUAL CP ANTENNA**

The RVD-based circularly polarized (CP) antenna system was modeled in NEC2d to evaluate its performance. NEC2d is a method of moments program for computing currents and fields in the frequency domain. The RVD-based CP antenna was chosen to use four RVDs to avoid the need for any monostatic measurements. The NEC2d models were used to optimize the arrangement of the four RVDs [41].

The goals of the numerical modeling are to find a configuration of RVDs that is suitable for producing dual circular polarization, to evaluate the effectiveness of the dual CP detection, and to predict the performance of the RVD-based CP antenna in experiments. The numerical models are meant to facilitate the development of a successful prototype antenna.

#### **2.1 Optimization of RVD Configuration**

The optimization of the four-RVD configuration considers two features of the antenna system: the physical separation of the RVDs and the coupling between them. The physical separation and coupling are closely related. The goal of the optimization is to find a good balance of low coupling without high separation between the RVDs.

##### **2.1.1 Physical Interference**

First, the minimum distance between the RVDs was calculated for many antenna configurations. To make sure that it is practical to build the RVD configuration, it is important to be aware how close to touching the RVDs are in each configuration. In addition the antenna configurations with greater minimum distance should have less coupling. Each RVD is 17.15 cm long with 11.43 cm of separation between the ends of the arms. Positions 1 and 2 are the X- and Y- coordinates for the feed of first quadrant RVD respectively. The other RVDs were positioned so that the system would be invariant under  $90^\circ$  rotations. Position

1 and Position 2 are represented by  $P_1$  and  $P_2$ .

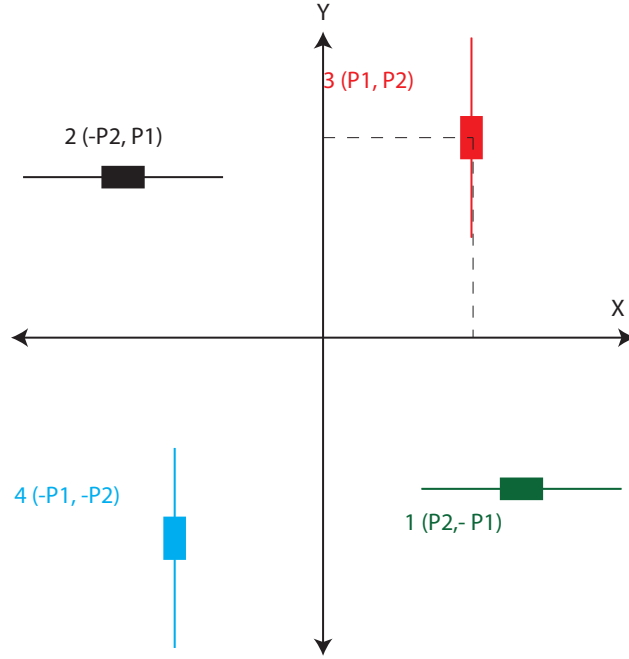


Figure 8: A diagram showing the effects of  $P_1$  and  $P_2$  on the RVD configuration.

Having either  $P_1$  or  $P_2$  equal to 0 results in a configuration with antenna feeds at the edge midpoints of a square. The size of such a square would need to be quite large to get sufficient separation between the antennas. The minimum distance between RVD segments of adjacent RVDs versus  $P_1$  and  $P_2$  is shown in Figure 9. This minimum distance roughly indicates how close adjacent RVDs are from touching. A greater minimum distance means more separation between the RVDs and therefore lower coupling. Keeping  $P_1$  equal to  $P_2$  increases the minimum distance between segments most effectively. This constraint means that the RVD feeds should be placed at the four corners of a square.

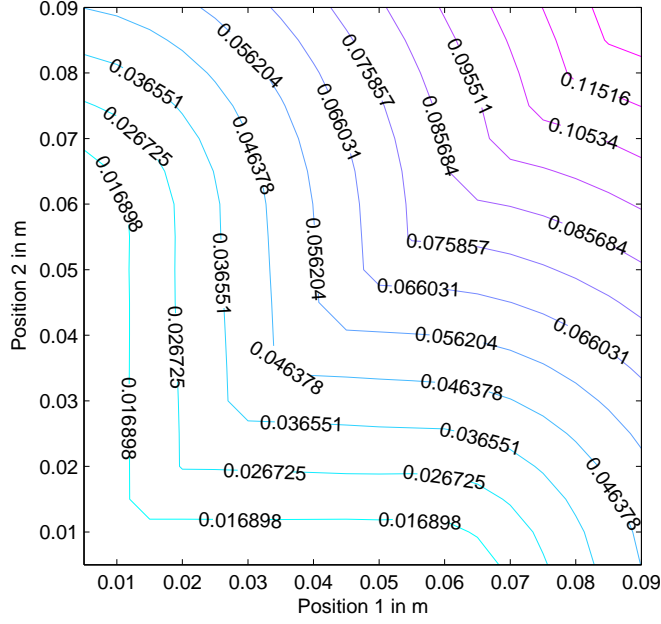


Figure 9: Contour graph of minimum distance (in meters) between points on adjacent RVDs versus  $P_1$  and  $P_2$ .

### 2.1.2 Coupling

NEC2d simulations were performed to quantify the RVD coupling as a function of  $P_1$  and  $P_2$ . The time-domain response is used for this calculation since the results from these antennas are frequently observed in the time-domain.

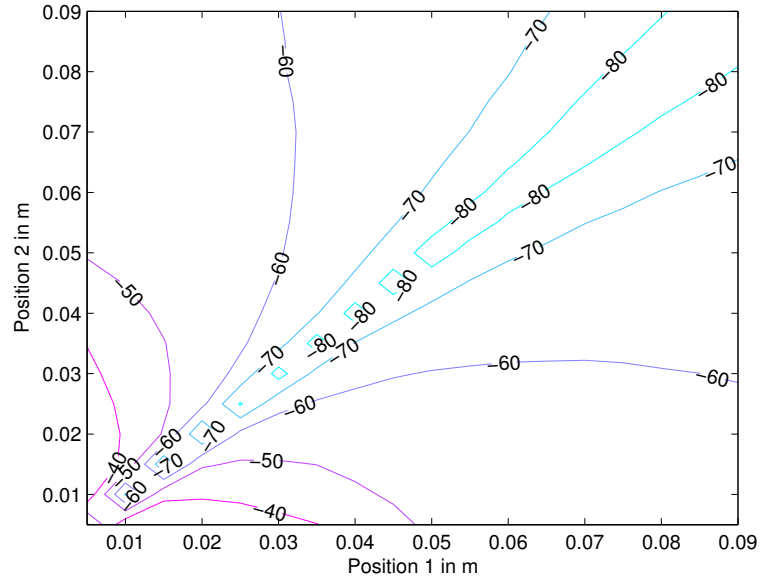
To obtain a time-domain response, S-parameters must first be computed by taking the complex ratio of received voltage to transmitted voltage. When co-polarization or cross-polarization are needed, Equations 15 and 16 are used to compute the co-polarization S-parameter and cross-polarization S-parameter respectively. The transmitted pulse is a differentiated Gaussian pulse with center frequency at 2.5 GHz. The S-parameter is multiplied with the Fast Fourier Transform (FFT) of the differentiated Gaussian pulse. The result is then Inverse Fast Fourier Transformed (IFFT) to obtain the time-domain response.

The strength of the co-polarized signal and the cross-polarized signal can be obtained by subtracting the minimum value from the maximum value (peak-to-peak) in the time-domain. The peak-to-peak values for different antenna positions are shown in Figure 10.

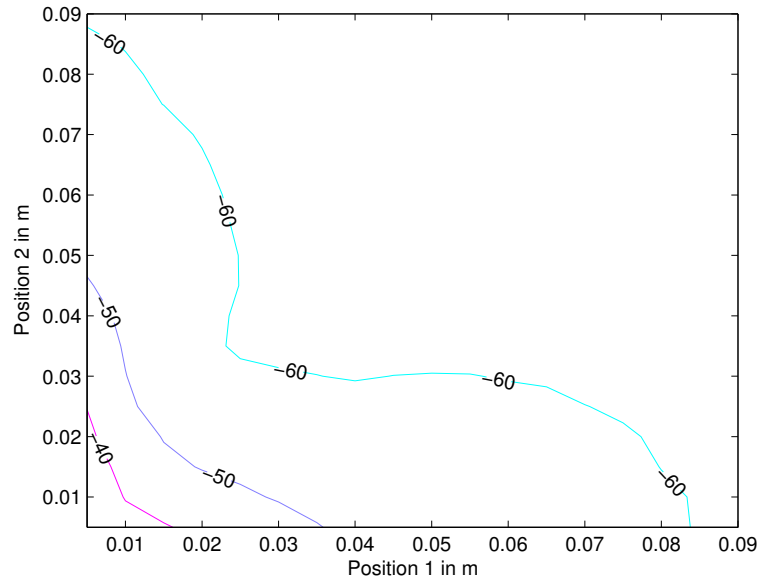
Peak-to-peak co-polarization values for a range of  $P_1$  and  $P_2$  are shown in Figure 10a. Peak-to-peak cross-polarization values are shown in Figure 10b. These figures confirm that making  $P_1 = P_2$  is the most effective way to lower both co-polarized and cross-polarized coupling. It can be observed in Figure 10a and Figure 10b that increasing  $P_1$  and  $P_2$  beyond 3 cm does not significantly reduce coupling.

Coupling strengths between RVDs 2 and 1 and between RVDs 2 and 3 are shown in Figure 11 for  $P_1 = P_2$ . RVDs 2 and 1 are parallel to each other. RVDs 3 and 4 should have similar coupling to RVDs 2 and 1 as a result of the symmetry in the antenna arrangement. RVDs 2 and 3 are orthogonal to each other and should have similar coupling to all other orthogonal pairs in the antenna arrangement. The steepest drop in coupling strength occurs while increasing Positions 1 and 2 to 2.5 cm. After 2.5 cm, additional antenna separation results in only small reductions in coupling strength.

From Figure 9 2.5 cm was selected as an acceptable value for  $P_1$  and  $P_2$ . The resulting antenna arrangement would have the RVD feeds located at the corners of a 5 cm by 5 cm square. A diagram of a top-down view of the antenna configuration is shown in Figure 12.



(a) Co-polarized coupling strength



(b) Cross-polarized coupling strength

Figure 10: Antenna coupling strength in dB versus antenna positions.

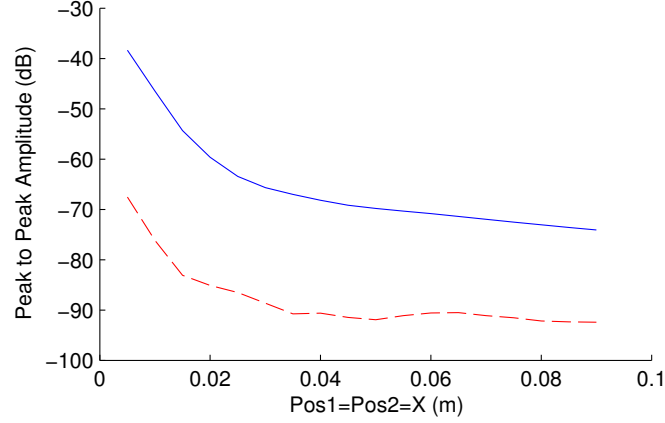


Figure 11: Coupling strength in dB versus antenna separation.  $S_{21}$ , the measurement between a parallel pair of antennas, is shown on the solid line.  $S_{23}$ , the measurement between an orthogonal pair of antennas, is shown on the dashed line.

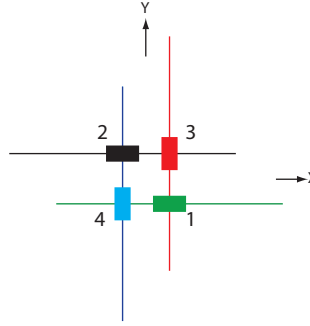


Figure 12: A 2-dimensional top-down view of the antenna geometry.

## 2.2 Modeling of Targets in Free Space

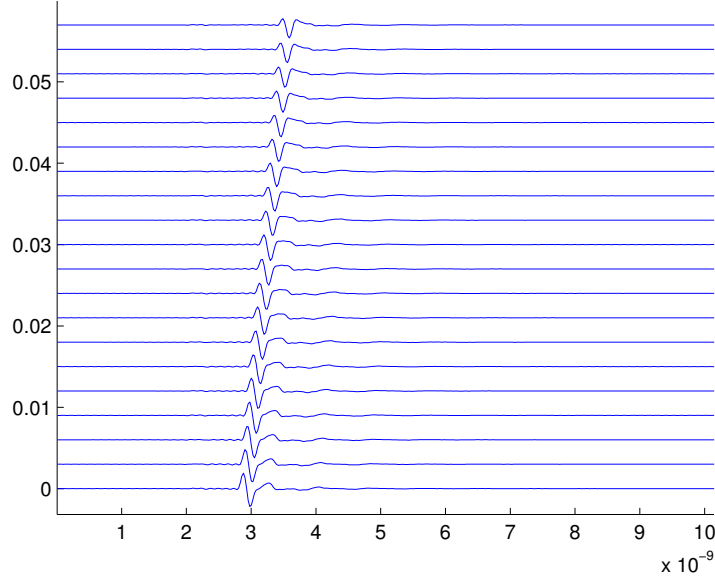
With a finalized antenna system geometry, targets were introduced into the NEC2d simulations to evaluate the performance of the antenna system design. Time-domain responses of a wire target for both co-polarization and cross-polarization are shown in Figure 13. The RVD responses were computed from 10 MHz to 8 GHz in 10 MHz steps. The input pulse in the time-domain was assumed to a differentiated Gaussian pulse with a center frequency of 2.5 GHz. The input pulse and the antenna response are multiplied in the frequency domain and then Inverse Fast Fourier Transformed to get the time-domain response. For each



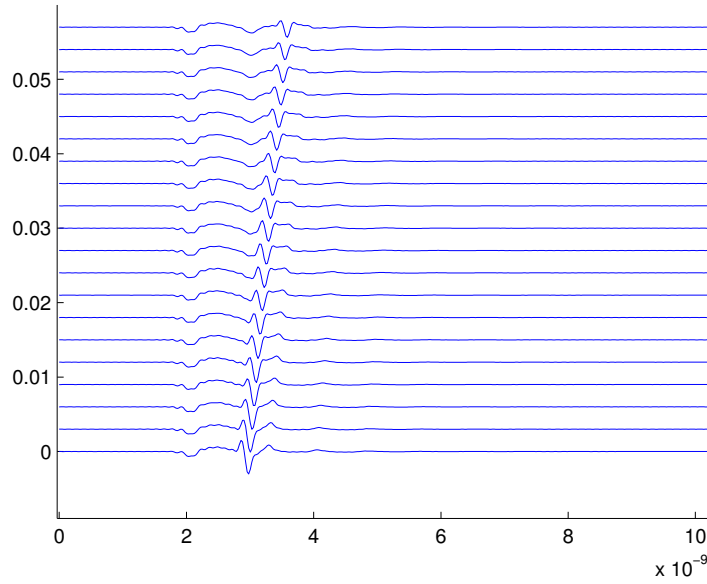
curve, the wire is on the  $z$ -axis and is moved 0.5 cm directly away from the RVD-based CP antenna, starting at  $z = 0.5 \text{ cm}$  and ending at  $z = 10 \text{ cm}$ . The wire target should scatter linearly polarized waves back to the antenna. A linearly polarized wave may be represented as the sum of two circularly polarized waves with equal magnitude and opposite handedness. The RVD-based CP antenna receives co-polarized signal and cross-polarized signal in almost equal amounts, so the RVD-based CP antenna works as expected for the wire target. The scattered response from the wire is delayed by approximately 0.025 ns for each 0.5 cm step away from the antennas. In Figure 13b a signal occurs at 2 ns which is due to the direct coupling between the antennas. This response is much larger for the cross-polarized response as predicated in Figure 10.

Time-domain responses of a circular loop target for both co-polarization and cross-polarization are shown in Figure 14. In Figure 14a the co-polarized signal is always zero because the antennas have zero co-polarized coupling, and the circular loop target scatters only cross-polarization. In Figure 14b the cross-polarized coupling of the antennas once again occurs at 2 ns. There is a cross-polarized pulse. This pulse becomes weaker and further delayed as the target moves farther from the antenna because the waves must travel a greater distance.

It is possible to distinguish the straight wire target from the circular loop target by comparing the relative signal strengths of co-polarized and cross-polarized received signals in Figure 13 and Figure 14. Later in this section, a method is presented for determining the presence of a target and whether the target is a linear type of target or a symmetric type of target.

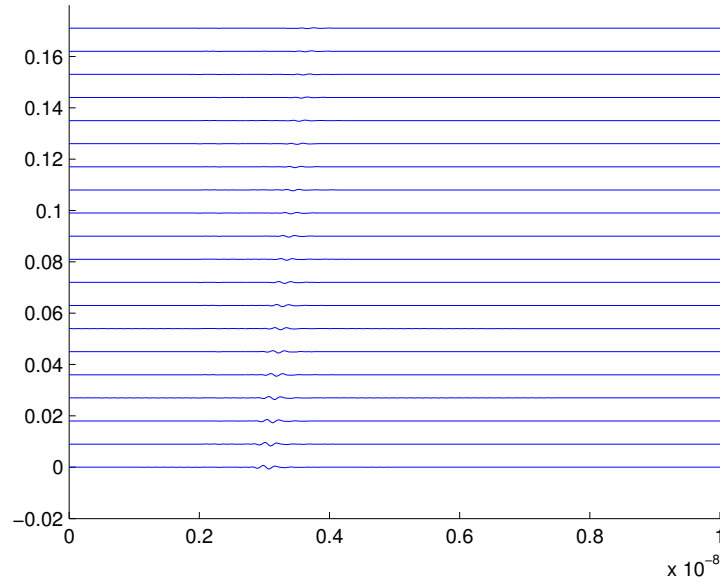


(a) Co-polarized signal

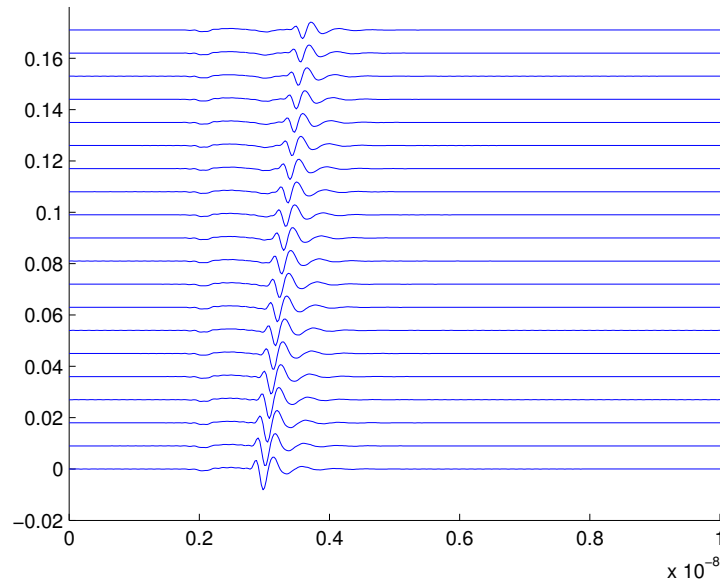


(b) Cross-polarized signal

Figure 13: Antenna time-domain responses from a horizontally oriented 10 cm long straight wire target. The wire was moved from 0.5 cm in front of the RVD-based CP antenna to 10 cm in front of the antenna in 0.5 cm steps. The bottom curve on each figure corresponds to a wire distance of 0.5 cm, and each subsequent curve corresponds to a wire distance 0.5 cm farther than the curve beneath it.



(a) Co-polarized signal

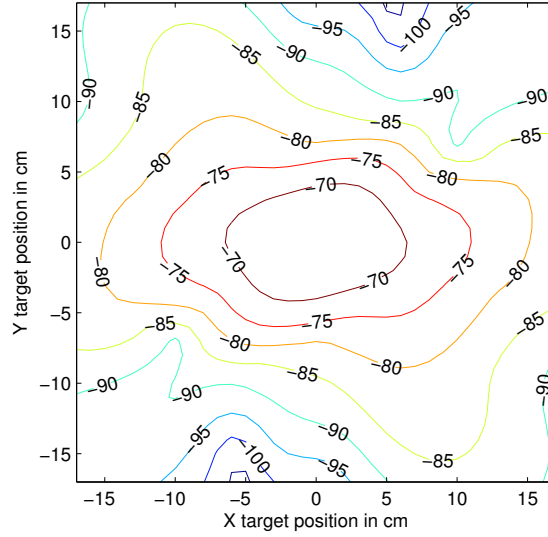


(b) Cross-polarized signal

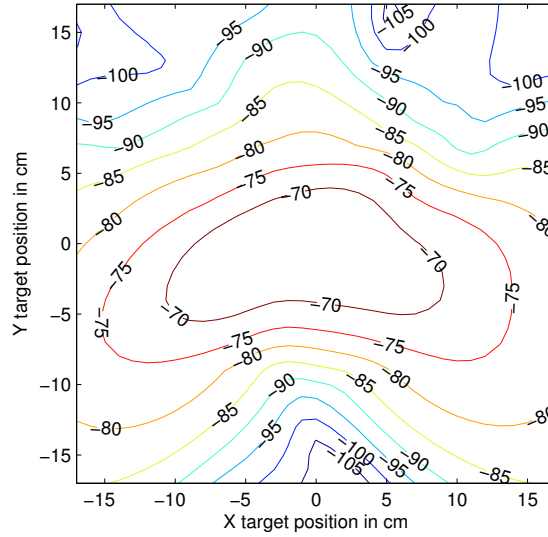
Figure 14: Antenna time-domain responses from a 5 cm diameter circular loop target. The loop was moved from 0.5 cm in front of the antennas to 10 cm in front of the antennas in 0.5 cm steps. The bottom curve on each figure corresponds to a loop distance of 0.5 cm, and each subsequent curve corresponds to a wire distance 0.5 cm farther than the curve beneath it.

Additional NEC2d simulations were performed while moving the targets in a plane perpendicular to the boresight axis. Moving the targets in front of the RVDs yields the same results as scanning the RVD-based CP antenna over the stationary target. The plane of movement for each target was fixed at a distance 10 cm in front of the RVDs. This distance was selected because the RVD-based CP antenna is intended to be used at short range. In a ground penetrating radar application, the RVD-based CP antenna would likely be just above the surface of the ground and the target would be just below the surface of the ground. Once again, the targets selected were a 5 cm diameter wire loop and a 10 cm long straight wire segment. The wire segment was rotated around the boresight axis at angles of  $0^\circ$ ,  $22.5^\circ$  and  $45^\circ$ . It is important to be able to distinguish the straight wire target from the loop target, even when the straight wire target has different spacial orientations. The circular loop target was not rotated because its geometry makes it rotation invariant in this case.

Signal strength versus X- and Y-positions of the  $0^\circ$  wire is shown in Figure 15. The signal strength is found by taking the peak-to-peak value, which is the maximum value of the time-domain signal minus the minimum value of the time-domain signal. This value is then given on a dB scale. The difference between Figure 15a and Figure 15b is shown in Figure 16. Since linear targets should scatter co-polarization and cross-polarization in equal amounts, the area over which the straight wire can be identified as a linear target should be revealed in Figure 16. The  $0^\circ$  wire can be identified as a wire as long as it is within about 5 cm of the point directly in front of the antennas. In this area the difference between the co-polarization peak-to-peak and cross-polarization peak-to-peak values is less than 2 dB.



(a) Co-polarized peak-to-peak



(b) Cross-polarized peak-to-peak

Figure 15: Received signal strength from a  $0^\circ$  wire. Co-polarized signal strength is shown in Figure 15a. Cross-polarized signal strength is shown in Figure 15b. The wire was positioned 10 cm in front of the RVDs in the minus Z-direction. The wire was then moved in the X-Y plane. At each position the received signal strength is given in dB.

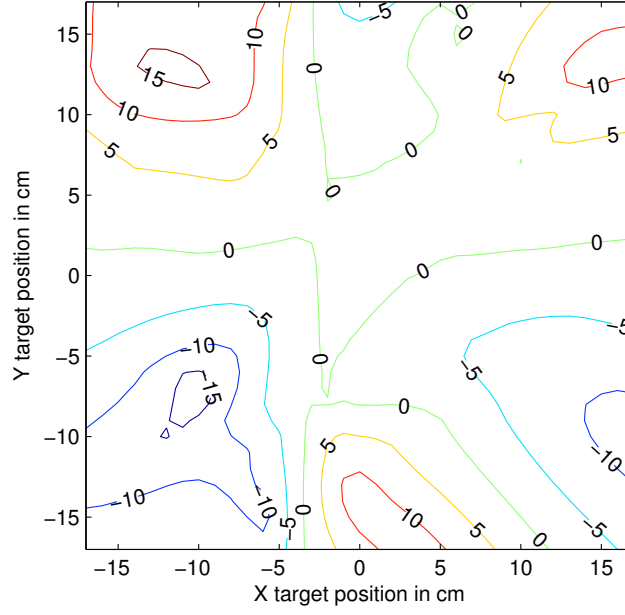
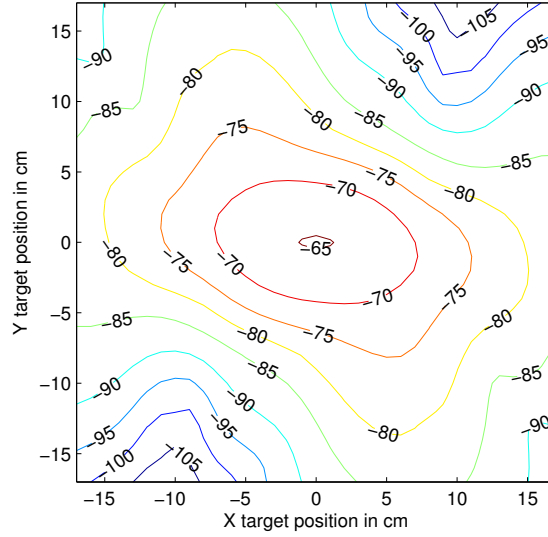
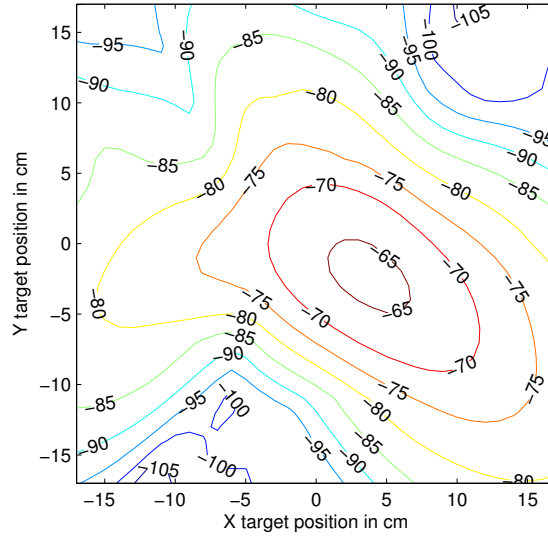


Figure 16: The difference between Figures 15a and 15b.

Signal strength versus X- and Y-position of the  $22.5^\circ$  wire is shown in Figure 17. The co-polarized signal strength is very similar to the cross-polarized signal strength. The difference between Figure 17a and Figure 17b is shown in Figure 18. Over most of the measurement region, the co-polarization and cross-polarization peak-to-peak value difference is less than 2 dB. This similarity between both polarization signal strengths is expected for this wire target.



(a) Co-polarized peak-to-peak



(b) Cross-polarized peak-to-peak

Figure 17: Received signal strength from a  $22.5^\circ$  wire. Co-polarized signal strength is shown in Figure 15a. Cross-polarized signal strength is shown in Figure 15b. The wire was positioned 10 cm in front of the RVDs in the minus Z-direction. The wire was then moved in the X-Y plane. At each position the received signal strength is given in dB.

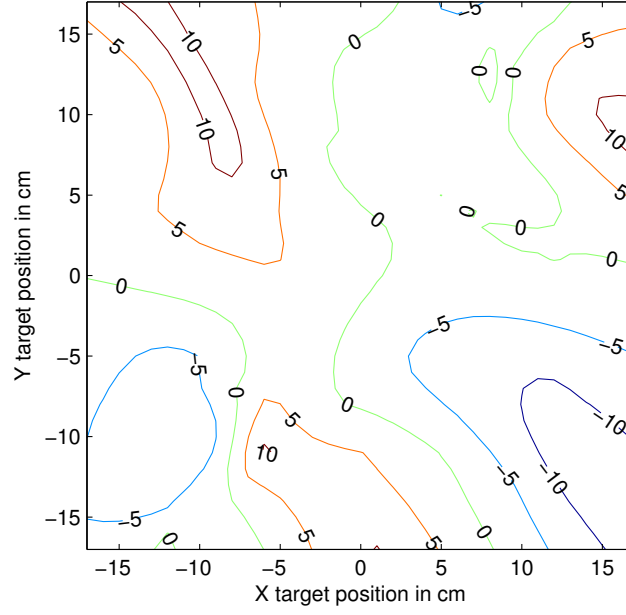
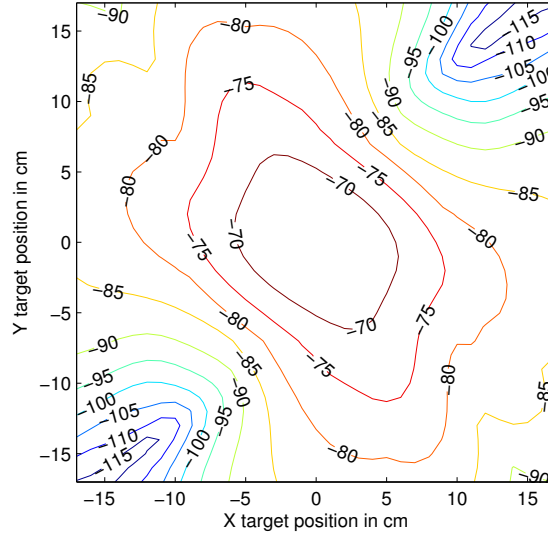


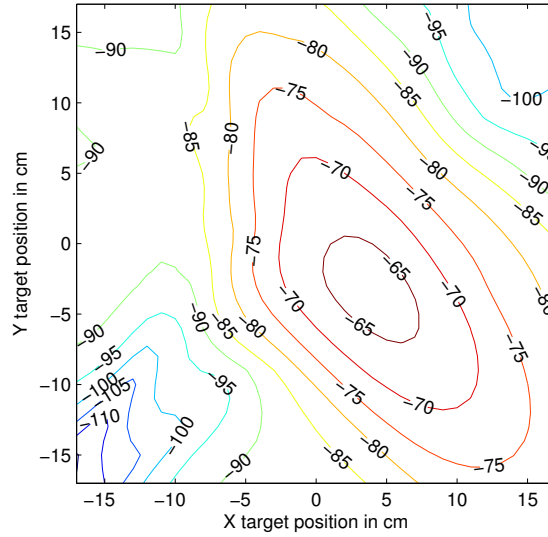
Figure 18: The difference between Figures 17a and 17b.

Signal strength versus X- and Y-position of the  $45^\circ$  wire is shown in Figure 19. The difference between Figure 19a and Figure 19b is shown in Figure 20. The difference between the peak-to-peak values for each polarization is under 5 dB for most of the measurement region. While the  $45^\circ$  wire can still be easily identified as a linear target when it is centered in front of the RVD-based CP antenna, the  $45^\circ$  wire cannot be identified as easily as either the  $0^\circ$  wire or the  $22.5^\circ$  wire when it is moved from the center.





(a) Co-polarized peak-to-peak



(b) Cross-polarized peak-to-peak

Figure 19: Received signal strength from a  $45^\circ$  wire. Co-polarized signal strength is shown in Figure 19a. Cross-polarized signal strength is shown in Figure 19b. The wire was positioned 10 cm in front of the RVDs in the minus Z-direction. The wire was then moved in the X-Y plane. At each position the received signal strength is given in dB.

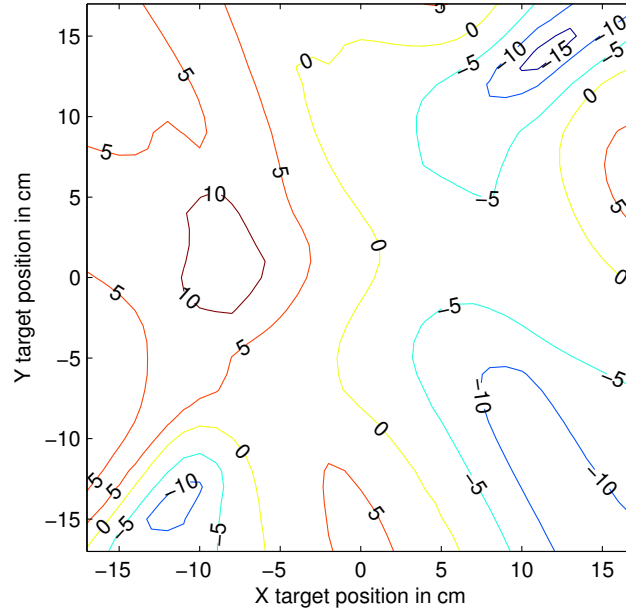
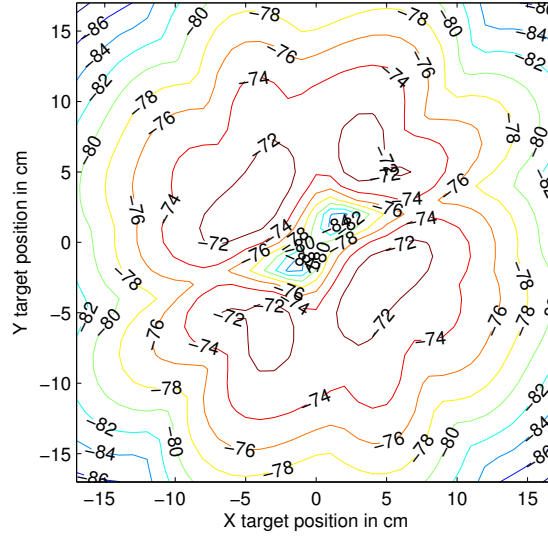
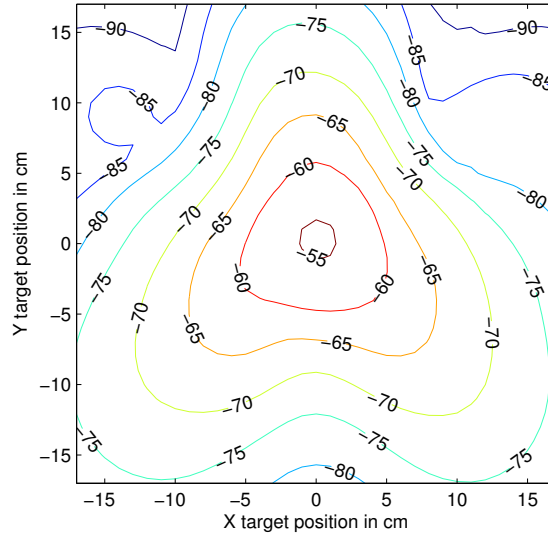


Figure 20: The difference between Figures 19a and 19b.

Signal strength versus X- and Y-position of the circular wire loop is shown in Figure 21. The loop is a symmetric type of target and is expected to have a high cross-polarized response and a low co-polarized response. The cross-polarization peak-to-peak values are high, particularly near the center. The co-polarization peak-to-peak values are very low in the center, then begin to rise and then begin to drop off again. The rise in co-polarization peak-to-peak values is caused by the patterns of the antennas being different in the X- and Y- planes.



(a) Co-polarized peak-to-peak



(b) Cross-polarized peak-to-peak

Figure 21: Received signal strength from a circular wire loop. Co-polarized signal strength is shown in Figure 21a. Cross-polarized signal strength is shown in Figure 21b. The loop was positioned 10 cm in front of the RVDs in the minus Z-direction. The loop was then moved in the X-Y plane. At each position the received signal strength is given in dB.

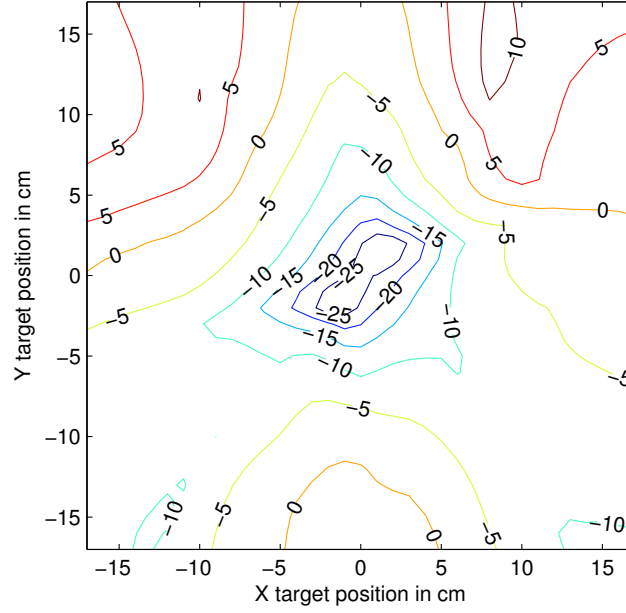


Figure 22: The difference between Figures 21a and 21b.

### 2.2.1 False Color Map Representation

For the next step, a method was developed to combine the co-polarization results and the cross-polarization results in a way that makes it easier to interpret the results. The method involves encoding the co-polarization and cross-polarization peak-to-peak values into the Red, Green and Blue (RGB) values for a color image. This false color map allows a single figure to contain information that used to be contained in two figures.

For the color image, the color of each pixel is defined by an RGB vector with Red, Green and Blue each having a value between 0 and 1. Each pixel corresponds to an X-Y position for co-polarization and cross-polarization measurements. For the false color map, white was selected to indicate measurement positions where no target was detected, red was selected to indicate measurement positions where a symmetric target was detected, and blue was selected to indicate measurement positions where a linear target was detected.

White corresponds to the RGB vector

$$\begin{bmatrix} R_W \\ G_W \\ B_W \end{bmatrix} = \begin{bmatrix} 1 \\ 1 \\ 1 \end{bmatrix}. \quad (20)$$

Red corresponds to the RGB vector

$$\begin{bmatrix} R_R \\ G_R \\ B_R \end{bmatrix} = \begin{bmatrix} 1 \\ 0 \\ 0 \end{bmatrix}. \quad (21)$$

Blue corresponds to the RGB vector

$$\begin{bmatrix} R_B \\ G_B \\ B_B \end{bmatrix} = \begin{bmatrix} 0 \\ 0 \\ 1 \end{bmatrix}. \quad (22)$$

At this point it is necessary to introduce the variables  $X_p$  and  $S$ .  $X_p$  takes values between 0 and 1, with 1 indicating a high likelihood that a target has been detected and 0 indicating that a low likelihood that a target has been detected.  $X_p$  depends on the peak-to-peak value of the cross-polarized signal. Since both linear and symmetric target responses have significant cross-polarized components, cross-polarized peak-to-peak value is good metric for determining the presence or absence of a target.  $S$  takes values between 0 and 1, with 1 indicating that the detected target is from the linear type and 0 indicating that the detected target is from the symmetric type.  $S$  depends on the relative difference between co-polarized and cross-polarized peak-to-peak values.  $X_p$  and  $S$  are given more specific definitions later in this section, but this information should be sufficient for explaining the color mapping method. The formula given by

$$\begin{bmatrix} R \\ G \\ B \end{bmatrix} = \begin{bmatrix} 1 + X_p(S - 1) \\ 1 - X_p \\ 1 - X_p S \end{bmatrix} \quad (23)$$

creates a color mapping that results in white when no target is present, red when a symmetric target is present, and blue when a linear target is present. It should be noted that there may be formulas other than Equation 23 that result in the desired color mapping.  $X_p$  is defined as

$$X_p = \begin{cases} 0 & \text{if } PP_{xpol} < min_{dB}, \\ \frac{PP_{xpol} - min_{dB}}{max_{dB} - min_{dB}} & \text{if } min_{dB} \leq PP_{xpol} \leq max_{dB}, \\ 1 & \text{if } PP_{xpol} > max_{dB}, \end{cases}$$

where  $PP_{xpol}$  is the cross-polarized peak-to-peak value in dB,  $min_{dB}$  is the minimum threshold for target detection,  $max_{dB}$  is the peak-to-peak value that corresponds to detecting a target.  $S$  is defined as

$$S = \begin{cases} 0 & \text{if } |PP_{xpol} - PP_{copol}| > tol_{dB}, \\ \frac{tol_{dB} - |PP_{xpol} - PP_{copol}|}{tol_{dB}} & \text{if } 0 \leq |PP_{xpol} - PP_{copol}| \leq tol_{dB}, \\ 1 & \text{if } |PP_{xpol} - PP_{copol}| = 0, \end{cases}$$

where  $PP_{copol}$  is the co-polarized peak-to-peak value in dB and  $tol_{dB}$  is the the difference in dB between the co-polarized and cross-polarized peak-to-peak values that corresponds to a target being identified as symmetric.  $X_p$  and  $S$  are both bounded between 0 and 1. Values for  $max_{dB}$ ,  $min_{dB}$  and  $tol_{dB}$  have to be selected carefully and may need to be reselected depending on the situation. The false color map assumes that there are no targets with a high co-polarized response and a low cross-polarized response. This is a fair assumption because such a target would be rare if it even existed at all.

A reference for the false color map is shown in Figure 23. The color shifts from blue to red as the ratio of cross-polarization to co-polarization decreases.

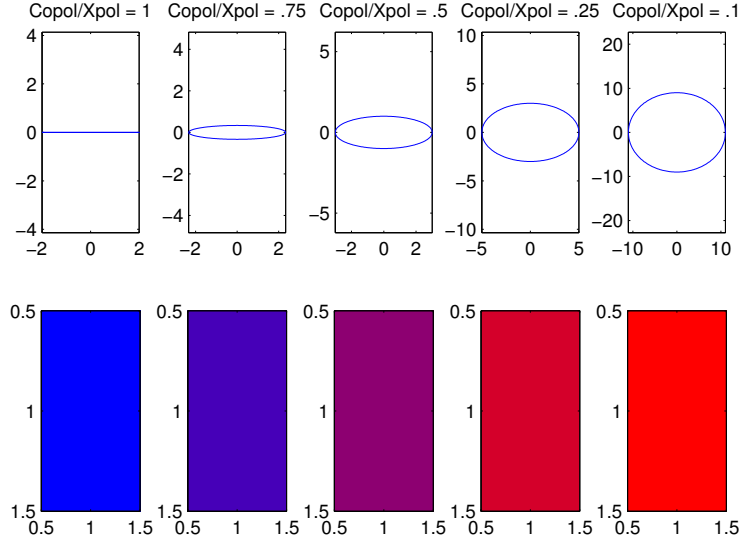


Figure 23: A key for the false color map showing how a ratio of co-polarization to cross-polarization affects the resulting polarization and color.

In Figure 24 two kinds of color map graphs are shown for three rotations of a wire target and a wire loop target. The co-polarized and cross-polarized responses are shown in pseudocolor graphs on a dB scale in the first and second columns of figures. For a pseudocolor graph, the values are plotted relative to a color scale with red indicating the highest values, blue indicating the lowest values, and orange, yellow, and green indicating intermediate values. These are standard MATLAB pseudocolor graphs with field intensities mapped to colors. Scanning position is on the X-axis and time is on the Y-axis. In the third column of figures, the method developed in Section 2.2.1 is used to make false color maps. The false color map is different from the pseudocolor graph because the false color map represents two sets of data, and the pseudocolor graph shows one set of data. For the false color map, the first set of data is represented on the red to blue color scale, and the second set of data is represented on the lightness of the color. The pseudocolor graph only has the color scale, but its color scale uses different colors than that of the false color map. The rotation angle for the three wire targets are  $0^\circ$ ,  $22.5^\circ$ , and  $45^\circ$ . Each of the wire targets has almost equal co-polarized and cross-polarized responses and a visible blue area in the false

color maps. The loop target has a low co-polarized response and a high cross-polarized response, therefore making it appear red in the false color map.

For all of the graphs in Figure 24, the signal envelopes were used. The envelopes are used because they allow more accurate calculations of peak signal strength. In order to compute the signal envelope, first the Hilbert transform of the signal is obtained. The enveloped response appears as a single positive peak, whereas the normal signals appear with multiple positive and negative peaks. The Hilbert transform of the signal is obtained by multiplying the original signal by  $j$  in the frequency-domain before transforming into the time-domain. Then the envelope signal is computed by taking the complex magnitude of the original signal plus  $j$  times the Hilbert transform signal in the time-domain. Examples of normal, Hilbert transform, and enveloped signals are shown in Figure 25. This example is from an experiment measuring the cross-polarized response of a wire target in air. The response from the ground appears beneath the wire.

The results in Figures 15-22 were used with the developed false color map for Figure 26. Here the color map is a function of X and Y, and the depth dependence is removed by choosing the color for the peak target response.  $max_{dB}$  was selected to be -55 dB,  $min_{dB}$  was selected to be -65 dB, and  $tol_{dB}$  was selected to be 20 dB. Figure 26a, Figure 26b and Figure 26c all have a blue area in the center surrounded by white area. The detection of linear targets does not depend on the orientation of the target as demonstrated in these three figures. Figure 26d has a red area surrounded by a blue area that is surrounded by white. The red area indicates that the loop target was correctly identified as radially symmetric. The blue area surrounds the red center because the co-polarization to cross-polarization ratio increases as the loop moves farther from boresight of the antenna. It may be useful that the targets can only be detected and identified within a few centimeters of the center because it allows for nearby targets to be separately detected and identified. As shown in Figure 26, circular polarization measurements from the RVD-based CP antenna enable accurate detection of wire targets. This detection does not depend on the wire target



orientation and is not overly sensitive to the target position.

The target responses have some asymmetry to them. While the geometry of the four-RVD arrangement is symmetric under  $90^\circ$  rotations, the selection of bistatic measurement pairs is not under symmetric  $90^\circ$  rotations. The cross-polarization and co-polarization data calculated from the measurement pairs do not have symmetry across the X- and Y- axes. In fact, it is not possible to reselect the measurement pairs in such a way to eliminate the asymmetry.

The results presented in this chapter demonstrate that the RVD-based CP antenna is capable of identifying the geometry of a target at short range.

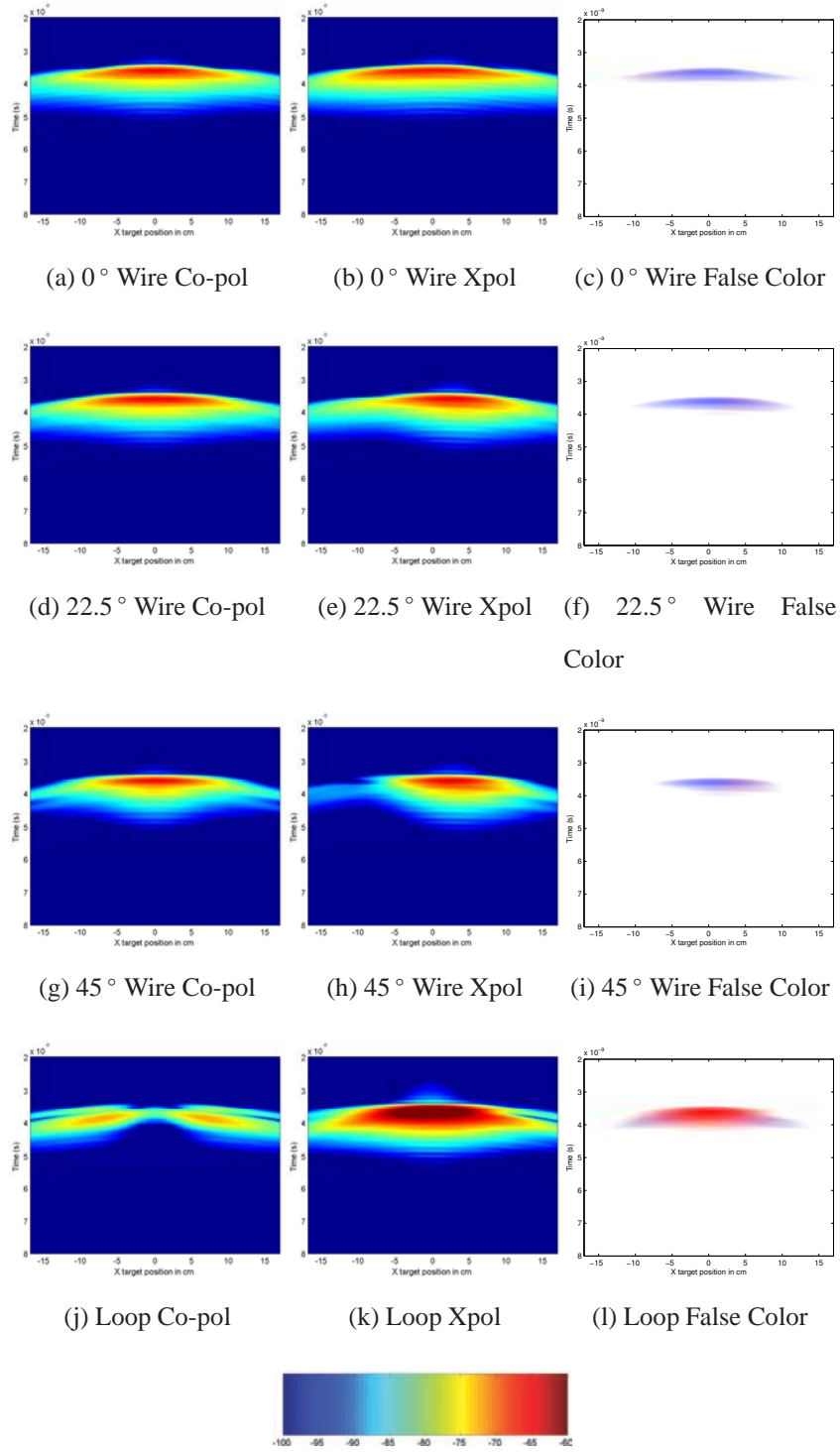
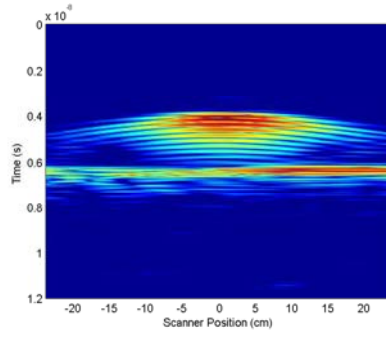
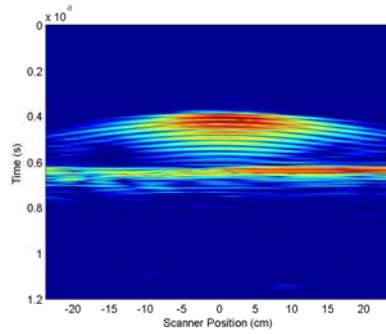


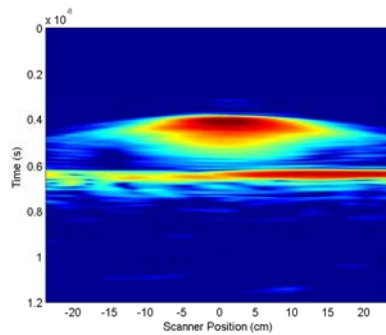
Figure 24: Numerical results for wire targets rotated  $0^\circ$ ,  $22.5^\circ$  and  $45^\circ$ , as well as a loop target. The left-most column figures are the co-polarized signals in dB. The center column figures are the cross-polarized signals in dB. The right-most column figures are the false color mapped signals.



(a) Normal Signal



(b) Hilbert Transform



(c) Signal Envelope

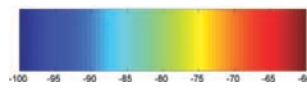


Figure 25: Examples of normal, Hilbert transform, and enveloped signals. These examples are from measurements of a wire target in air.

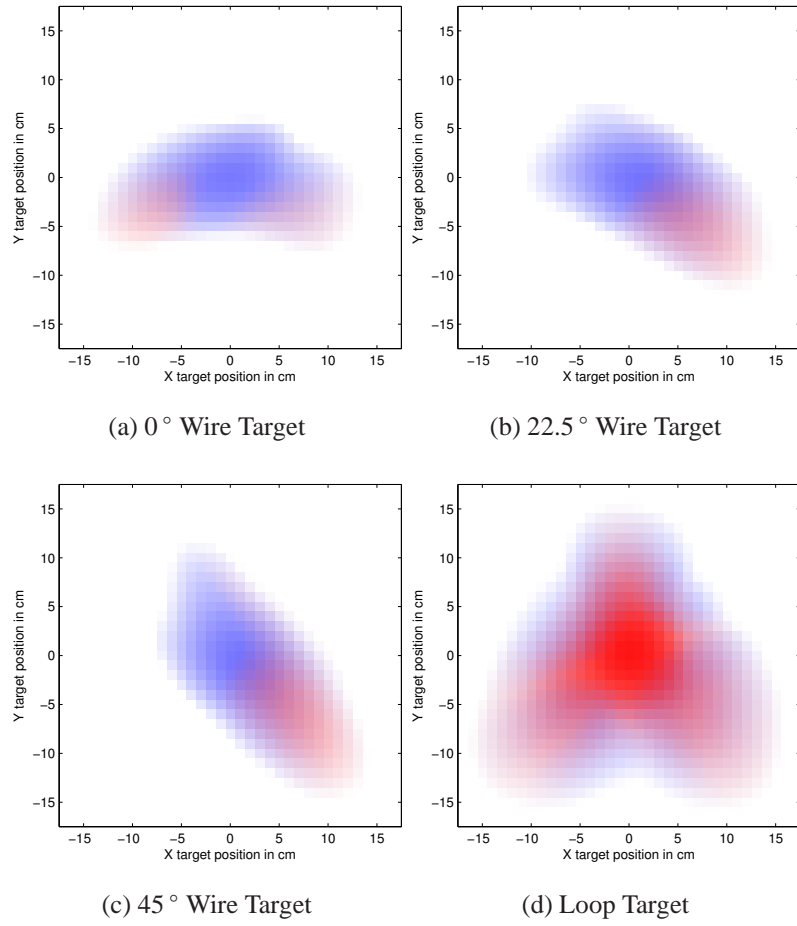


Figure 26: False color maps indicating the detection of targets. White indicates that no target is detected, blue indicates that a linear type of target has been detected, and red indicates that a radially symmetric type of target has been detected.

## CHAPTER 3

### EXPERIMENTAL RESULTS FOR THE DUAL CP ANTENNA

An antenna was built to match the geometry used in the NEC2d model as much as possible [42]. A set of RVDs were made on thin Kapton Printed Circuit Boards (PCBs) with surface-mount resistors on the RVD arms. The RVD PCBs are adhered onto the balun PCBs. Each balun PCB has a double-Y balun on a 1.016 mm thick FR4 PCB. The PCBs were designed with slots in them so that they can fit together in the configuration from the NEC2d models. There is also a back piece for holding all four PCBs together. A photograph of the RVD-based CP antenna is shown in Figure 27.

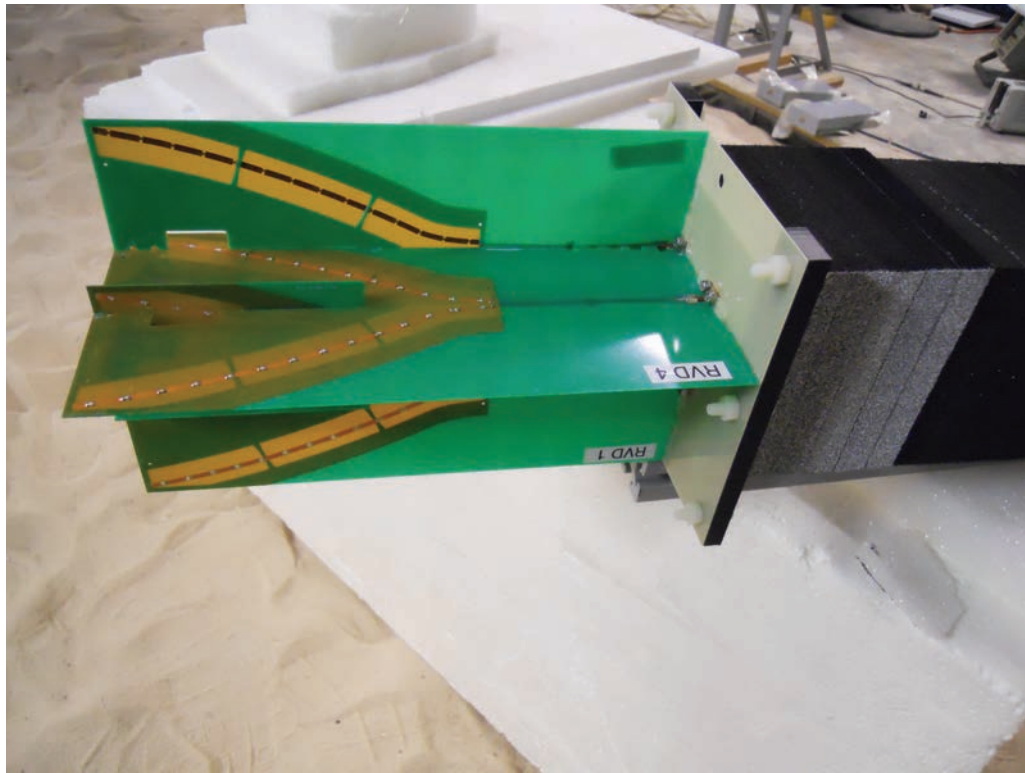


Figure 27: Photograph of the RVD-based circularly polarized antenna.

The antenna was attached to a mount, which attaches to the 3D positioner. The positioner is over the indoor sandbox. The positioner allows the antenna to be accurately positioned in space. The positioner is also capable of slowly moving the antenna down

scanning lanes. Measurements can be made regularly throughout the scan to obtain measurements covering a 2D grid. The antenna position is recorded with the help of encoders. The encoders attach to the motors that drive the positioning system. The X- and Y- positions can then be calculated from the recorded encoder readings.

The antenna is connected to the network analyzer using 2-meter-long Sub-Miniature version A (SMA) cables. There are four cables, each one connecting an RVD feed to a network analyzer port. The cables are bundled together with plastic zip ties to reduce radiation from the cables. At the antenna end of the cables, blocks of electromagnetic absorber are used to reduce radiation between the cables.

The network analyzer used is an Agilent Technologies E5071C. The network analyzer measures the S-parameters for the desired frequencies. In these experiments the measured frequencies were swept from 10 MHz to 8 GHz in 10 MHz steps.

The S-parameters  $S_{21}$ ,  $S_{23}$ ,  $S_{41}$ , and  $S_{43}$  are measured sequentially while the positioner moves the antenna along the scanning lanes. Since the measurements are all occurring while the antenna is moving, the antenna is not in exactly the same position for each of the four S-parameter measurements. This could result in S-parameter measurements that do not result in very good circular polarization when combined. In order to avoid this problem, the positioner speed was slowed down. The network analyzer records a sequence of four S-parameter measurements in approximately one second. The positioner was set to move less than 0.5 cm per second, so the antenna position varies by less than one centimeter over a sequence of S-parameter measurements. The network analyzer was programmed to include a delay between measuring sequences of S-parameters to allow time for the positioner to move approximately one centimeter. After the measurements are done, the data set is interpolated to obtain measurement data at the desired measurement positions.

The first goal of the experiments is to validate the numerical model for the RVD-based CP antenna. The second goal of the experiments is to demonstrate the value of the RVD-based CP antenna in GPR applications. The RVD-based CP antenna should be able to

detect buried wires and allow identification of wire targets.

In Section 3.1 measurements are presented for targets in air. In Section 3.2 targets are measured in the ground. Targets are measured in air first because it is a simpler experiment that is not affected by the ground scattering. The prototype antenna should not be used to measure ground targets until it is shown to work well for targets in air.

### 3.1 Targets in Air

For the experiments for targets in air, each target was placed on top of a styrofoam pedestal. Using the positioner, the antenna was elevated to 10 cm above the pedestal. A photograph of the experiment setup is shown in Figure 28.

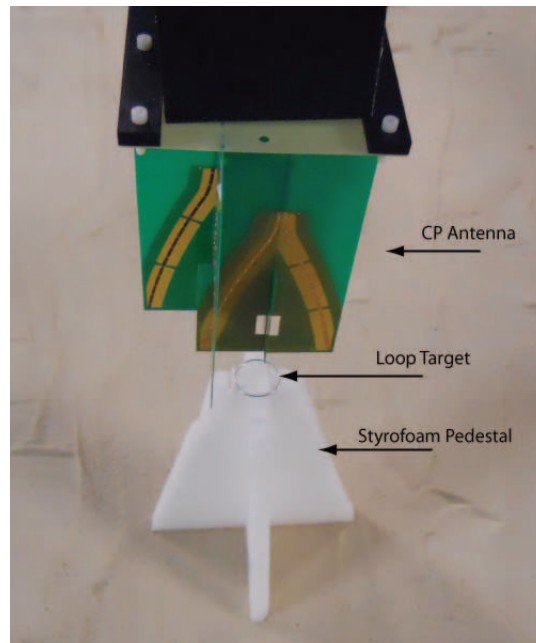


Figure 28: Photograph of the setup for the air experiments.

Due to the low response of the styrofoam pedestal, the targets on top of the pedestal appear to be surrounded by air on all sides. The ground surface is visible in the results at later times than the targets. The ground surface should be a radially symmetric target when it is completely flat, so it should have a high cross-polarization response, a low co-polarization response, and it should be red on the false color maps.

### 3.1.1 Wire Targets and Loop

A  $0^\circ$  wire, a  $22.5^\circ$  wire, a  $45^\circ$  wire, and circular wire loop were scanned in air. The angles are measured relative to the X-direction. The center-lane Y-direction scan results are shown in Figure 29. The response from the ground surface can be seen at approximately 6.5 ns. The results were processed as in Chapter 2. The measurements were made from 10 MHz to 8 GHz in 10 MHz steps, and the pulse was a differentiated Gaussian with a center frequency of 2.5 GHz. The signal envelopes were computed for the figures. In Figure 29 the co-polarized responses are shown in the left column of figures, the cross-polarized responses are shown in the center column of figures, and false color maps are shown in the right column of figures. In each graph the ground appears like a radially symmetric target as expected. The wires are linear targets, so they should have almost even cross-polarized and co-polarized responses, and they should appear blue in the false color maps. The wires appear just like a typical linear target at all three orientations. The loop is a radially symmetric target, and it appears exactly like a radially symmetric target in the experiments.

Top-down false color maps for the four targets are shown in Figure 30. The responses from the ground surface have been time-gated out. The maximum values for the enveloped co-polarization and cross-polarization responses were used to determine the color at each scanning position.

In the air experiments, all three wire targets have even co-polarization and cross-polarization responses. All three wire targets appear blue in the false color maps. In Figure 30d the  $45^\circ$  wire target has a little bit of red in it, but it is mostly blue. The loop target has a low co-polarization response, a high cross-polarization response, and the loop appears red in the false color maps. All four targets have been detected and properly identified in the air experiments. The air experiment results agree with the numerical results in Figure 24 and Figure 26.



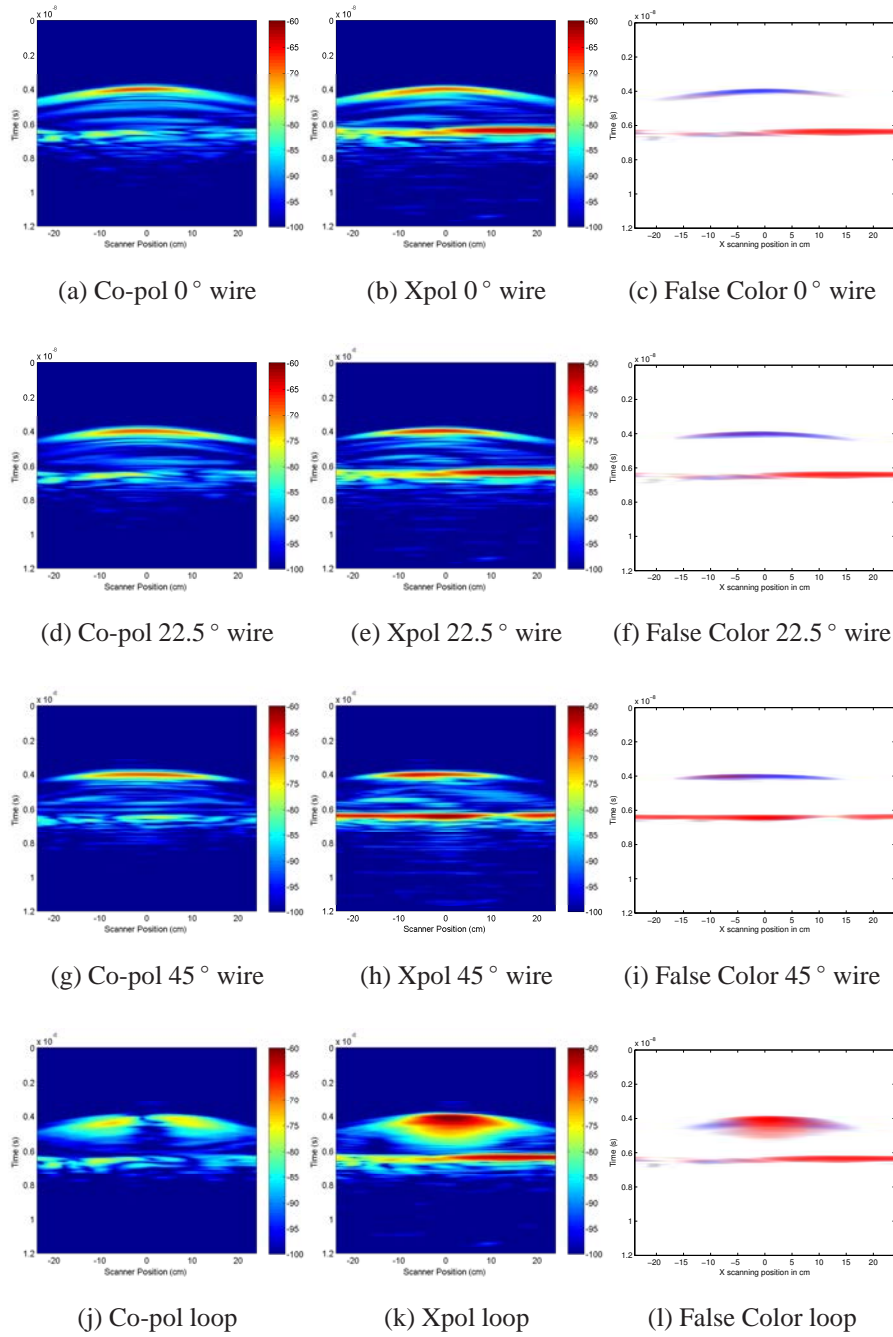


Figure 29: Results for scans over targets in air. The first column of figures has pseudocolor graphs in dB for the co-polarization responses. The second column of figures has pseudocolor graphs in dB for the cross-polarization responses. The third column of figures has false color maps.

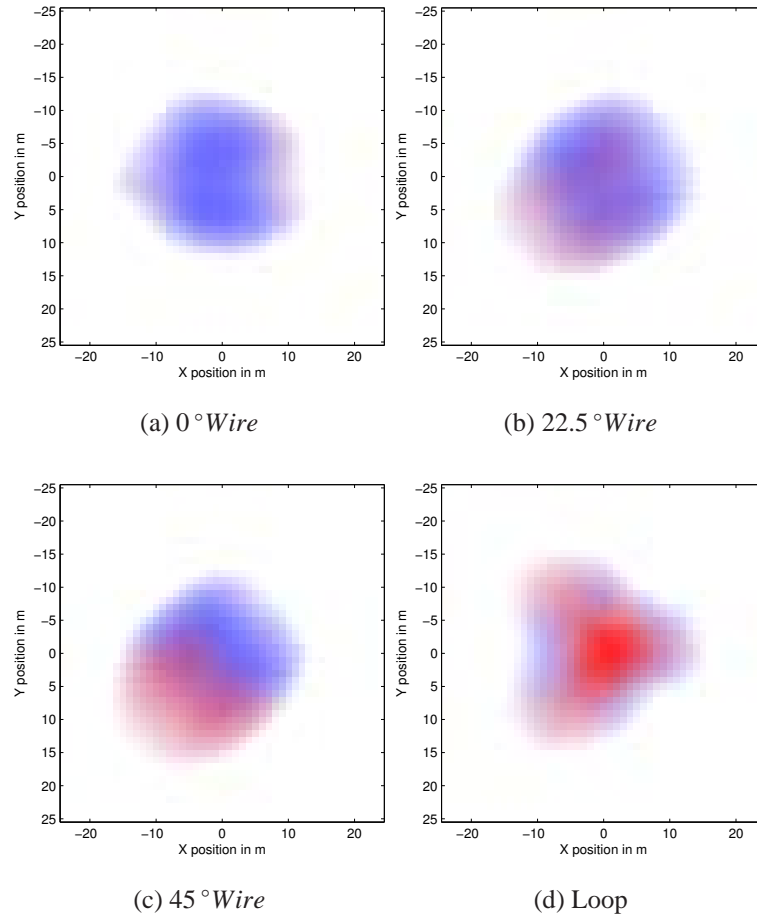


Figure 30: False color maps for a  $0^\circ$  wire, a  $22.5^\circ$  wire, a  $45^\circ$  wire, and circular wire loop that were scanned in air.

### 3.1.2 Metal Sphere Target

A metal sphere target was also detected in air. The sphere has a diameter of 5.08 cm. The sphere is a radially symmetric target, so it should have responses that are similar to those of the loop.

The center-lane co-polarization response, cross-polarization response and false color map are shown in Figure 31. As predicted, the metal sphere has a high cross-polarization response, a low co-polarization response, and appears red on the false color map.

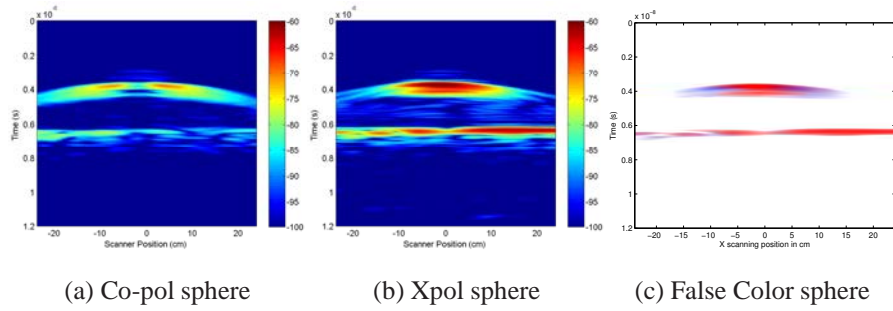


Figure 31: Results for scans over the metal sphere target in air.

The top-down false color map for the metal sphere is shown in Figure 32. The sphere appears a very bright red when the antenna is directly over the sphere. The sphere has some blue at the edges of the false color pattern, but the false color map unmistakably indicates that the sphere is a radially symmetric target.

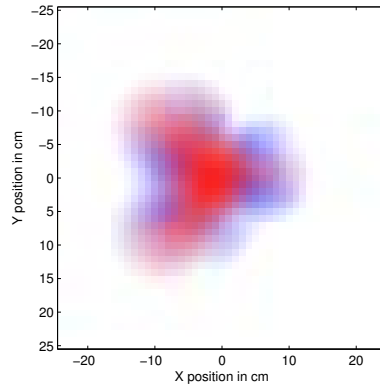


Figure 32: False color map for a metal sphere target in air.

### 3.2 Targets in Ground

Experiments were performed with targets buried beneath the surface of the sand. The surface of the sand was leveled and smoothed. The positioner was used to lower the antenna to a height of 11.43 cm above the surface of the sand. The targets were buried 10.16 cm beneath the surface of the sand. The target responses are weaker than the responses for targets in air due to the slightly greater target distance and attenuation in the sand.

### 3.2.1 Wire and Loop Targets

The  $0^\circ$  wire, a  $22.5^\circ$  wire, a  $45^\circ$  wire, and circular wire loop were buried in the sand and scanned between 10 MHz and 8 GHz in 10 MHz steps. The center-lane scan results are shown in Figure 33. The response from the ground surface can be seen at approximately 4.3 ns. The ground surface appears red in these experiments. The wire targets appear blue in the false color maps, and the loop target appears red. The responses are weaker than for the targets in air because there is loss from propagation in the sand.

Center-lane false color maps along the X-direction are shown in Figure 34. These figures provide an orthogonal view of the targets. The  $0^\circ$  wire target now appears as a line rather than a hyperbola because it is aligned with the scanning direction. In order to lower the response of the ground and improve target visibility, the measurements along the perimeter of the scanning area were averaged and then subtracted from each measurement. When the antenna moves parallel to the wire target as measurements are performed, the distance between the antenna and the wire remains fixed until the antenna moves past the ends of the wire. When the antenna moves orthogonally to the wire target, the distance between the antenna and the wire reaches a minimum when the antenna is directly over the wire. As the distance of the wire target increases, the response of the wire target occurs later in time.

Top-down false color maps for the buried targets are shown in Figure 35. The responses from the ground surface have been time-gated out. The three wire targets appear blue in the false color maps and the loop target appears red. This shows that geometry classification is still successful when the targets are buried.

There are some small issues with the results for the buried targets. Some of the wire targets appear slightly red in the false color maps. In these instances the co-polarization and cross-polarization are not quite equal, but the co-polarization response is still much larger than the cross-polarization response of a radially symmetric target. Overall, the buried target results show that the RVD-based CP antenna is capable of detecting buried targets

and discriminating between them based on geometry type.

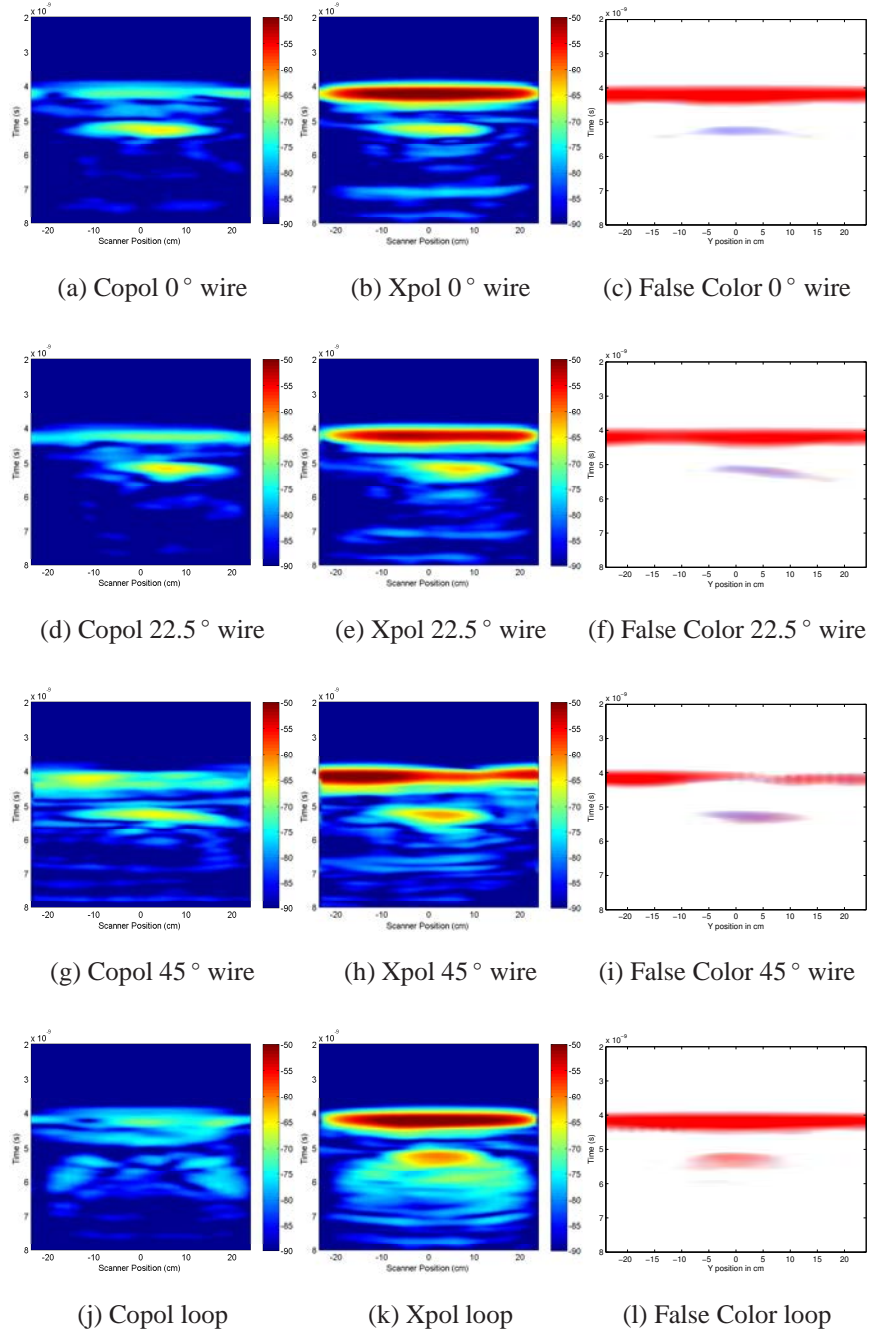


Figure 33: Results for scans over targets in the ground. The first column of figures has pseudocolor graphs in dB for the co-polarization responses. The second column of figures has pseudocolor graphs in dB for the cross-polarization responses. The third column of figures has false color maps.

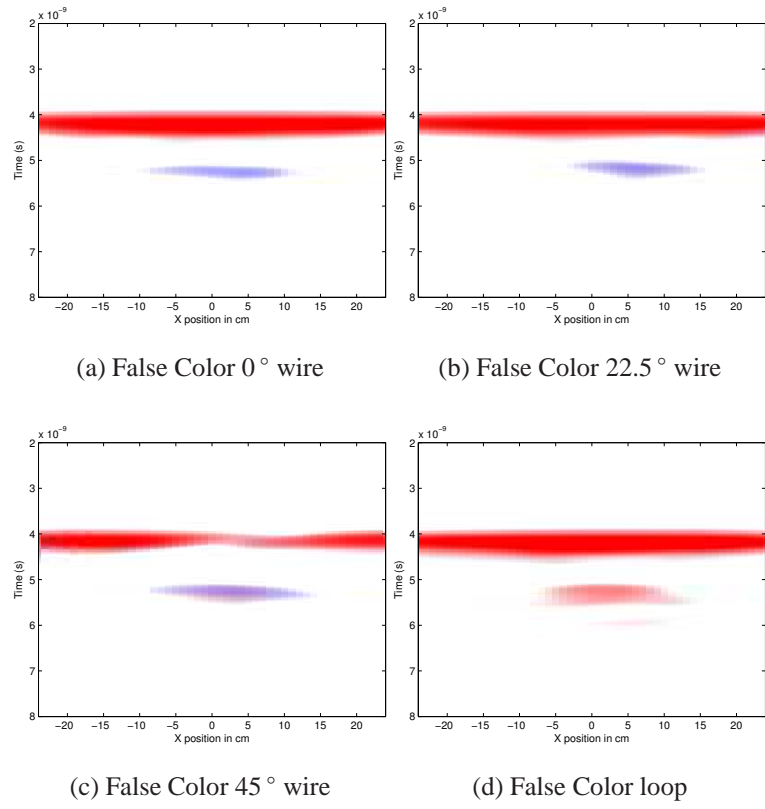


Figure 34: Results for scans over targets in the ground in the X-direction.

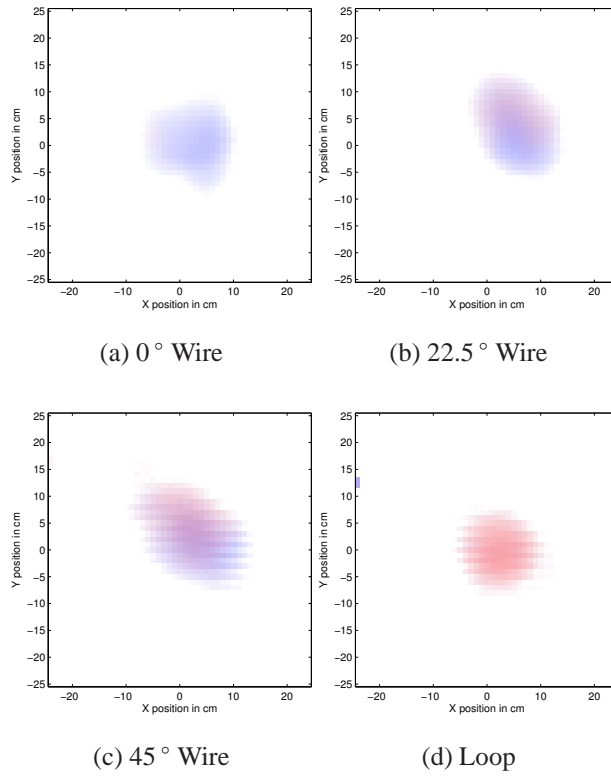


Figure 35: False color maps for a  $0^\circ$  wire, a  $22.5^\circ$  wire, a  $45^\circ$  wire, and circular wire loop that were scanned in the ground.

### 3.2.2 Metal Sphere Target

The center-lane co-polarization response, cross-polarization response and false color map for the buried metal sphere target are shown in Figure 36. The sphere is a radially symmetric target, just like the loop, so it should have a high cross-polarized response, a low co-polarized response, and it should appear red on the false color map. The results show that it looks similar to the loop target, except that its response is stronger. The response is likely stronger because the sphere is a larger target.

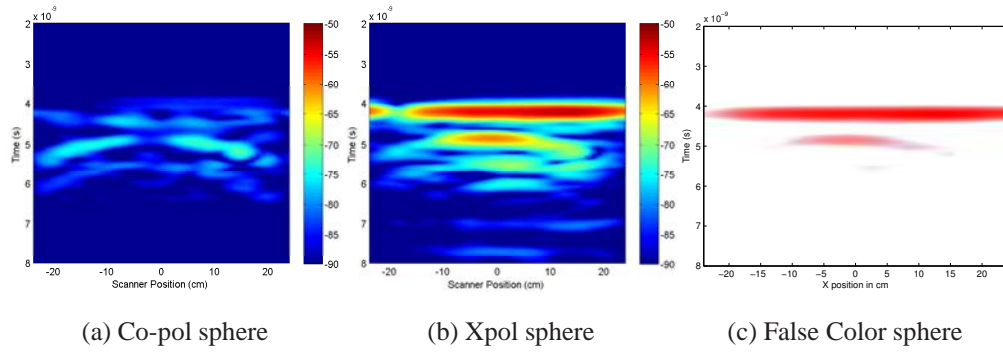


Figure 36: Results for scans over the metal sphere target in the ground.

A Y-direction center-lane scanning results are shown in Figure 37. Since the sphere has radial symmetry, the response for the sphere should be nearly the same in the Y-direction and X-direction.

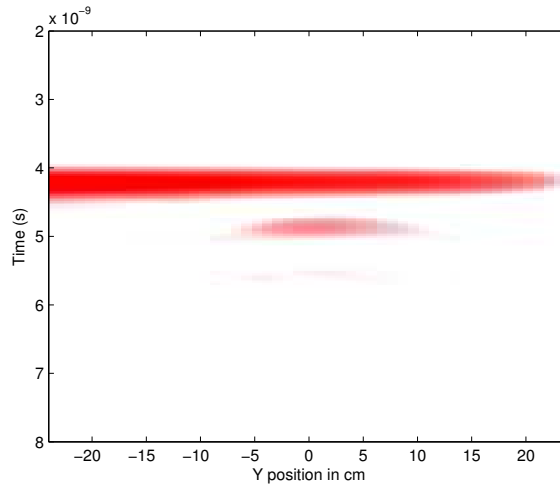


Figure 37: Y-direction scan over the buried loop target.

The top-down false color map for the metal sphere is shown in Figure 38. As predicted, the metal sphere has a high cross-polarization response, a low co-polarization response, and appears red of the false color map.



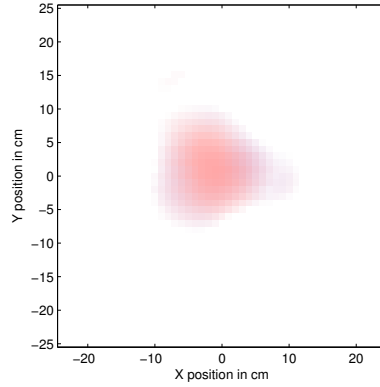


Figure 38: False color map for a metal sphere target in the ground.

The results for the buried metal sphere target indicate that the sphere can be easily identified as a radially symmetric target.

### 3.3 Targets in Ground with Clutter

In this section, the effects of ground clutter are investigated. Experiments were performed with several types of targets. The targets are buried and scanned as in the Section 3.2. One of the goals for the antenna is to have low target interaction. If multiple targets are buried fairly close together, then the antenna should be able to distinctly detect each of the targets. Also, each target should have the same geometry classification as it would if it were the only target present. The clutter experiments are done to find instances when a false alarm or missed target of interest might occur.

#### 3.3.1 Buried Sphere

Experiments were performed with the metal sphere target. A photograph of the metal sphere is shown in Figure 39.



Figure 39: A photograph of a metal sphere used in the clutter experiments.

Results for the sphere in air are in Section 3.1.2. Results for the buried sphere are in Section 3.2.2.

An experiment was performed with both the metal sphere and the wire buried in the ground. A diagram for the relative locations of the buried sphere and wire is shown in Figure 40. The results of this experiment are shown in Figure 41. The sphere and the wire targets are easily identifiable. When the antenna is directly between the wire and the sphere, the targets are about the same distance from the antenna, and the responses overlap.

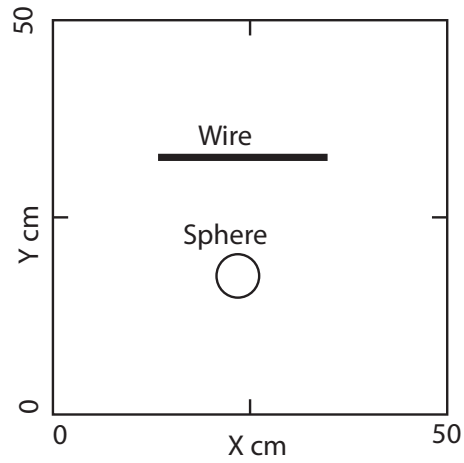
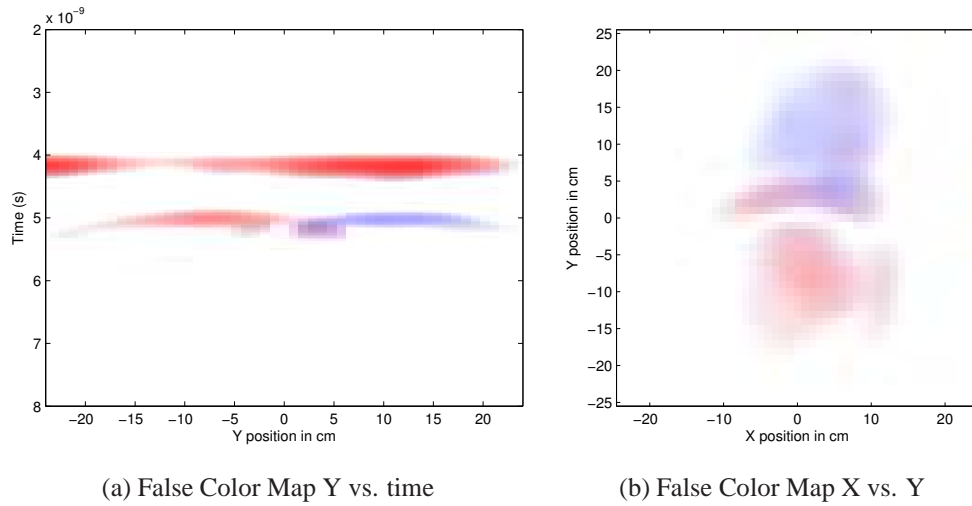


Figure 40: A diagram for the buried sphere and wire experiment.



(a) False Color Map Y vs. time

(b) False Color Map X vs. Y

Figure 41: Results for scans over the sphere and wire targets in the ground.

An experiment was performed with five metal spheres and two wires buried in the sand. Two of the metal spheres were the same size as the one in the previous experiment, and the other three were half of the diameter of that sphere. A diagram for the relative locations for all of the buried spheres and wires is shown in Figure 42. The results for this experiment are shown in Figure 43. In Figure 43b it is difficult to see individual targets or clearly see the wire targets. In Figure 43a it is easier to see the wire targets. From Figure 43b the

presence of both linear targets and radially symmetric targets can be seen, but it is difficult to determine the number of targets or their positions. With so many sphere targets buried close together, it is difficult to clearly see each sphere target.

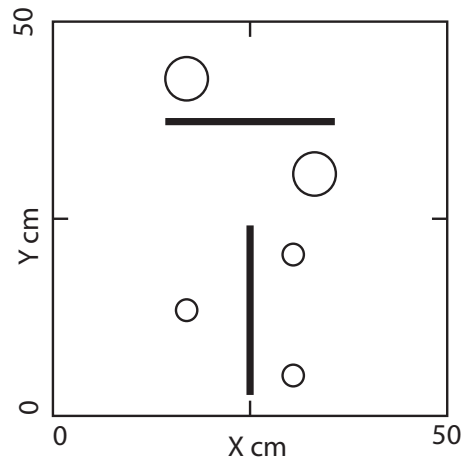


Figure 42: A diagram for the experiment with multiple buried spheres and wires.

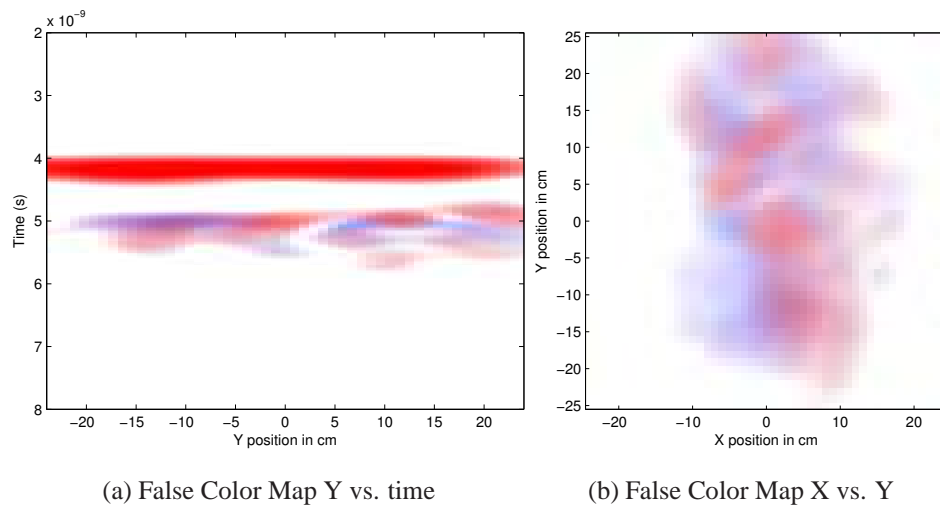


Figure 43: Results for scans over the sphere targets and wire targets buried together in the ground.

### 3.3.2 Buried Rocks

Rocks are often in the ground, so examining the effects of rocks would be useful for GPR. For the following experiments, rocks were buried in the sand. A picture of one of the rocks from the experiment is shown in Figure 44. The rock is expected to be a radially symmetric target because it has a fairly large size. The irregularities and asymmetries in the shape of rock may cause it to behave less like a perfectly radially symmetric target.



Figure 44: A photograph of a rock used in the clutter experiments.

An experiment was performed with just a single buried rock. Center-lane results for the rock are shown in Figure 45. The rock appears like a weak radially symmetric target. It has a low co-polarized response. It has high cross-polarized response, but it is not as high as the response of the loop. The rock appears soft red on the false color map, indicating that it is a radially symmetric target with a relatively weak response.

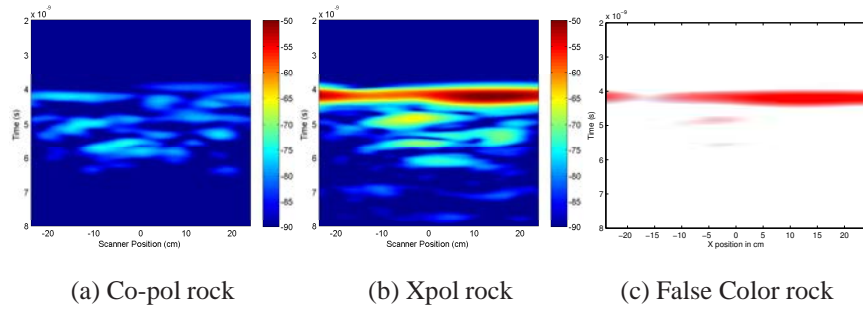


Figure 45: Results for scans over the rock target in the ground.

The top-down false color map for the buried rock is shown in Figure 46. The rock appears soft red over a fairly small area on the false color map.

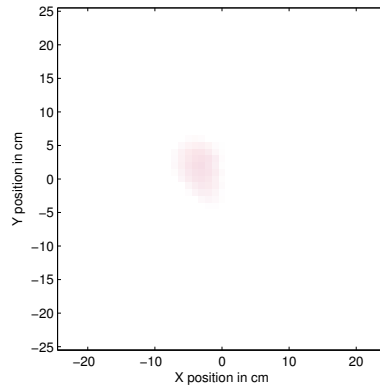


Figure 46: False color map for a rock target in the ground.

An experiment was performed with a rock buried 10 cm away from a wire target. A diagram for the positions of the rock and the wire is shown in Figure 47. False color maps for the buried rock and wire are shown in Figure 48. Y vs. time measurements are shown instead of X vs. time, because both target responses overlap over the X vs. time center-lane. The rock is a weak radially symmetric target. It is easiest to distinguish between the response of the rock and the response of the wire in Figure 48a.

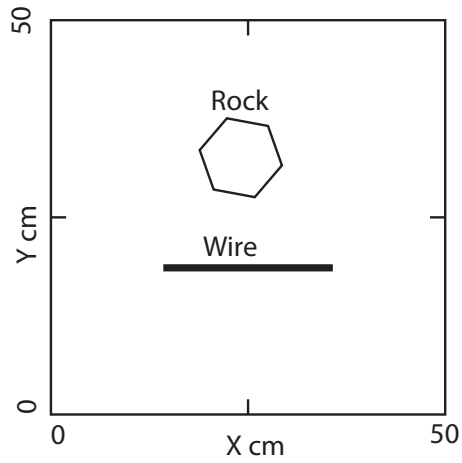


Figure 47: A diagram for the buried rock and wire experiment.

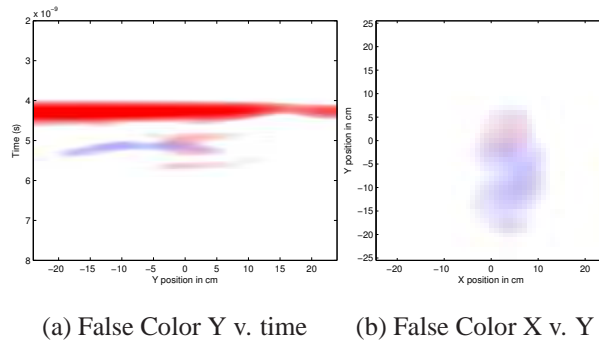


Figure 48: Results for scans over the single rock target and wire target together in the ground.

An experiment was performed with 2 wires and 12 rocks buried in the scanning area. A diagram for the positions of the rocks and the wires is shown in Figure 49. False color maps for this experiment are shown in Figure 50. Both blue and red areas can be seen in Figure 50, but it is difficult to see individual targets due to the high concentration of buried objects.

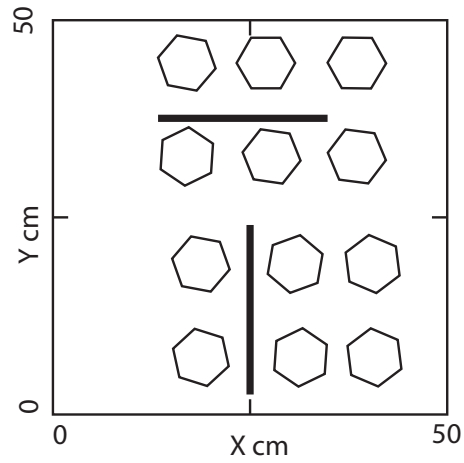


Figure 49: A diagram for the experiment with multiple buried rocks and wires.

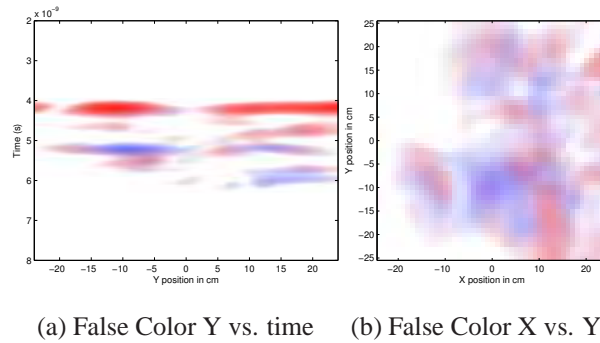


Figure 50: Results for scans over the multiple rock targets and wire targets buried together in the ground.

Another experiment was performed with the wire targets removed and the rock targets unmoved. A diagram for this experiment is shown in Figure 51. The false color maps for this experiment are shown in Figure 52. By comparing the results of these two experiments, the wire targets are responsible for most of the blue on the false color maps, but the rocks sometimes appear a little blue on the false color map.



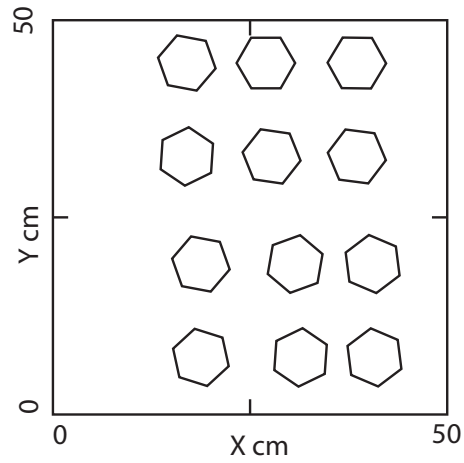


Figure 51: A diagram for the experiment with multiple buried rocks but without the wires.

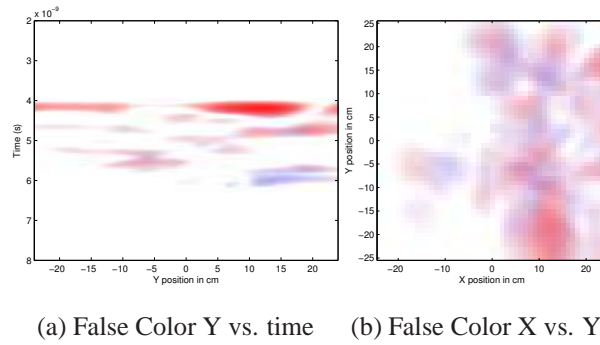


Figure 52: Results for scans over the multiple rock targets without the wire targets.

### 3.3.3 Buried Wooden Board

Experiments were performed with a wooden block buried in the sand. The wooden block is 63 mm by 353 mm by 36 mm. Since the wooden block has large flat rectangular faces, it is expected to be a radially symmetric target. It should have a high cross-polarized response, a low co-polarized response, and it should appear red on the false color map. A photograph of the wooden block is shown in Figure 53.



Figure 53: A photograph of a wooden block used in the clutter experiments.

A experiment was performed with the wooden block and no other targets buried in the sand. The side of the wooden block that faced the antenna was 63 mm by 353 mm. Results for the wooden block are shown in Figure 54. The wooden block is in fact a radially symmetric target, but the response of the wooden block is weak compared to the responses of the loop and sphere targets.

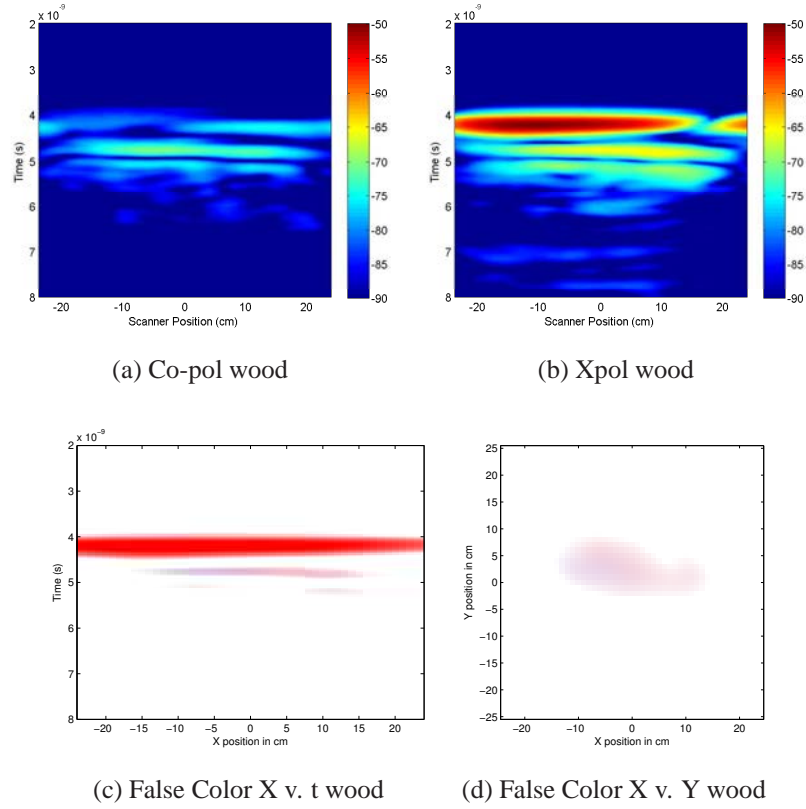


Figure 54: Results for scans over the wooden block target in the ground.

Another experiment was performed with the wooden block rotated. The 36 mm by 353 mm side faced the antenna for this experiment. The results for this experiment are shown in Figure 55. With the narrower side of the wooden block facing the antenna, the wooden block could appear more like a linear target. In Figure 55 the wooden block still behaves as a radially symmetric target, so it is not quite narrow enough to appear as a linear target.

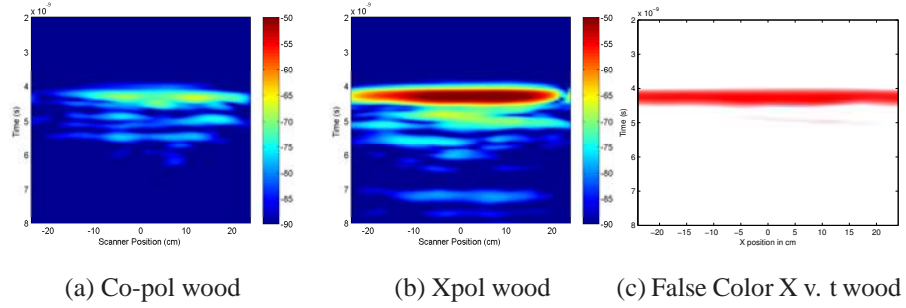


Figure 55: Results for scans over the wooden block target in the ground. The narrow side of the wooden block was facing upwards towards the antenna.

An experiment was performed with both a wooden block and a wire buried in the ground. A diagram for the relative locations of the buried wooden block and wire is shown in Figure 56. The results for this experiment are shown in Figure 57. The wire target appears as a strong blue on the false color map, while the wooden block appears as a soft red on the false color map.

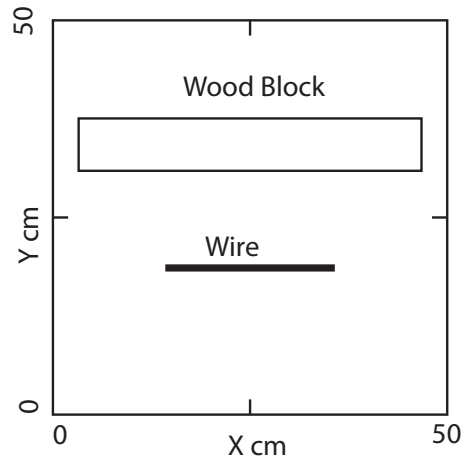
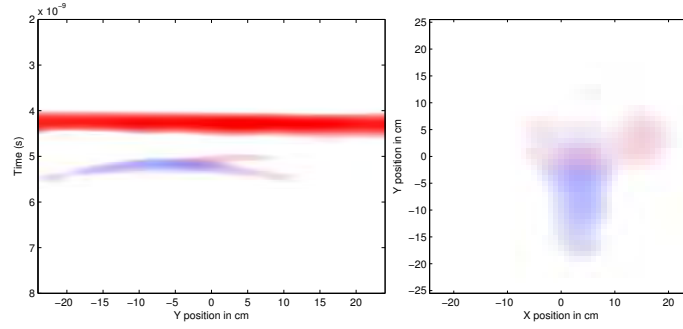


Figure 56: A diagram for the buried wooden block and wire experiment.



(a) False Color Map Y vs. t (b) False Color Map X vs. Y

Figure 57: Results for scans over the wooden block and wire targets in the ground.

### 3.3.4 Buried Aluminum Can

Experiments were performed using an aluminum can. A photograph of the can is shown in Figure 58. The can is expected to be radially symmetric target. The large size of the can makes the can appear locally like a flat surface. The can is almost a cylinder, and the wire targets are actually thin metal cylinders. Although they are both cylinders, the wire target is a linear target, and the can is a radially symmetric target. Therefore, the radius of the cylinder greatly affects the co-polarized and cross-polarized scattering. This motivates the cylinder thickness analysis in Section 3.4.



Figure 58: A photograph of an aluminum can used in the clutter experiments.

An experiment was performed with only the can buried in the ground with the cylindrical side of the can facing the antenna. The results of this experiment are shown in Figure 59. The results show that the aluminum can is a radially symmetric target, much like the metal sphere.

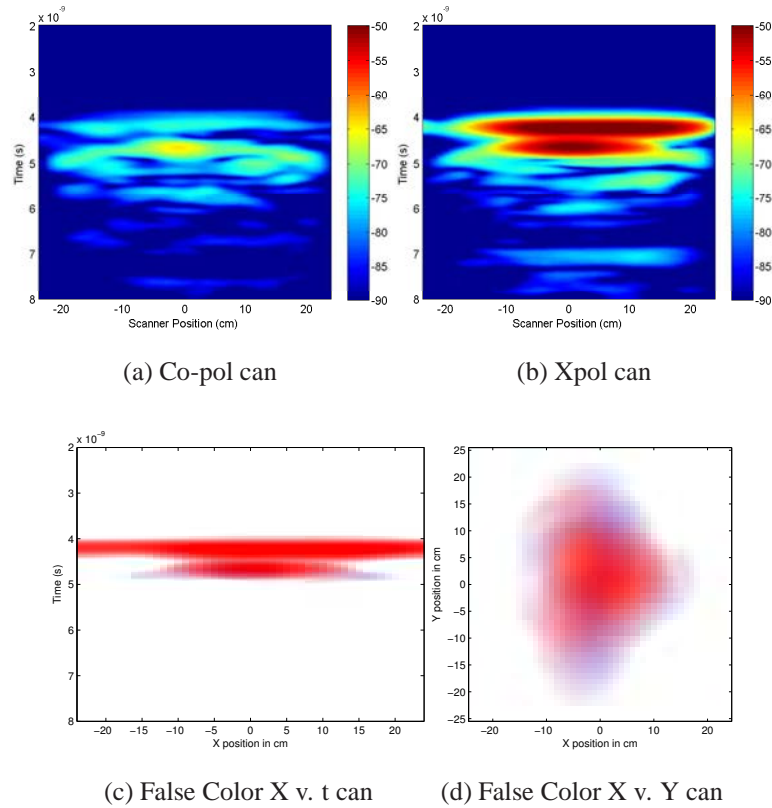


Figure 59: Results for scans over the aluminum can target in the ground.

Another experiment was performed with the top of the can facing the antenna. The results of this experiment are shown in Figure 60.

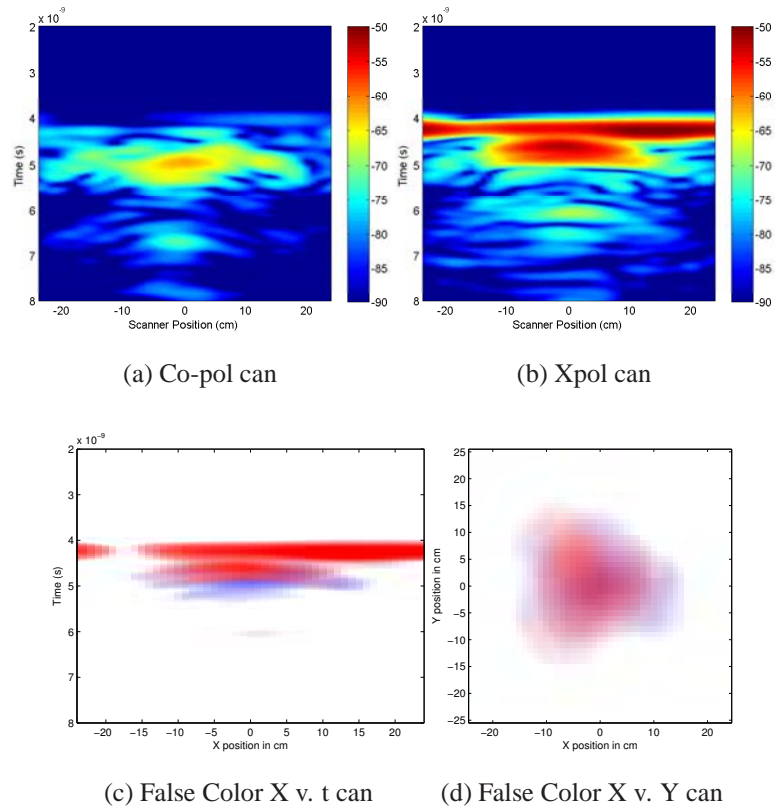


Figure 60: Results for scans over the aluminum can in the ground. The top of the can faced upwards towards the antenna.

An experiment was performed with both the can and a wire in the ground. A diagram for the positions of the buried aluminum can and wire is shown in Figure 61. The results for this experiment are shown in Figure 62. Both targets are clearly visible and properly categorized on the false color map.

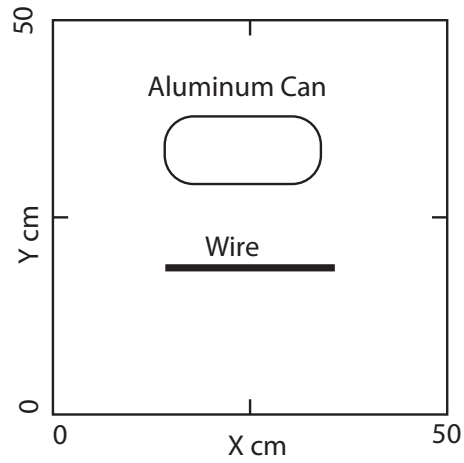


Figure 61: A diagram for the buried can and wire experiment.

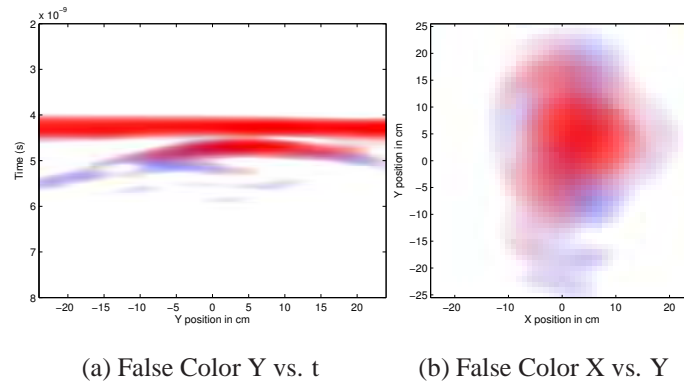


Figure 62: Results for scans over the aluminum can and wire targets in the ground.

### 3.3.5 Buried Land mine

Experiments were performed with a small anti-personnel land mine. The land mine is inert so that it is safe for testing. A photograph of the land mine is shown in Figure 63. The land mine is expected to be a radially symmetric target because it has radial symmetry.





Figure 63: A photograph of a land mine used in the clutter experiments.

An experiment was performed with both a land mine and a wire buried in the sand, 10 cm apart. A diagram for the positions of the buried land mine and wire is shown in Figure 64. The results of this experiment are shown in Figure 65. The responses of the land mine indicate that it is a radially symmetric target. Both targets are easily detected and have distinct responses in this experiment.

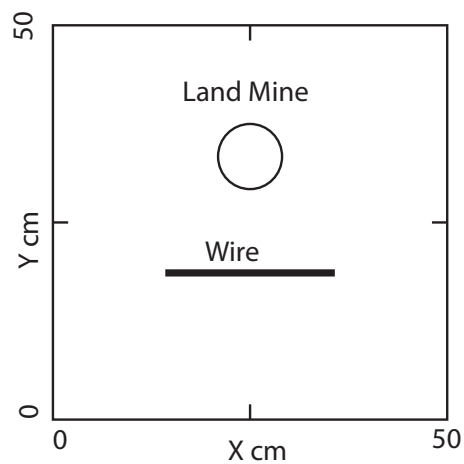
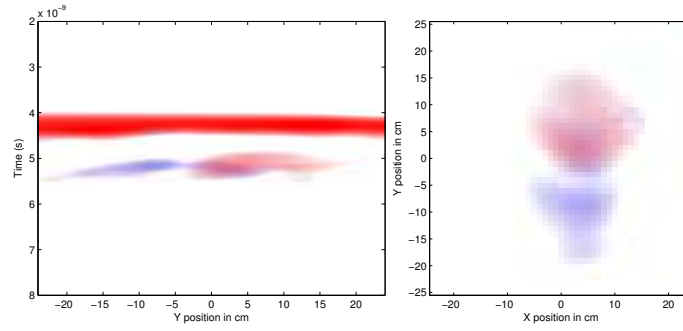


Figure 64: A diagram for the buried land mine and wire experiment.



(a) False Color Y vs. t

(b) False Color X vs. Y

Figure 65: Results for scans over the land mine and wire targets in the ground.

### 3.3.6 Summary

The strengths of the co-polarization and cross-polarization responses for targets in air are shown in Figure 66. These values are based on the boresight measurements in the experiments with targets in air. The wire targets are grouped along the line of equal co-polarization and cross-polarization, and the loop and sphere targets are far away from this line.

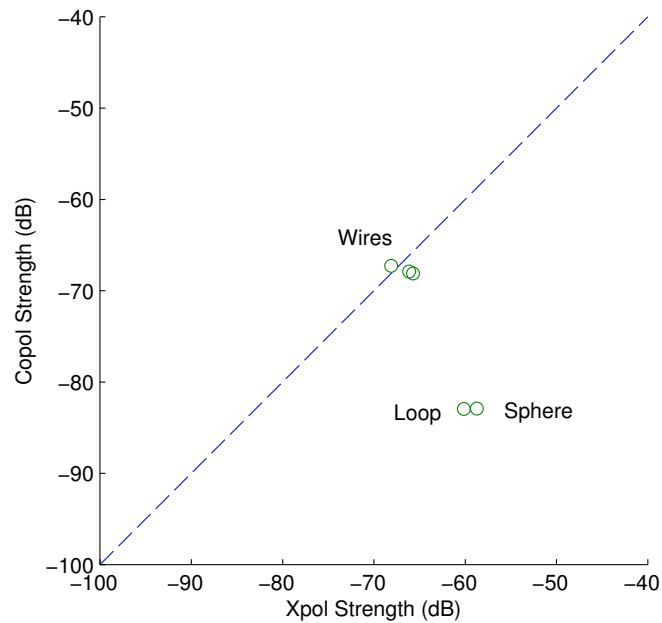


Figure 66: Scatter plot of relative co-polarization and cross-polarization response strength for targets in air.

The strengths of the co-polarization and cross-polarization responses for targets in the ground are shown in Figure 67. Most of the target geometries can be identified from the location of each target in this figure. The wooden block target is difficult to classify because its cross-polarization response is only about 6.7 dB higher than its co-polarization response. The can is far away from the other targets mostly because its response is so strong.

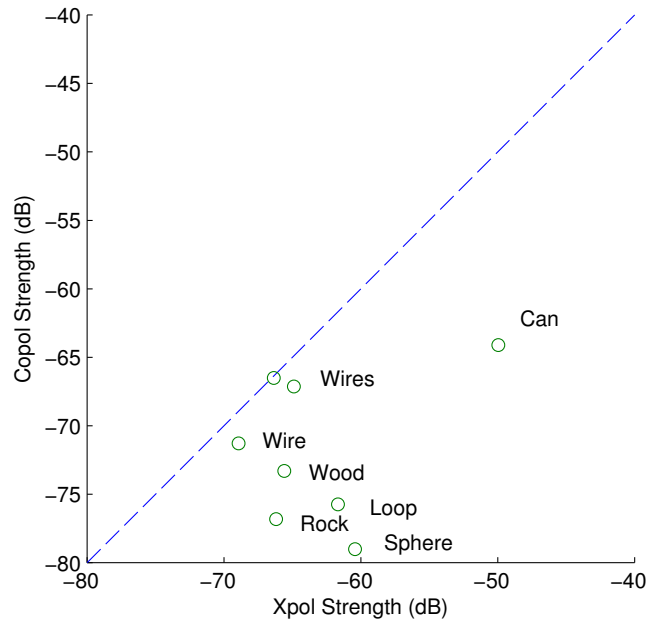


Figure 67: Scatter plot of relative co-polarization and cross-polarization response strength for targets in the ground.

### 3.4 Wire Thickness Analysis

The effect of the wire thickness was examined. A wire is a metal cylinder, although it is not necessarily rigid. A wire is a linear target, and a cylinder of extremely large radius appears locally like a flat metal surface, which is a radially symmetric target. Therefore, whether a cylinder appears as a linear target or a radially symmetric target depends on the radius of the cylinder. The cylinder radius at which the cylinder transitions from a linear target to a radially symmetric target should depend on the wavelengths used.

The wire targets in the previous experiments were 18 Gauge with a diameter of 1.04 mm. An experiment was performed using a 30 Gauge wire target (0.25 mm diameter) to see if such a thin wire a target could still be detected. The wires are each 20 cm long. For large radii cylinders, aluminum cylinders were used in place of wires. Results for scans over the buried 30 Gauge wire target are shown in Figure 68. The wire targets were measured from 10 MHz to 8 GHz in 10 MHz steps. The results were processed according to the procedures

used in the previous sections of this chapter. The co-polarization response along the center scanning lane is shown in Figure 68a. The cross-polarization response along the center scanning lane is shown in Figure 68b. The false color map along the center scanning lane is shown in Figure 68c. The top-down view false color map is shown in Figure 68d. The 30 Gauge wire gives a much weaker response than the 18 Gauge wire, but the 30 Gauge wire can still be detected and properly identified as a wire target. The 30 Gauge wire response is weaker because it is much thinner.

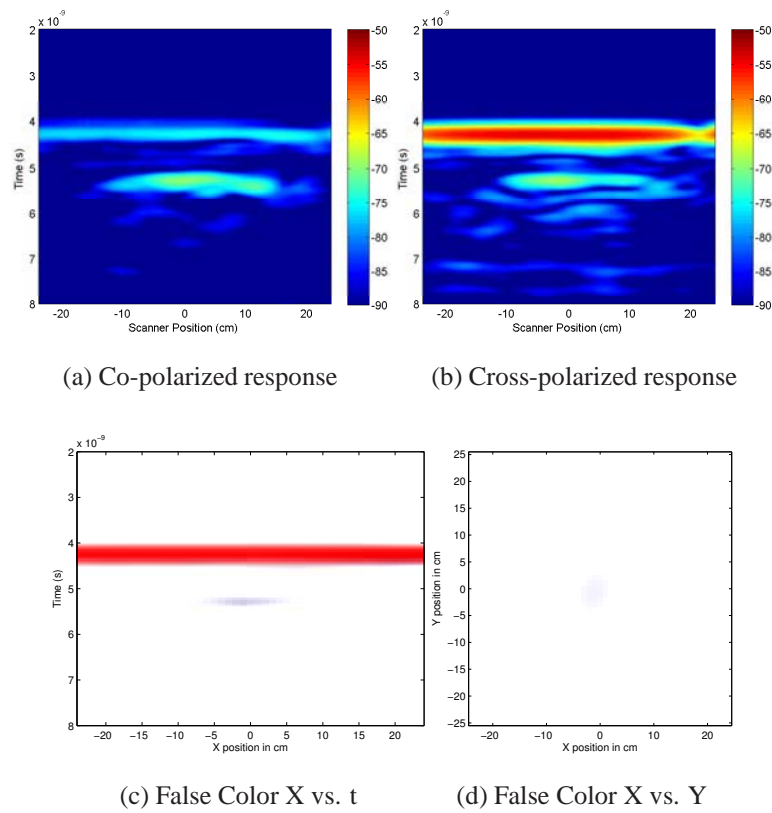


Figure 68: Results for scans over the buried 30 Gauge wire target.

A buried 24 Gauge wire target (0.50 mm diameter) was also scanned. Results for the 24 Gauge wire target are shown in Figure 69. The 24 Gauge wire provides a much stronger response than the 30 Gauge wire, but still slightly weaker than the 18 Gauge wire.

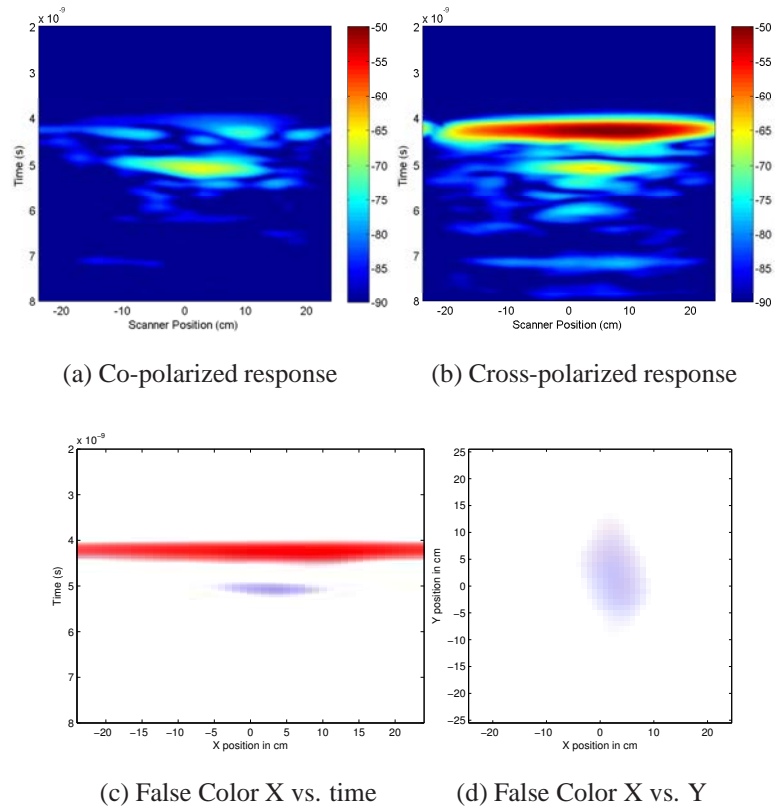
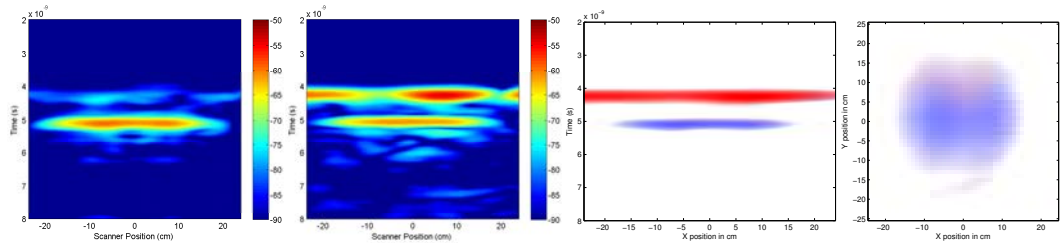
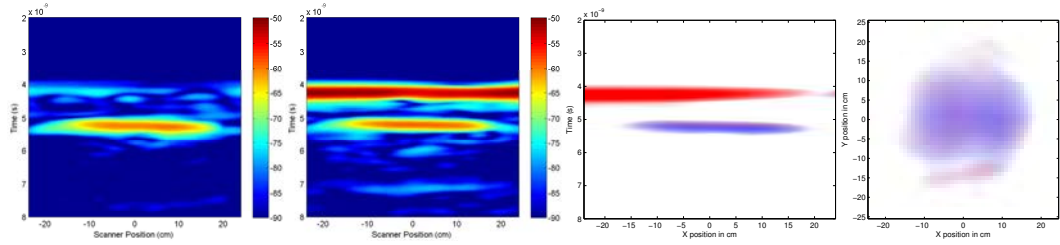


Figure 69: Results for scans over the buried 24 Gauge wire target.

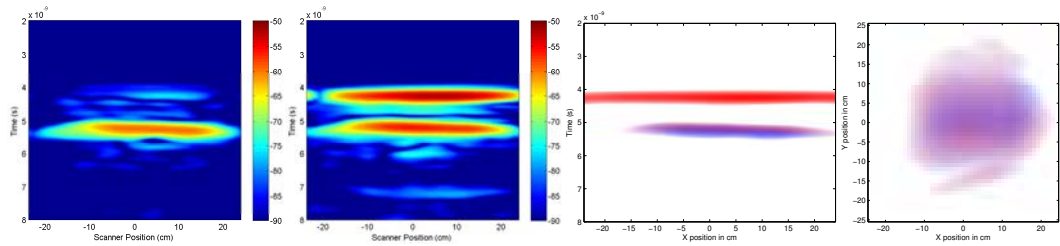
The aluminum cylinders have diameters of 6.35 mm, 9.53 mm, 12.70 mm, 19.05 mm, 25.40 mm and 38.10 mm. The cylinders were buried 10 cm beneath the surface of the sand and then scanned with the RVD-based CP antenna. Co-polarization responses, cross-polarization responses, and false color maps for all of the cylinders are shown in Figure 70 and Figure 71.



(a) Co-pol 6.35 mm Cyl. (b) Xpol 6.35 mm Cyl. (c) False Color 6.35 mm (d) X-Y 6.35 mm

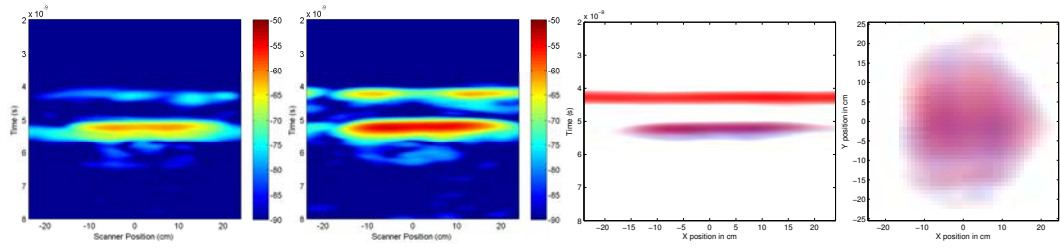


(e) Co-pol 9.53 mm Cyl. (f) Xpol 9.53 mm Cyl. (g) False Color 9.53 mm (h) X-Y 9.53 mm

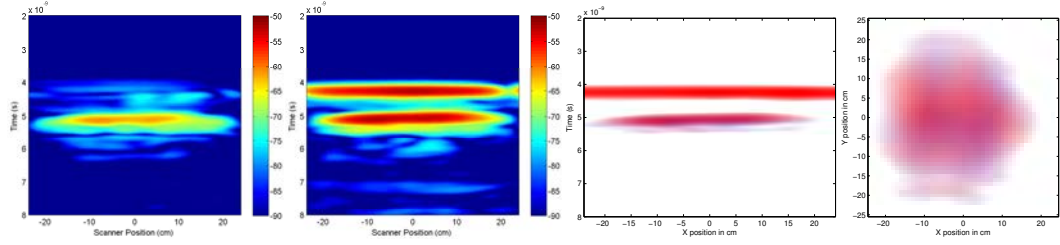


(i) Co-pol 12.70 mm Cyl. (j) Xpol 12.70 mm Cyl. (k) False Color 12.70 mm (l) X-Y 12.70 mm

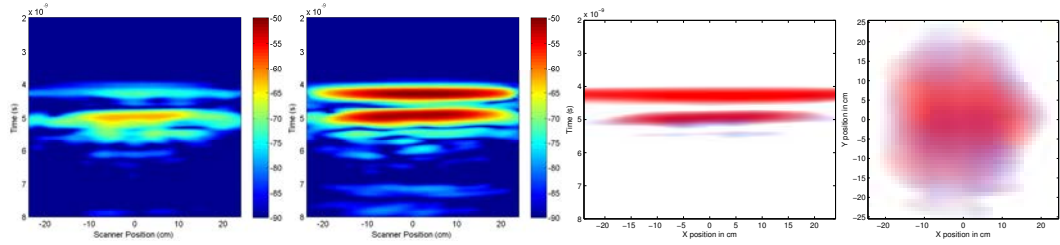
Figure 70: Results for scans over buried cylinder targets. The first row of figures is from results for the 6.35 mm cylinder. The second row of figures is from results for the 9.53 mm cylinder. The third row of figures is from results for the 12.70 mm cylinder.



(a) Co-pol 19.05 mm Cyl. (b) Xpol 19.05 mm Cyl. (c) False Color 19.05 mm (d) X-Y 19.05 mm



(e) Co-pol 25.40 mm Cyl. (f) Xpol 25.40 mm Cyl. (g) False Color 25.40 mm (h) X-Y 25.40 mm



(i) Co-pol 38.10 mm Cyl. (j) Xpol 38.10 mm Cyl. (k) False Color 38.10 mm (l) X-Y 38.10 mm

Figure 71: Results for scans over buried cylinder targets. The first row of figures is from results for the 19.05 mm cylinder. The second row of figures is from results for the 25.40 mm cylinder. The third row of figures is from results for the 38.10 mm cylinder.

The strengths of the co-polarization and cross-polarization responses for the cylinder and wire targets are shown in Figure 72. The wire targets are grouped along the line of equal co-polarization and cross-polarization. The cylinder targets are farther from the line of equal co-polarization and cross-polarization when the diameters increase.



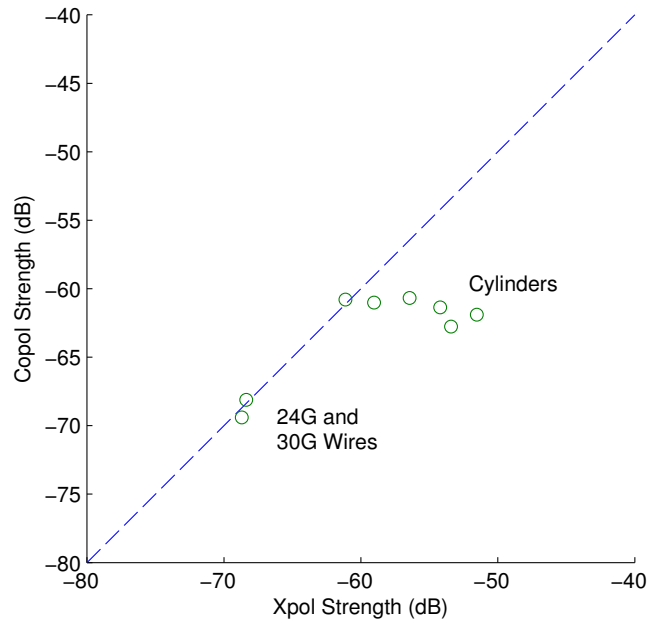


Figure 72: Scatter plot of relative co-polarization and cross-polarization response strength for cylinder and wire targets.

From these results a cylinder appears to begin transitioning from a linear target to a radially symmetric target after the diameter of the cylinder is increased past 12.70 mm. For the results of the 12.70 mm cylinder, there is some ambiguity in the determination of target type. The 12.70 mm diameter cylinder is in between being a linear target and being a radially symmetric target. The center frequency of the pulse is 2.5 GHz, which corresponds to a wavelength of approximately 60 mm in sand. All cylinders with a diameter of at least 19.05 mm, or approximately a quarter wavelength, appear as radially symmetric targets. Although the large cylinders appear as radially symmetric targets, even the 38.10 mm cylinder has a significant co-polarized response. Therefore, a cylinder with a diameter of 38.10 mm has not completely transitioned into becoming a radially symmetric target.

### **3.5 Ground Surface Roughness Analysis**

The effects of ground-surface roughness on dual CP detection were investigated. The ground surface is often neither smooth nor level in many applications. The goal of this investigation is to detect buried wire targets when the ground surface is rough. In order for the RVD-based CP antenna to be useful in a GPR, it should remain effective when the ground surface is not smooth. A rough ground surface may no longer appear as a radially symmetric target, and the responses would likely depend on the local features of the roughness.

For the experiments a 1 meter long wire target was used. Since the scanning area is 50 cm by 50 cm, the ends of the wire are not detected. The wire was buried 10.16 cm beneath the surface of the sand. The wire was placed in the center of the scanning area and aligned in the X-direction. Then the surface of the sand was disturbed to introduce the roughness. The average depth of the wire should remain approximately 10.16 cm.

For the first experiment, many shallow valleys were drawn into the surface of the sand. Photographs of the sand surface are shown in Figure 73.



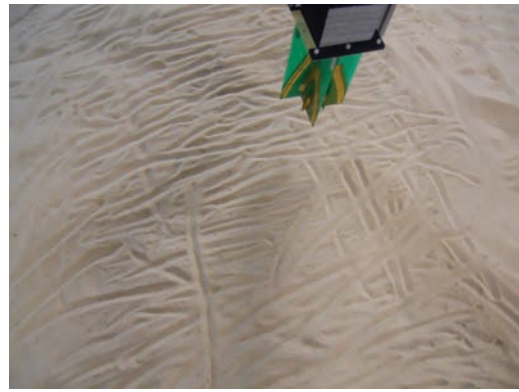
(a) Photo 1



(b) Photo 2



(c) Photo 3



(d) Photo 4

Figure 73: Four photographs of the sand surface in the first surface roughness experiment.

Co-polarization and cross-polarization center-lane responses are shown in Figure 74. The wire target still has almost equal co-polarization and cross-polarization responses. The ground surface has a high cross-polarized response and a low co-polarized response. The surface roughness may have introduced a little bit more co-polarization into the ground-surface response.

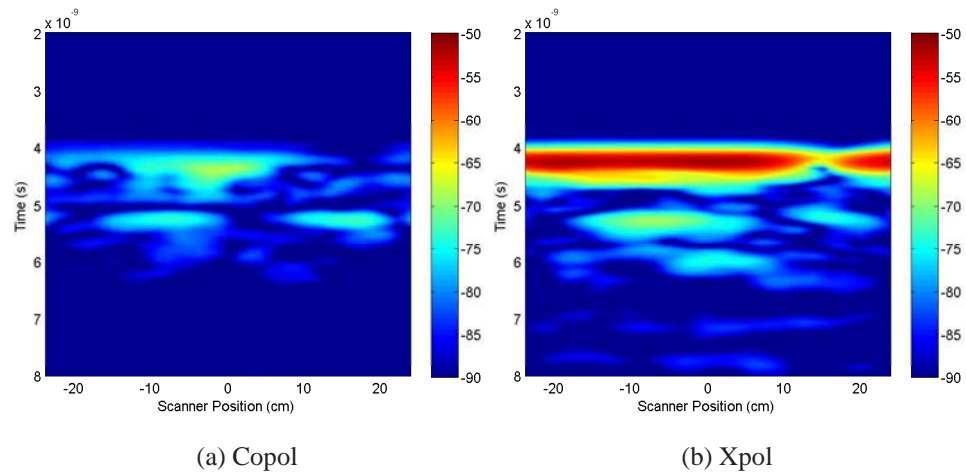


Figure 74: Co-polarization and cross-polarization responses from the first surface roughness experiment. The wire target is aligned with the scanning lane.

False color maps for the first experiment are shown in Figure 75. The wire remains plainly visible while underneath the rough sand surface. The response from the ground surface appears as a linear target in a couple of areas, but the ground surface remains mostly a radially symmetric target.

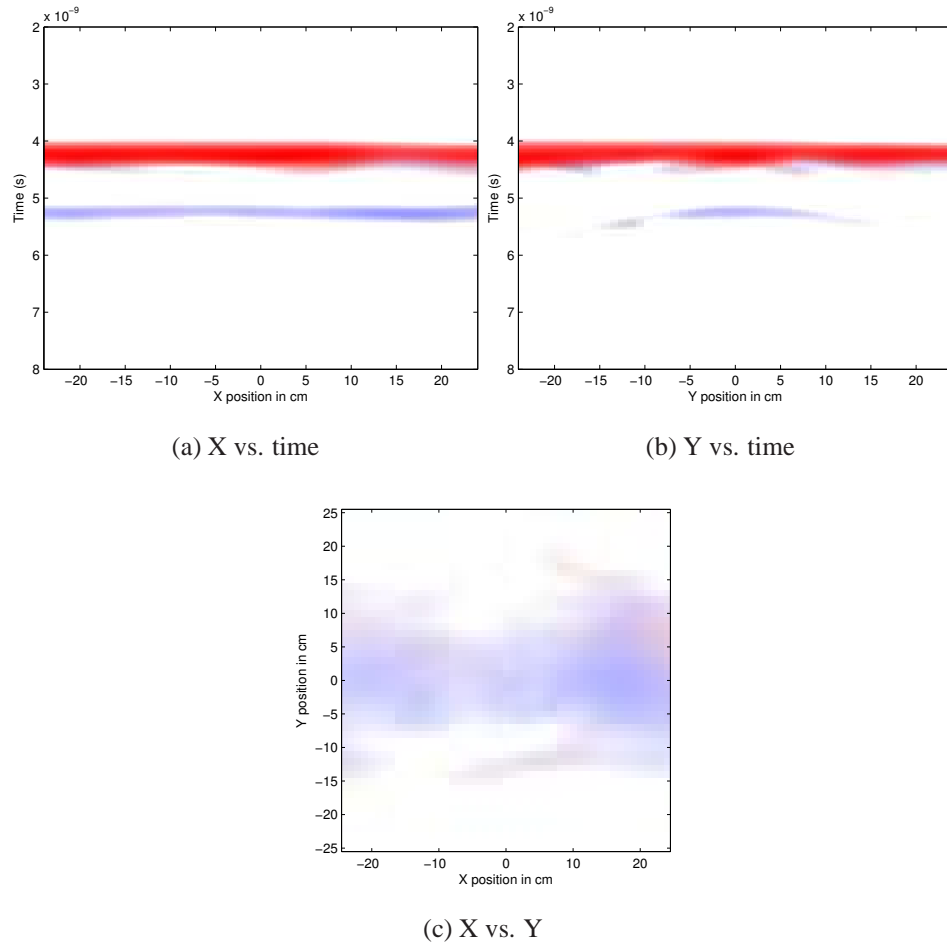
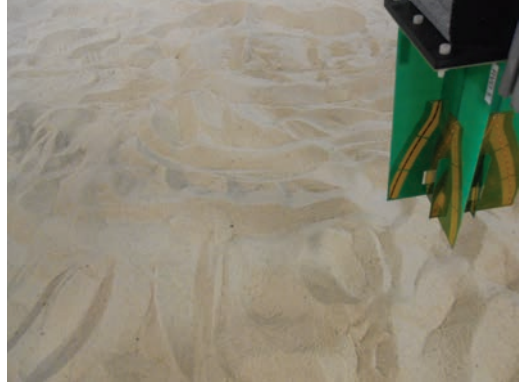


Figure 75: False color maps of the first surface roughness experiment. The wire target runs across the width of the scanning area in the X-direction at approximately  $Y = 0$  cm.

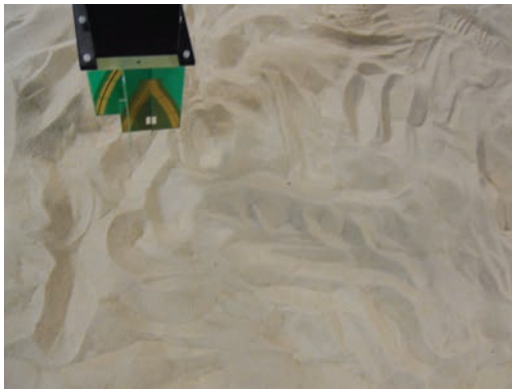
For the second experiment, large valleys and hills were formed into the surface of the sand. Photographs of the sand surface are shown in Figure 76.



(a) Photo 1



(b) Photo 2



(c) Photo 3



(d) Photo 4

Figure 76: Four photographs of the sand surface in the second surface roughness experiment.

The wire target remained buried in the same position as in the first experiment. Co-polarization and cross-polarization center-lane responses are shown in Figure 77. The ground response has even more co-polarization in this experiment, making the wire target more difficult to distinguish from the ground surface.

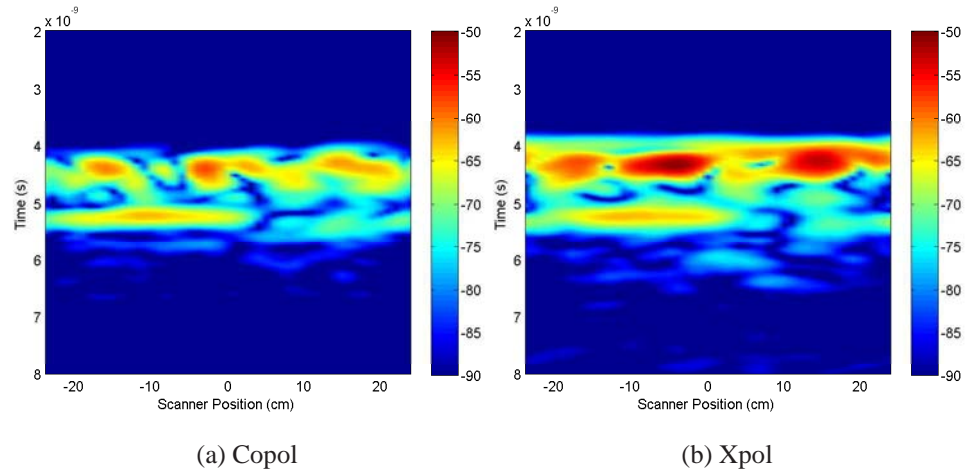


Figure 77: Co-polarization and cross-polarization responses from the second surface roughness experiment. The wire target is aligned with the scanning lane.

False color maps for the second experiment are shown in Figure 78. The wire remains plainly visible while underneath the rough sand surface. The response from the wire target appears to vary with the large changes in target depth. The response from the ground surface varies greatly. In places the ground surface appears as a linear target, and in other places the ground surface appears as a radially symmetric target. It is difficult to provide a geometry classification for the rough sand surface.

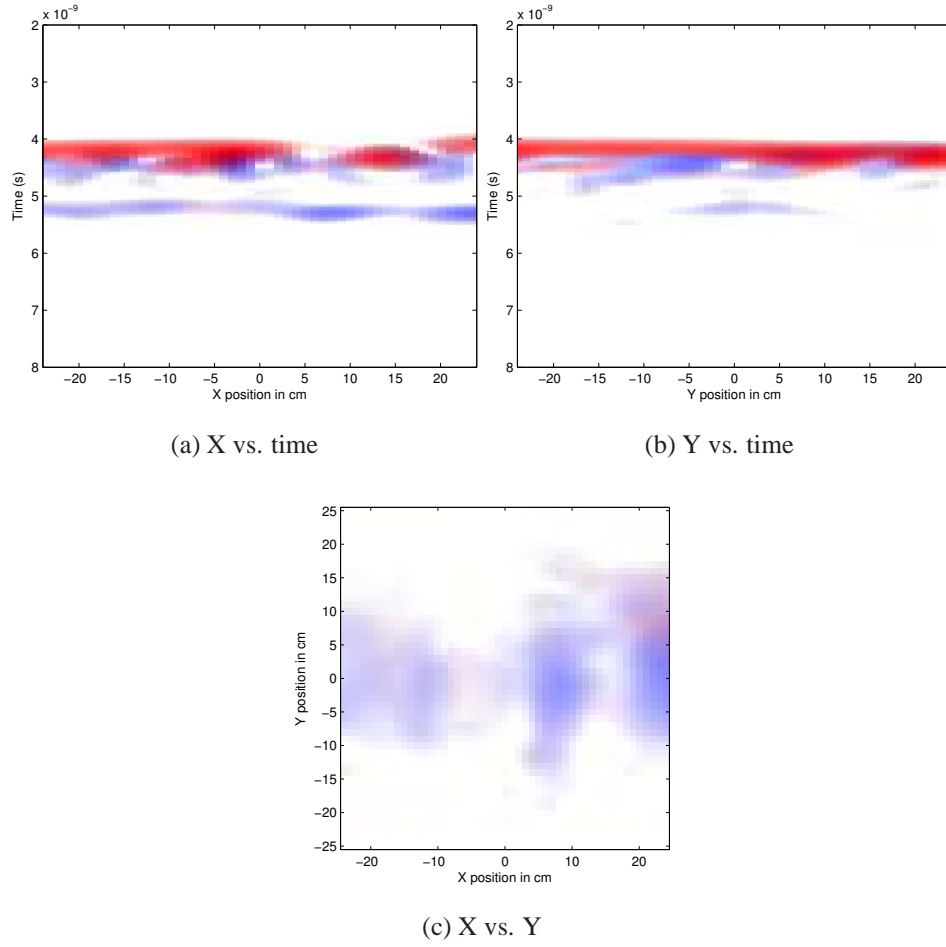


Figure 78: False color maps of the second surface roughness experiment. The wire target runs across the width of the scanning area in the X-direction at approximately  $Y = 0 \text{ cm}$ .

Pseudocolor graphs for  $S_{21}$  and  $S_{43}$  in the time-domain are shown in Figure 79. Antennas 2 and 1 are parallel and aligned with the buried wire. Antennas 4 and 3 are parallel and orthogonal to antennas 2 and 1. Figure 79 demonstrates the advantages of the RVD-based CP antenna over a traditional linear polarization GPR system. For  $S_{21}$  the response of the buried wire is visible, but the buried wire response looks similar to the response from the surface of the ground. From just looking at  $S_{21}$ , it is difficult to determine if the response of the wire is actually caused by a buried wire, or some interface between layers of different soil. For a Y-direction scan of  $S_{21}$ , the wire response would look quite similar to the



response of a loop. From just looking at  $S_{43}$ , the buried wire is not visible at all. With the RVD-based CP antenna, the wire target may be quickly identified.

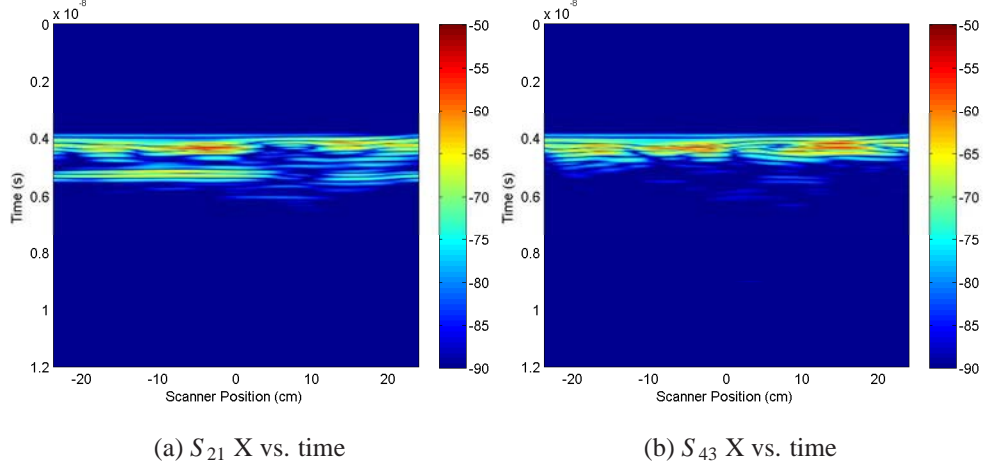


Figure 79: S-parameter measurements of the second surface roughness experiment.

The RVD-based CP antenna performs well in the surface-roughness experiments. The roughness in the sand surface greatly affects the response. The buried wire targets are still easily detected and identified.

## CHAPTER 4

### RVD IMPROVEMENT FOR OFF-BORESIGHT CP

In the previous chapters, a set of four RVD antennas designed by Kim were combined to make a dual-polarized antenna. The Kim RVD antenna was designed to be used for a linearly polarized GPR system. The resulting dual-polarized antenna was shown to be effective for targets centered under the antenna, but its effectiveness degraded when the targets were not centered. In this chapter the RVD is redesigned to perform better in the dual-polarized antenna.

The goal of the RVD redesign is to increase the area over which the RVD-based CP antenna is capable of transmitting and receiving circular polarization. In Figure 26 the loop target only appears like a radially symmetric target when it is positioned at boresight. This problem is due to asymmetry in the radiation pattern of the RVD. The synthesization of circular polarization assumes that orthogonal RVDs radiate electric fields everywhere that are equal in magnitude and orthogonal in direction of polarization. However, this assumption can be false when electric fields that are away from boresight are examined. The RVD redesign should help the antenna correctly categorize targets that are a little bit farther away from boresight. Two features of the RVD are examined for improving the CP synthesis, the curvature of the RVD arms, and the resistive profile along the RVD arms.

Two optimizations of the RVD are presented in this chapter. In the first optimization, the shape of the RVD changes while the resistive profile remains the same. This optimization improved the CP synthesis of the RVD-based CP antenna, but the RVDs lost some gain. In the second optimization of the RVD, the arm shape and the resistive profile were simultaneously changed to allow for further improvement.

## 4.1 RVD Reshaping

The curvature of the RVD arms was previously developed by Kim [37]. A diagram of the RVD geometry is shown in Figure 80.

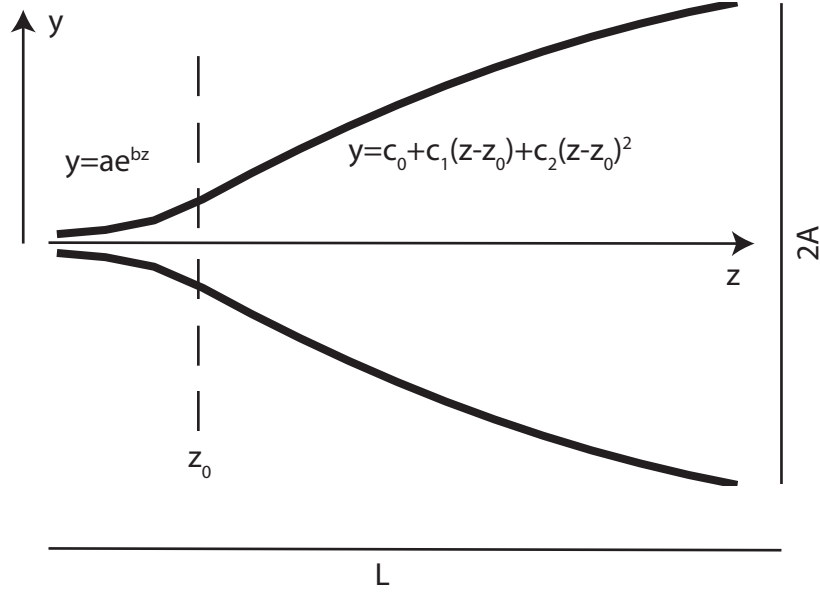


Figure 80: A diagram showing the parameters that define the geometry of the RVD.

The shape of the RVD arm is an exponential function that transitions into a quadratic function. The length of the RVD is defined by  $L$ , and the width between the ends of the arms is defined by  $2A$ . The first portion of the arm is characterized by

$$y = ae^{bz}, \quad (24)$$

where  $a$  and  $b$  can be adjusted to change the shape of the exponential. The point at which the exponential becomes the quadratic is  $z_0$ . The second portion of the arm is characterized by

$$y = c_0 + c_1(z - z_0) + c_2(z - z_0)^2, \quad (25)$$

where  $c_0$ ,  $c_1$ , and  $c_2$  are parameters that determine that shape of the quadratic. There are some restrictions on  $a$ ,  $b$ ,  $c_0$ ,  $c_1$ , and  $c_2$ . First,  $a$  is the width at the terminal end of the RVD

and should be set to the desired width. Second, in order to ensure the two portions of the arm are connected, the piecewise function must be continuous. Therefore,

$$ae^{bz_0} = c_0. \quad (26)$$

Next, the arms should be continuously differentiable at  $z_0$ . Therefore,

$$abe^{bz_0} = c_1. \quad (27)$$

Finally, the width at the arm ends is

$$A = c_0 + c_1(L - z_0) + c_2(L - z_0)^2. \quad (28)$$

In Kim's work the following parameters were selected:  $L = 0.01715 \text{ m}$ ,  $2A = 0.01143 \text{ m}$ ,  $z_0 = 0.2L$ ,  $a = 7.919 \cdot 10^{-4} \text{ m}$ ,  $b = 67.34 \text{ m}^{-1}$ ,  $c_0 = 7.976 \cdot 10^{-3} \text{ m}$ ,  $c_1 = 0.5371$ , and  $c_2 = -1.302 \text{ m}^{-1}$ .

For reshaping the RVD,  $a$  and  $b$  were left unchanged,  $z_0$  and  $c_2$  were varied, and  $c_0$  and  $c_1$  were determined by the restrictions. The width of the feed is determined by  $a$ , so  $a$  was not changed to avoid redesigning the feed. Also,  $b$  was left unchanged because  $z_0$  and  $c_2$  seem to have a greater effect on the arm shape, and changing  $b$  as well would complicate the optimization. At this point it is necessary to develop a metric that evaluates how well an RVD produces circular polarization. For a Y-direction polarized RVD, the  $E_y$  near fields were computed on a plane 10 cm in front of the RVD. The near fields were compared moving in the X-direction away from boresight and moving in the Y-direction away from boresight. The goal is to have the same distribution the near fields in both directions. In this way an X-direction polarized RVD would have nearly the same near fields everywhere. Together, the X-direction polarized RVD and the Y-direction polarized RVD would synthesize better CP away from boresight, because CP requires orthogonal field components of equal magnitude.

The metric is given by

$$M = \sum_i |E_{ypp}(x_i, 0) - E_{ypp}(0, x_i)|, 0 \text{ cm} \leq x_i \leq 25 \text{ cm}. \quad (29)$$

To compute this metric, the  $E_y$  near fields along  $x = 0$  and  $y = 0$  are collected and viewed in the time-domain. At each point the peak-to-peak amplitude of the signal is computed. For each pair of points that are the same distance from the center, the peak-to-peak amplitudes are subtracted. For example, a point 5 cm in the X-direction would be paired with a point 5 cm in the Y-direction. Then the absolute value of each pair is taken, and the metric is defined as the sum of all of the absolute values. A metric value of zero would indicate that each pair of points has the same peak-to-peak amplitude. Then the metric is minimized over  $z_0$  and  $c_2$ , with  $z_0$  between  $0.01L$  and  $0.3L$ , and  $c_2$  between  $-2$  and  $0$ .

The RVDs were modeled in NEC2d for many different values of  $z_0$  and  $c_2$ . Initial attempts at optimization resulted in selections with very wide antennas with  $2A$  greater than 1 m. Such a large antenna would be expected to have consistent field values over a large area, but it would not be practical due to its size. The constraint was used to fix the width.  $z_0$  was varied, while  $c_2$  was chosen to keep  $2A$  fixed. The constraint allowed for  $b$  to be introduced as an optimization parameter in place of  $c_2$ .

The selection with the lowest metric value has  $z_0 = 0.01L$ ,  $b = 4$ , and  $c_2 = -0.0464 m^{-1}$ . With  $z_0$  so small,  $b$  does not greatly affect the shape of the RVD arms. This selection has a metric value of 1.3781 compared to a value of 2.6421 for the previous RVD. A picture of the resulting RVD shape is shown in Figure 81. Contours comparing the near field values for the Kim RVD and the reshaped RVD are shown in Figure 82.

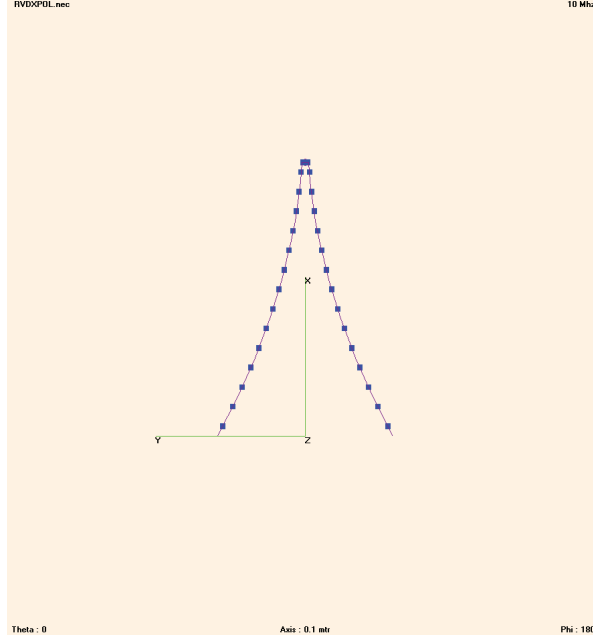


Figure 81: A diagram of the optimized RVD shape.

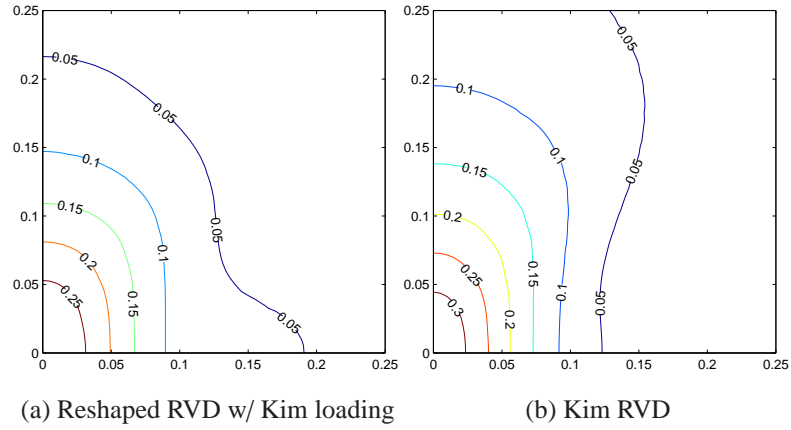


Figure 82: Near fields for the optimized and old RVDs.

The  $z_0$ -dependence of the metric is shown in Figure 83. In Figure 83 the different curves represent changing the metric by limiting the distance from boresight of the fields used to compute the metric. These changes represent changes on the limits of  $x_i$  in Equation 29. Even when the metric focuses on fields very near to boresight, low values of  $z_0$  still achieve a minimum value for the metric. This information indicates that the reshaped RVD

improves CP both near and far from boresight.

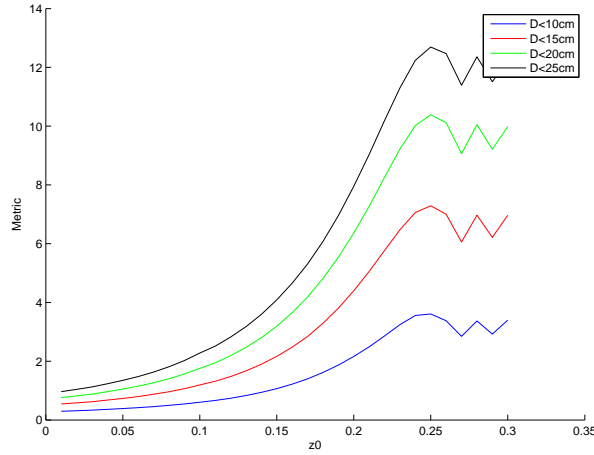


Figure 83: Metric values versus  $z_0$ . The black curve uses a metric that compares field values with 25 cm of boresight, the green curve uses a metric that compares field values with 20 cm of boresight, the red curve uses a metric that compares field values with 15 cm of boresight, and the blue curve uses a metric that compares field values with 10 cm of boresight.

NEC simulations were performed with four of reshaped RVDs in the developed configuration, scanning over the wire targets at three angles and the loop target. Center-lane results are shown in Figure 84. All of the wire targets have even co-polarized and cross-polarized responses, and they appear blue on the false color maps. The loop target has a high cross-polarized response, a low co-polarized response, and it appears blue on the false color map. The reshaped RVD is just as capable at detecting the targets as the previous RVD was in Figure 24.

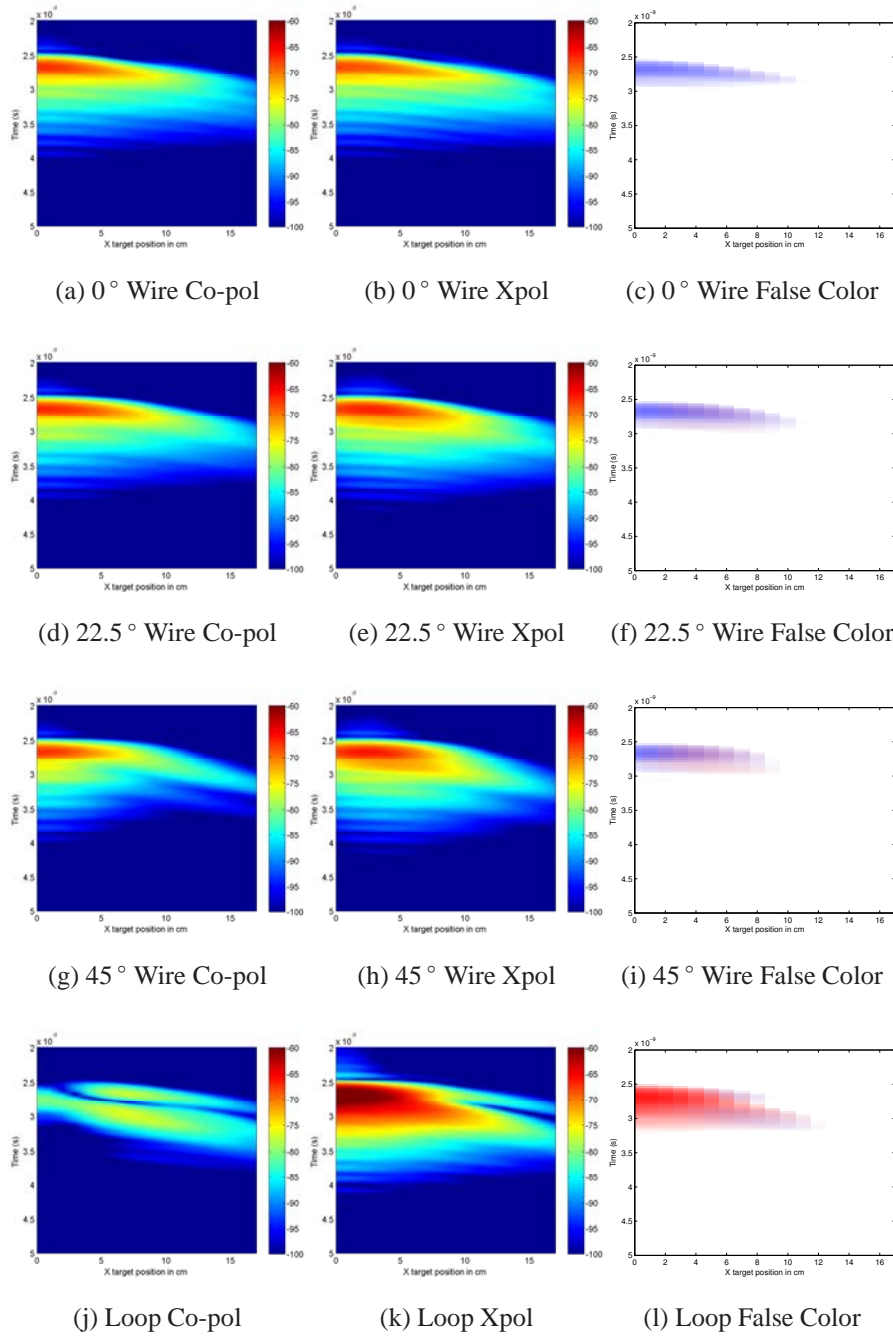


Figure 84: Numerical results for reshaped RVD scans of wire targets a loop target. The left-most column figures are the co-polarized signals in dB. The center column figures are the cross-polarized signals in dB. The right-most column figures are the false color mapped signals.



Top-down false color maps are shown in Figure 85. The loop target in Figure 85d appears red with very small blueness at the edges. The loop in Figure 85d appears red over a larger area than the loop in Figure 26d. The reshaped RVD demonstrates improved performance over the previous design.

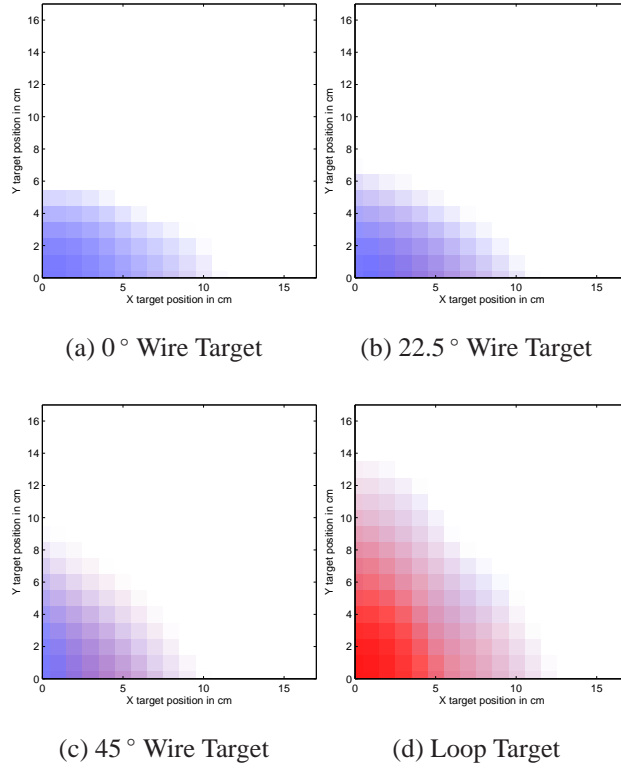


Figure 85: False color maps for the reshaped RVD scans of wire and loop targets.

## 4.2 Resistive Profile Analysis

An analysis was performed to attempt to further improve the RVD by changing the parameters of the resistive profile and the shape parameters of the RVD simultaneously. The goal is to improve the quality of the off-boresight CP. The improvements are meant to make it easier to distinguish between linear targets and radially symmetric targets.

For this optimization of the RVD, four parameters were varied. These parameters come from the design of the original Kim RVD [37]. The first two parameters are  $R_1$  and  $R_2$ , which determine the resistive profile on the RVD. The resistance values along the RVD

arms are given by

$$R(r') = \frac{\Delta h(r')}{\frac{\left(1 - \frac{r'}{h}\right)}{\frac{R_1}{h}} + \frac{\left(1 - \frac{r'}{h}\right)^2}{\frac{R_2}{h}}}, \quad (30)$$

where  $r'$  is the position along the RVD arm,  $h$  is the total length of the RVD arm, and  $\Delta h(r')$  is the length of the arm segment corresponding to the resistor at  $r'$ .

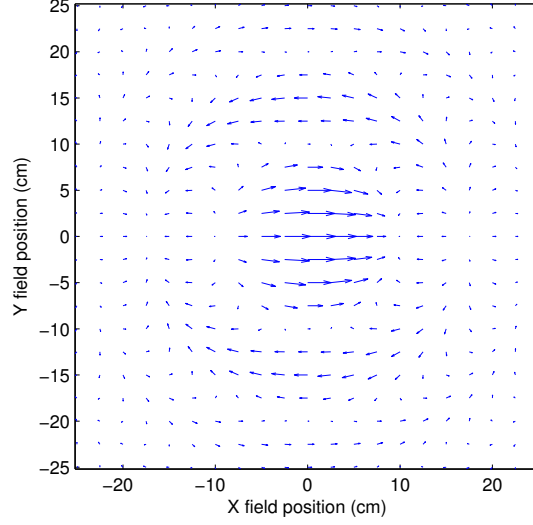
The shape of the RVD was also varied in the optimization. The shape of the RVD arm is characterized by

$$y = \begin{cases} ae^{bz} & \text{if } z < z_0, \\ c_0 + c_1(z - z_0) + c_2(z - z_0)^2 & \text{if } z > z_0. \end{cases}$$

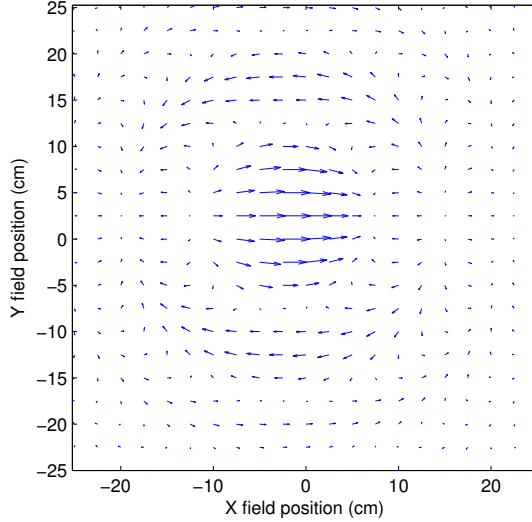
The parameters  $b$  and  $z_0$  were selected to be varied in the optimization.  $a$  is determined by the separation width at the RVD feed.  $c_0$  and  $c_1$  are determined by forcing the RVD shape to be continuous with a continuous derivative at  $z_0$ .  $c_2$  is determined by forcing the separation between the ends of the RVD arms to be 11.43 cm.

The parameters  $R_1$  and  $R_2$  were each varied between 50 and 500  $\Omega$ . The parameter  $z_0$  was varied between  $0.04L$  and  $0.96L$ , where  $L$  is the length of the RVD. The parameter  $b$  was varied between 25 and 65. RVDs that were wider than 11.43 cm at any point were left out of the optimization.

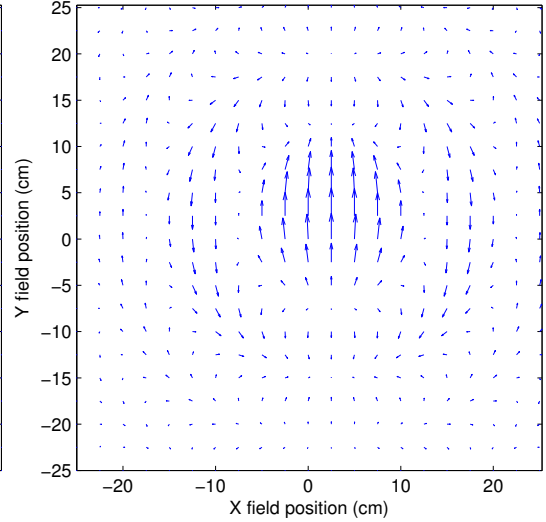
For the optimization a single RVD of each parameter set was simulated with NEC, and the near fields were computed. Using the field pattern of that single RVD, the near field patterns for each of the four RVDs in the CP antenna were computed by translating and rotating the original field pattern. Example vector maps for the original and some transformed near fields are shown in Figure 86. This method eliminates the need to simulate all four RVDs and hastens the computation.



(a) Original Near Field



(b) RVD 2 Near Field



(c) RVD 3 Near Field

Figure 86: Vector maps of the near field patterns based on the original Kim RVD.

With all four near-field patterns, reciprocity is used to compute the RVD responses of small, symmetric scatterers at each field point [34]. This step further speeds up the computation by avoiding having to simulate targets in NEC. From reciprocity the antenna response on antenna 2 from transmitting on antenna 1 is given by

$$V_{21} = -\frac{j\omega Z_c (\epsilon E_2^T P_e E_1)}{2V_2}, \quad (31)$$

where  $Z_c$  is the input impedance,  $\epsilon$  is the permittivity,  $E_2$  and  $E_1$  are the near fields produced by antennas 2 and 1 respectively at the scatterer location,  $V_2$  is the source voltage of antenna 2, and  $P_e$  is the polarizability matrix for the small, symmetric scatterer. The polarizability of a symmetric scatterer is used in the optimization of the antennas since it is good test for the cross-polarization quality and co-polarization quality of the antenna. The polarizability matrix of a symmetric scatterer is proportional to the identity matrix.  $S_{21}$  can be computed within some unknown scale factor with

$$S_{21} \propto -j\omega (\epsilon E_2 I E_1). \quad (32)$$

The S-parameters  $S_{23}$ ,  $S_{41}$ , and  $S_{43}$  can be computed in a similar manner. Then the co-polarization and cross-polarization responses may be computed using Equation 15 and Equation 16.

At this point it is necessary to develop metrics to compare the performance of all of the simulated RVDs. The first metric is meant to represent the boresight signal strength of an RVD. Using the cross-polarization S-parameter, the time-domain response at boresight is computed for a differentiated Gaussian pulse with a center frequency of 2.5 GHz. The difference between the maximum and minimum values for the cross-polarization time-domain response is used for the signal strength metric,  $X_0$ .  $X_0$  may be calculated with

$$X_0 = \max_t X_b(t) - \min_t X_b(t), \quad (33)$$

where  $X_b(t)$  is the boresight cross-polarization time-domain response.

The next metric is meant to assign a single value to the ability of each RVD to distinguish between radially symmetric targets and linear targets. This metric is based on the ratio of co-polarization to cross-polarization. Since the optimization is meant to increase the area over which a radially symmetric target has a low co-polarization to cross-polarization ratio, it is necessary to examine the near fields off of boresight. First, the co-polarization and cross-polarization time-domain peak-to-peak values are computed at each near field

point. The co-polarization to cross-polarization ratio metric,  $M$ , is given by

$$M = \max_{|\vec{r}| < 7.5 \text{ cm}} \left( \frac{C_{pp}(\vec{r})}{X_{pp}(\vec{r})} \right). \quad (34)$$

The near fields considered for  $M$  are restricted to be within 7.5 cm of boresight. The distance 7.5 cm was chosen to focus the optimization on a large area, without putting too much weight on improving the responses where the target is faintly detected. A good candidate RVD should have a low value for  $M$  because  $M$  acts like an upper bound on the co-polarization to cross-polarization ratio over a certain area.

The third metric captures the time-compactness of the transmitted pulses from the RVD. As with  $X_0$ , this metric makes use of the boresight cross-polarization time-domain response,  $X_b(t)$ . The metric is obtained by taking dividing  $X_b(t)$  by its  $L^2$  norm, then taking the  $L^1$  norm of the result. The time-compactness metric,  $T_c$  can be calculated with

$$T_c = \frac{\int_0^T |X_b(t)| dt}{\int_0^T X_b^2(t) dt}. \quad (35)$$

An RVD with a higher value for  $T_c$  produces pulses that are less compact in time. To demonstrate how  $T_c$  correlates to time compactness, it may help to consider the two rectangular pulses that are shown in Figure 87.

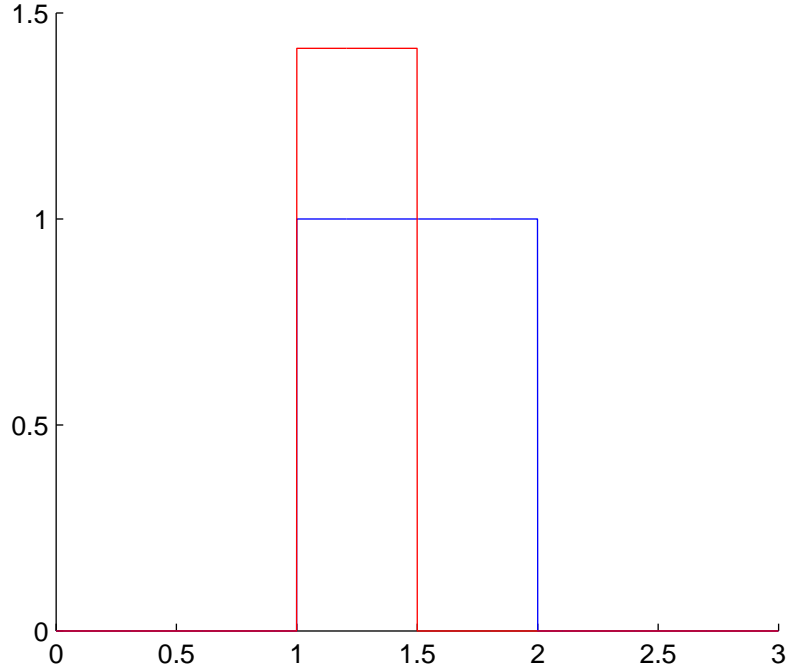


Figure 87: Example rectangular pulses. The blue pulse has a width of 1 and a height of 1. The red pulse has a width of  $\frac{1}{2}$  and a height of  $\sqrt{2}$ .

The first pulse has a width of 1 and a height of 1. The second pulse has a width of  $\frac{1}{2}$  and a height of  $\sqrt{2}$ . The second pulse is more compact in time because it has less width. A signal that is compact in time should concentrate most of its energy in a narrow time interval. Both pulses have  $L^2$  norms that are equal to one. Since the  $L^2$  norms are one,  $T_c$  is simply equal to the  $L^1$  norm in this example. For the first pulse,  $T_c = 1$ , and for the second pulse,  $T_c = \frac{\sqrt{2}}{2}$ . Therefore,  $T_c$  is a reasonable metric for time compactness, with signals that have lower values for  $T_c$  being more compact in time.

For the original Kim RVD,  $X_0 = 0.0037$ ,  $M = 0.871$ , and  $T_c = 13,536$ . Metric values for candidate RVDs are shown in Figure 88. RVDs with  $X_0 < 0.0037$  have been omitted from the scatter plot to avoid RVDs with weaker signal strength than the Kim RVD. The RVD with the lowest value for  $M$  on Figure 88 was selected for additional analysis. From the selection process, this RVD should have an  $X_0$  value at least as good as the Kim RVD, it should have a better value for  $M$  than the Kim RVD, but it may have lost some pulse time

compactness. For the reshaped RVD developed with the first optimization,  $X_0 = 0.0032$ ,  $M = 0.671$ , and  $T_c = 13,928$ . The reshaped RVD has an improved value for  $M$ , but it has a value for  $X_0$  that is 14% lower than the  $X_0$  value for the original Kim RVD.

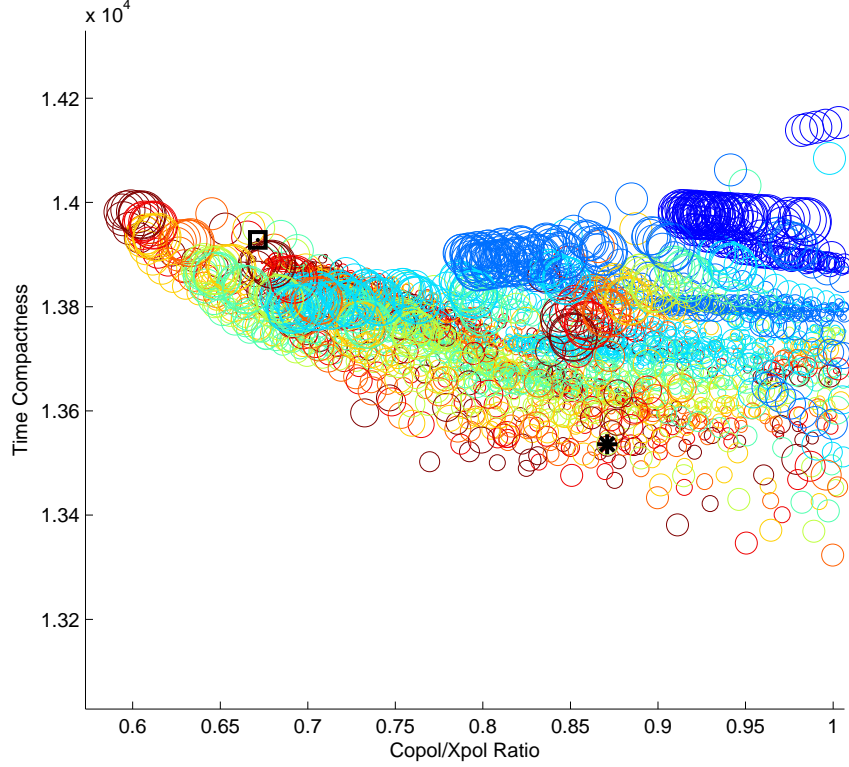


Figure 88: A scatter plot of metric values for the candidate RVDs with  $X_0 > X_{0kim} = 0.0037$ . The color of the circles on the scatter plot vary with  $R_1$ , and the size of the circles vary with  $z_0$ . The original Kim RVD is marked with the \*. The reshaped RVD with the Kim resistive profile is marked by the square.

The selected RVD has metric values of  $X_0 = 0.0038$ ,  $M = 0.594$ , and  $T_c = 13,986$ . The parameters for this RVD are  $R_1 = 500 \Omega$ ,  $R_2 = 150 \Omega$ ,  $b = 25$ , and  $z_0 = 0.69L$ . At this point the pulses for the optimized RVD and the Kim RVD should be compared to see how much time compactness was lost for the optimization. Boresight, cross-polarization, time-domain pulses are shown in Figure 89 for both RVDs. The pulses appear very similar, so there is no significant loss in time compactness as a cost of improving the co-polarization

to cross-polarization ratio.

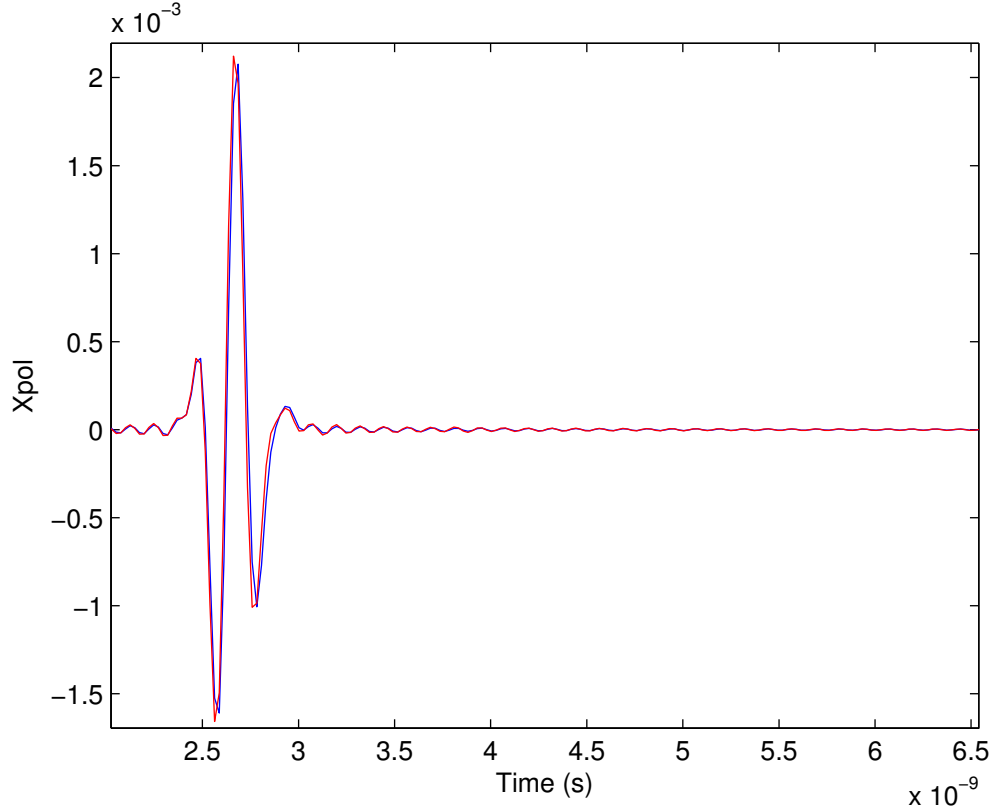


Figure 89: Time-domain pulses at boresight for the Kim RVD (blue) and the optimized RVD (red).

### 4.3 Numerical Results of Dual CP Antenna with Improved RVD

The RVD-based CP antenna with the optimized RVD was simulated with small circular loop targets in Numerical Electromagnetics Code (NEC). These simulations differ from those in Chapter 2 in one important way; the loop targets now only have a diameter of 5 mm. The targets are still in a plane 10 cm in front of the RVD-based CP antenna. The smaller loop targets should more closely match the near-field, small-scatterer, reciprocity model. The responses were modeled from 10 MHz to 8 GHz in 10 MHz increments. The pulse was chosen to be a differentiated Gaussian with a center frequency of 2.5 GHz.

Contour graphs of co-polarization and cross-polarization are shown in Figure 90. The



cross-polarization contours are similar for both RVDs, but the cross-polarization for the optimized RVD has significantly better symmetry than the Kim RVD. The co-polarization for the Kim RVD reaches values approximately 5 dB higher than it reaches for the optimized RVD. Since these results are from loop targets, the goal is to have as little co-polarization as possible.

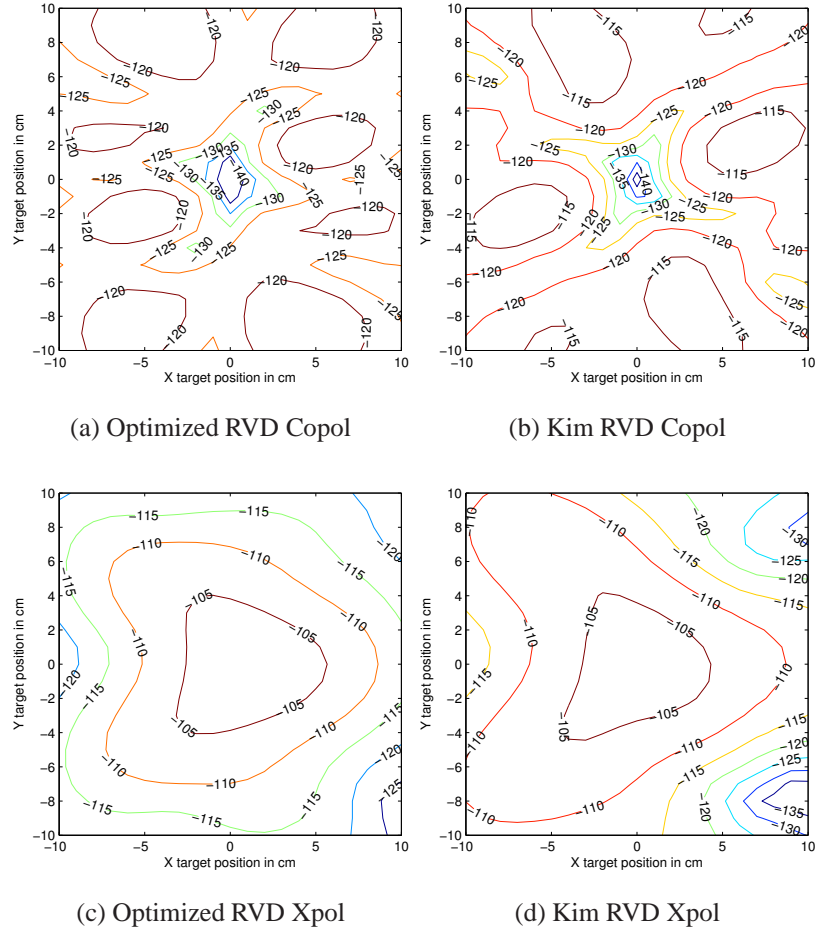


Figure 90: Co-polarization and cross-polarization contours for scans over a small loop target. Results are shown for both the Kim RVD and the optimized RVD. Contours are in dB.

Contour graphs of the co-polarization to cross-polarization ratio are shown in Figure 91. These values are generally lower for the optimized RVD, meaning that the optimized RVD is more likely to provide a correct identification of the target geometry.

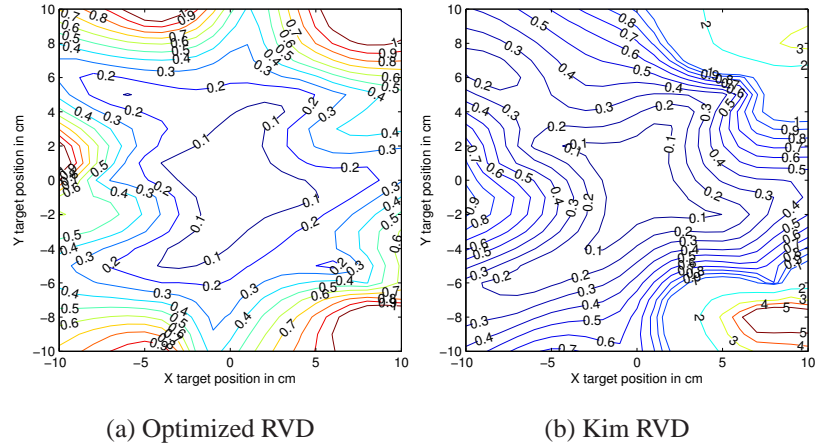


Figure 91: Co-polarization to cross-polarization ratio contours for scans over a small loop target.

False color maps of the target scans are shown in Figure 92. For the optimized RVD, the loop target appears red over most of the scanning area. The loop only appears blue within a few small areas along the boundary of the scanning area. For the Kim RVD, the loop target appears rather blue at positive- $X$  positions that are not near the center. The optimized RVD demonstrates improved reliability in geometry-based target identification.

Radiation patterns are shown in Figure 93 for both RVDs. The radiation patterns are a little bit stronger for the Kim RVD. The optimized RVD seems to have more similarity between the  $X$ - $Z$  plane radiation pattern and the  $X$ - $Y$  plane radiation pattern.

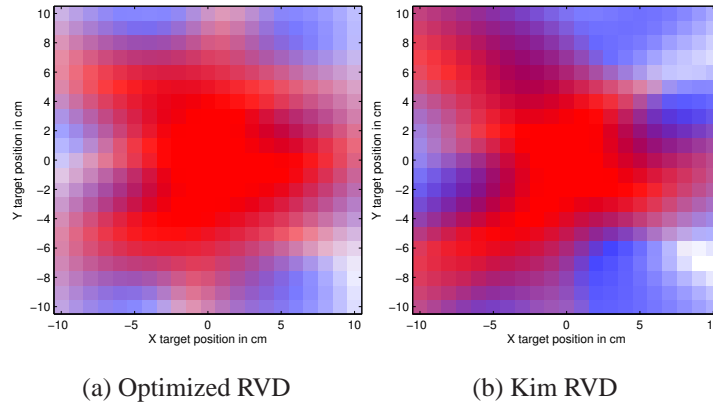


Figure 92: False color maps for scans over a small loop target. Red indicates a high co-polarization to cross-polarization ratio, and blue indicates a low co-polarization to cross-polarization ratio.

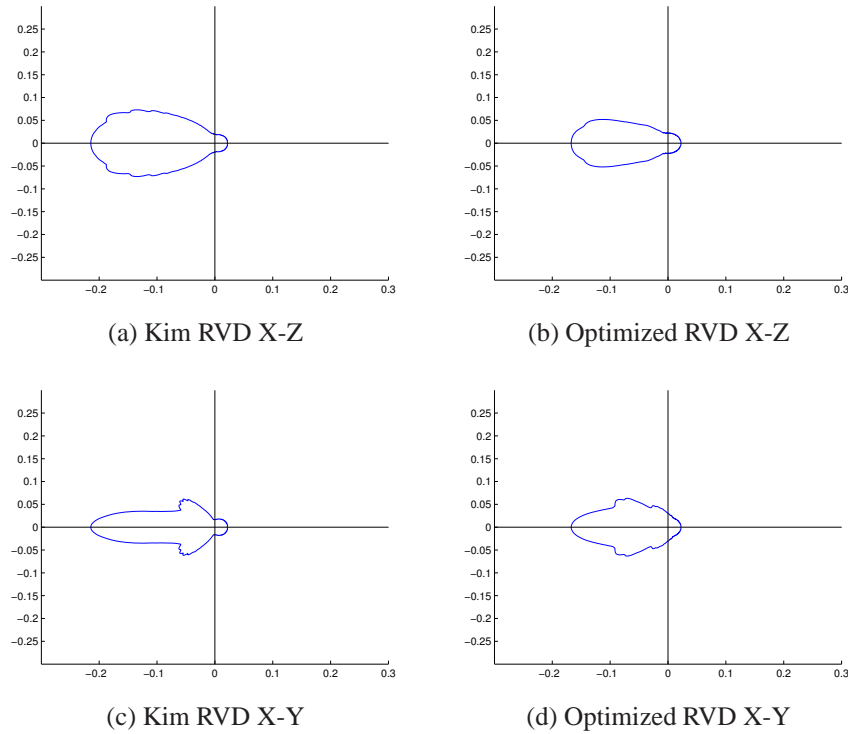


Figure 93: Radiation patterns for the optimized RVD and Kim RVD. Each RVD is directed in the negative-X direction. X-Z plane radiation patterns are in the first row. X-Y plane radiation patterns are in the second row.

#### 4.4 Experimental Results from Improved RVD

A new RVD-based CP antenna was built using the optimized RVD design of Section 4.2. It was built to reuse most of the experimental setup in Chapter 3. A photograph of the optimized RVD is shown in Figure 94. The RVD is on a 0.1 mm thick polyamide substrate. The balun is on a 1.016 mm thick FR4 PCB.

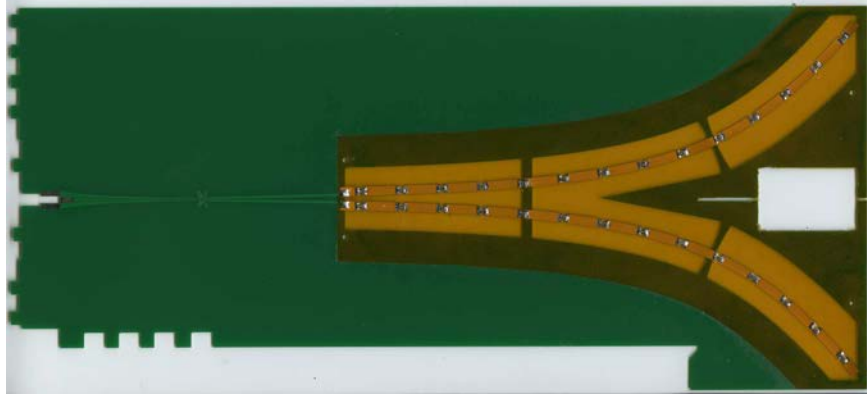


Figure 94: Photograph of the optimized RVD.

The resistive profile is approximated with 0805 surface-mount resistors. The values of these resistors for both the optimized RVD and the Kim RVD are shown in Table 1. The new RVD-based CP antenna fits onto the same positioner mount as before. A photograph of the experiment setup is shown in Figure 95.

Table 1: Resistance values (in Ohms) for resistors along the RVD arms of the optimized and Kim RVDs.

Optimized	Kim
8.06	17.8
9.09	19.6
10.2	22.1
11.8	25.5
13.7	29.4
16.2	34.0
19.6	40.2
24.0	49.9
30.9	60.4
42.2	78.7
60.4	107
102	158
210	280
866	887



Figure 95: Photograph of the optimized RVD CP antenna experimental setup.

The time-domain responses for scattering from CP antennas of each RVD type are shown in Figure 96. A differentiated Gaussian pulse with a center frequency of 2.5 GHz was used. In these experimental results, the CP antennas are detected as targets with a bistatic pair of Kim RVDs. These responses should indicate the relative radar cross-sections of each CP antenna. On each CP antenna, each RVD was connected to a  $50\ \Omega$  load. The CP antennas were placed 50 cm directly in front of the transmitting and receiving RVDs. A rectangular 21 cm by 8.5 cm metal plate was also measured as a target for reference. It was placed at a distance of 50 cm, so its response would occur at the same time as the reflection off of the front of the CP antenna. An FR4 back piece was also measured. This piece is an 18 cm by 18 cm square and is identical to the piece that holds the four RVDs together in the CP antenna. It was positioned at the spot marked by the back pieces of the CP antenna, so its response should show how much the back pieces contribute to the response of the CP antennas. The CP antennas have similar responses, so the Kim RVD and the optimized RVD should have similar radar cross-sections. In Figure 96d the response of the metal plate occurs at approximately 35.5 ns. Therefore, the responses of the CP antenna that occur at 35.5 ns are likely reflections off of the front of the antenna. The response of the FR4 back piece occurs at approximately 37.5 ns. The FR4 back piece appears to contribute to a large part of the response for each CP antenna. The optimization of the RVD appears to have maintained a low radar cross-section of the Kim RVD.

In the following sections, experimental results are presented to compare the performance of the optimized RVD and the Kim RVD.

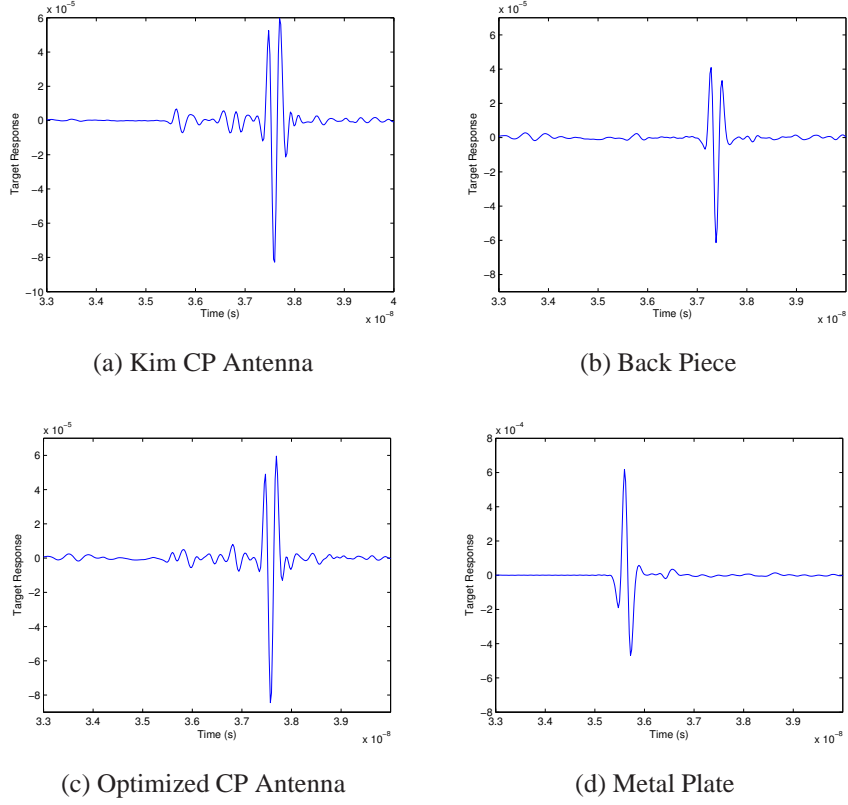


Figure 96: Time-domain responses for scattering from the the optimized RVD and Kim RVD CP antennas. A metal plate target and the CP antenna back piece are shown for reference.

#### 4.4.1 Targets in Air with Improved RVD

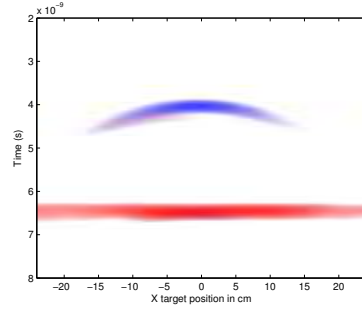
Experiments were performed on targets in air. The targets were a 20 cm long wire at angles of  $0^\circ$ ,  $22.5^\circ$ , and  $45^\circ$ , and also a 5 cm diameter loop. The targets were placed on a styrofoam pedestal. The positioner was programmed to perform scans over a 50 cm by 50 cm area. The measurements were recorded with an Agilent Technologies E5071C Network Analyzer. Measurements were made between 10 MHz and 8 GHz.

The new RVD-based CP antenna was mounted onto a positioner. 2D scans were performed with targets positioned 10 cm from the scanning plane. The targets are a 20 cm long metal wire and a 5 cm diameter metal loop. The targets were placed on top of a styrofoam pedestal, which should make the target appear almost as if it is surrounded by air

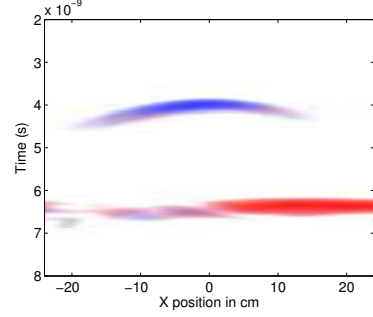
on all sides. Scans were performed over a 50 cm by 50 cm area. The results in Figure 97 represent a single scanning lane directly over the target. In these figures, the first response is from the target, and the second response is from the ground beneath the target. Since the ground is a flat surface, it should have a low co-polarization response and appear red on the false color maps. The wire targets appear very similar with the Kim RVD and the optimized RVD. However, the response from the loop target appears slightly less blue for the optimized RVD. Therefore, the optimized RVD has a lower co-polarization to cross-polarization ratio when measuring loop targets, and the optimized RVD is better for determining target geometries.

False color maps for these 2D scans are shown in Figure 98. At each measurement location the response from the ground was removed with time-gating to isolate the response of the target. Detection of the wire targets does not change much between the Kim RVD and the optimized RVD. The loop target appears slightly more red with the optimized RVD, but the response also appears slightly weaker.

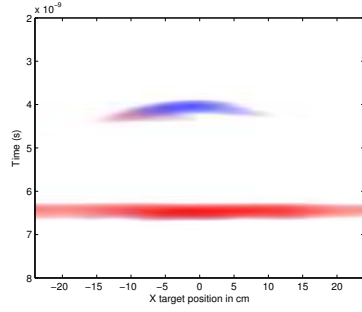




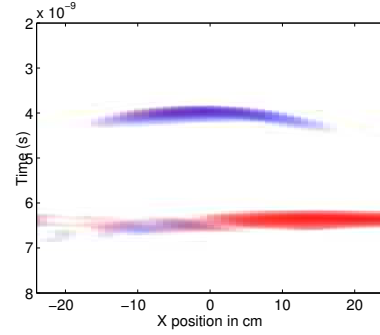
(a) 0° Wire, Optimized RVD



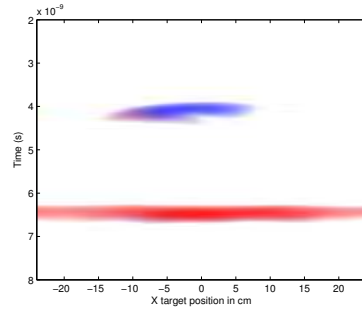
(b) 0° Wire, Kim RVD



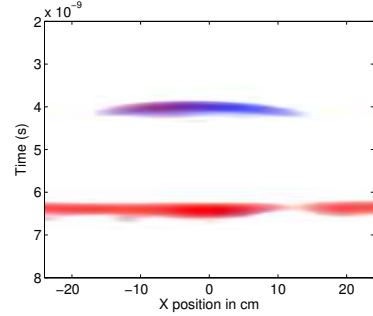
(c) 22.5° Wire, Optimized RVD



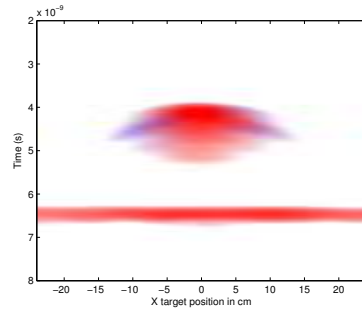
(d) 22.5° Wire, Kim RVD



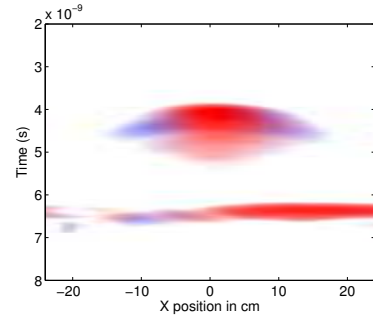
(e) 45° Wire, Optimized RVD



(f) 45° Wire, Kim RVD



(g) Loop, Optimized RVD



(h) Loop, Kim RVD

Figure 97: False Color Maps for 20 cm long wire targets at 0°, 22.5° and 45°, as well as a 5 cm diameter loop target. The targets are measured in air.

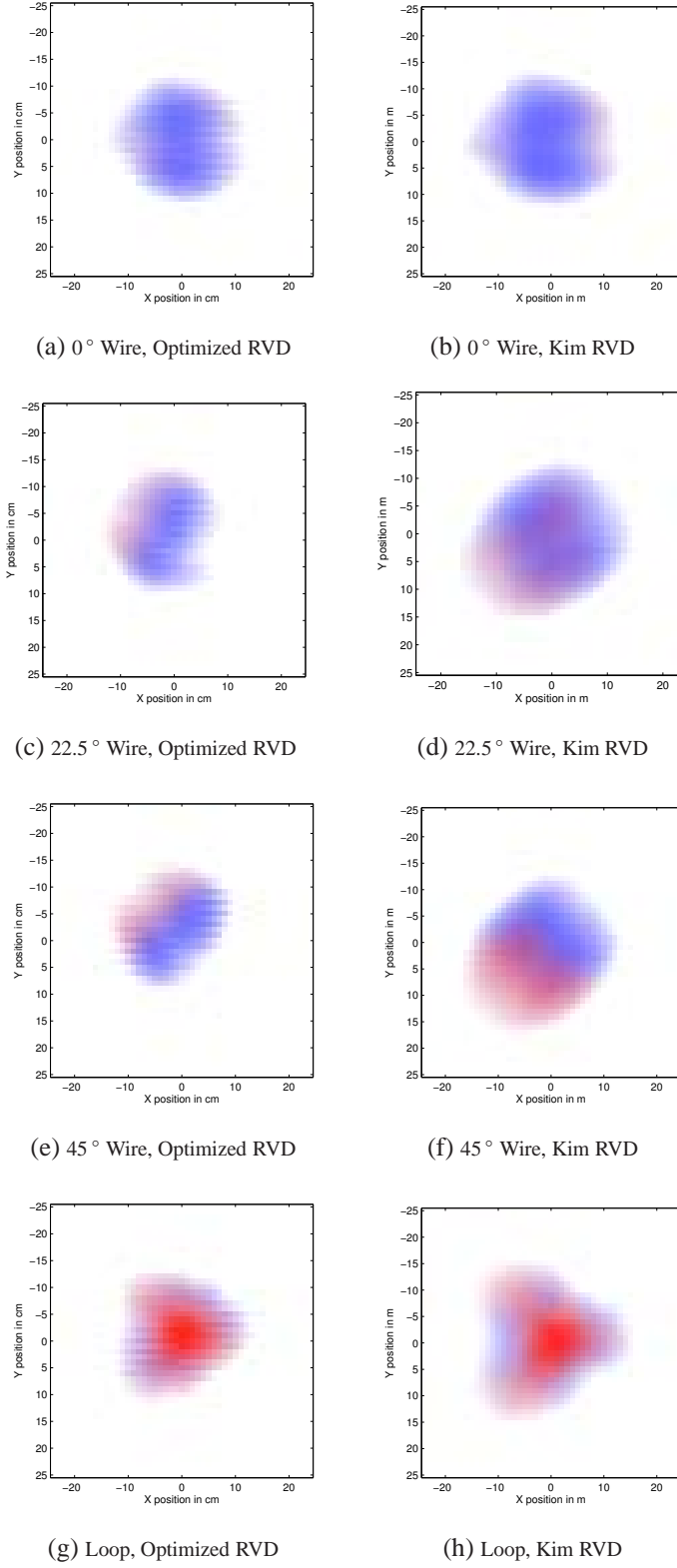
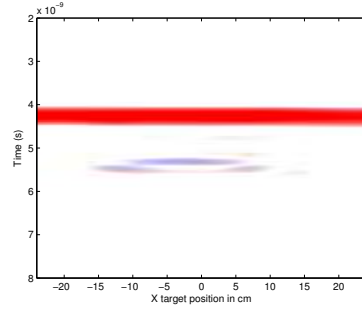


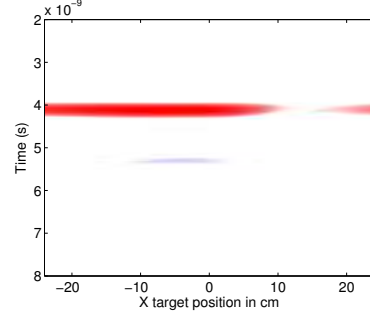
Figure 98: False color maps of experimental 2D scans indicating the detection of targets in air.

#### **4.4.2 Buried Targets with Improved RVD**

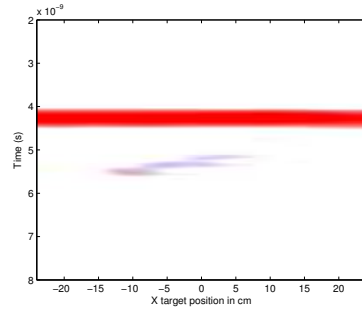
Scans were performed over buried targets. The scans were done over a 50 cm by 50 cm area. The wire and the loop were buried in smooth, leveled sand. The antenna was positioned approximately 11 cm above the ground, and the targets were buried approximately 10 cm beneath the surface. Single scanning lane results for the buried targets are shown in Figure 99. The ground response occurs at approximately 4 ns and the target response occurs at approximately 5 ns. False color maps for these 2D scans are shown in Figure 100. At each measurement location, the response from the ground was removed with time-gating to isolate the target response. The wire targets appear blue and the loop target appears red. Both RVDs appear to have similar performance for buried targets.



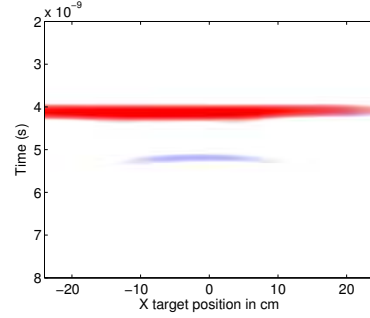
(a) 0° Wire, Optimized RVD



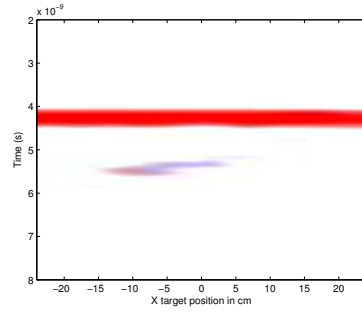
(b) 0° Wire, Kim RVD



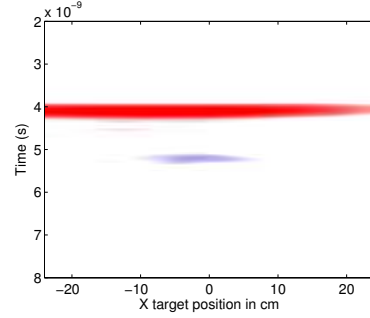
(c) 22.5° Wire, Optimized RVD



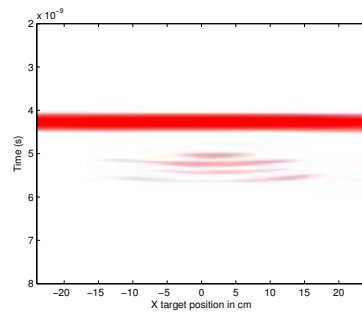
(d) 22.5° Wire, Kim RVD



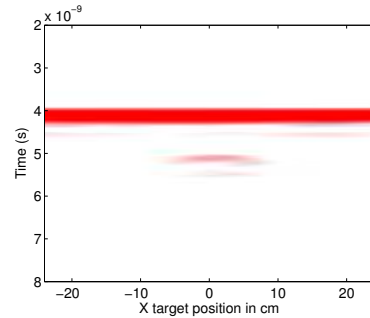
(e) 45° Wire, Optimized RVD



(f) 45° Wire, Kim RVD

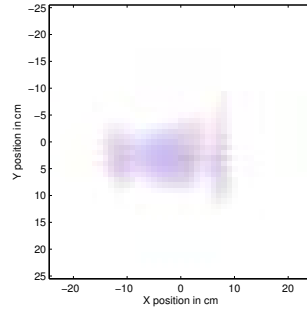


(g) Loop, Optimized RVD

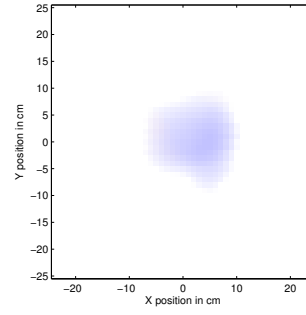


(h) Loop, Kim RVD

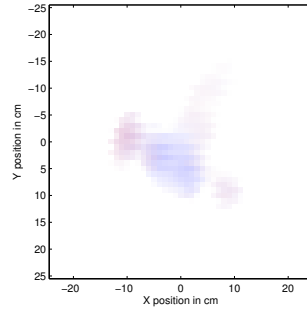
Figure 99: False color maps for 20 cm long wire targets at 0°, 22.5° and 45°, as well as a 5 cm diameter loop target. The targets were buried in the sand.



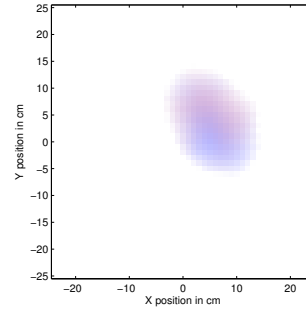
(a) 0° Wire, Optimized



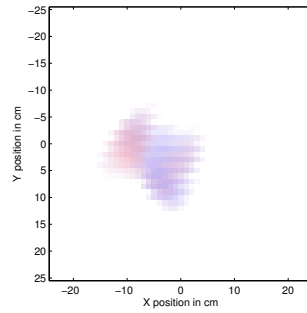
(b) 0° Wire, Kim



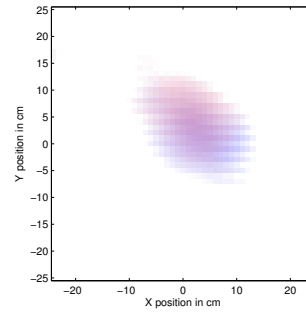
(c) 22.5° Wire, Optimized



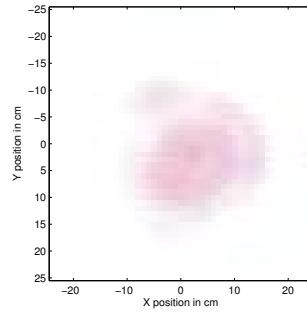
(d) 22.5° Wire, Kim



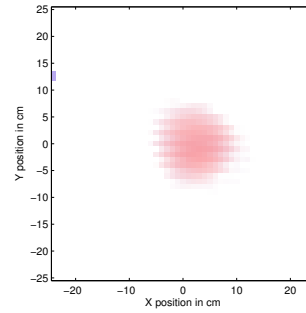
(e) 45° Wire, Optimized



(f) 45° Wire, Kim



(g) Loop, Optimized



(h) Loop, Kim

Figure 100: False color maps from buried target experiments.

## 4.5 Alternate Cross-Polarization Calculation

In this Section two alternate methods for calculating the cross-polarization S-parameter are presented. In Equation 16 the cross-polarization S-parameter is given by

$$S_{xpol} = S_{21} + S_{43} + j(S_{23} - S_{41}). \quad (36)$$

Equation 36 can be further simplified. The derivation of Equation 16 requires the assumption that the target is in the far field. In the far field, the separation distance between the four RVDs is extremely small relative to the distance between the RVDs and the target. Therefore, the separation between the RVDs can be assumed to be zero. With this assumption, RVDs 1 and 2 are colocated, and RVDs 3 and 4 are also colocated. So any measurements taken with RVD 1 would be the same if they were taken with RVD 2 instead. RVDs 3 and 4 also take interchangeable measurements. This means that

$$S_{23} = S_{14}. \quad (37)$$

As a result of reciprocity,

$$S_{23} = S_{14} = S_{41}, \quad (38)$$

because the transmitting antenna and receiving antenna can change roles without affecting the measurement. Under these new assumptions, Equation 36 becomes

$$\begin{aligned} S_{xpol2} &= S_{21} + S_{43} + j(S_{23} - S_{41}) \\ &= S_{21} + S_{43} + j(0) \\ &= S_{21} + S_{43}. \end{aligned} \quad (39)$$

The two formulations for the cross-polarization S-parameter are equivalent in the far field, but Equation 39 could have advantages over Equation 16 in the near field. In the near field, the separation between the RVDs is significant, so  $S_{23}$  ends up being slightly different from  $S_{41}$ . The same method cannot be used for computing the co-polarization S-parameter.

The optimization of the RVD is reexamined with the alternate cross-polarization. Particularly,  $M$  is recalculated for the alternate cross-polarization S-parameter. Scatter plots

of candidate RVDs are shown in Figure 101 for both methods of computing the cross-polarization. The optimized RVD with the original method of computing the cross-polarization appears among the RVDs with the lowest values of  $M$  when using the alternate method of computing the cross-polarization. The alternate method does not greatly affect the optimization of the RVD. The RVD that was selected from using the original method should also perform well with the alternate method.

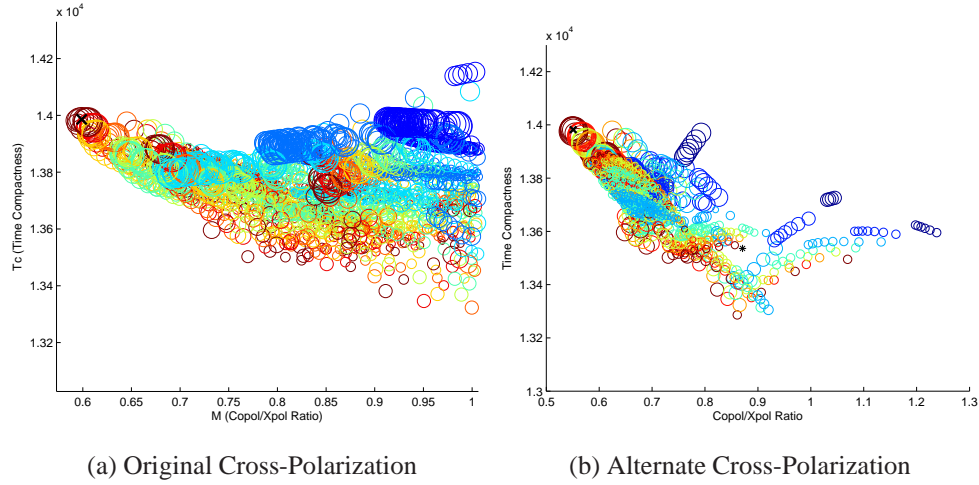


Figure 101: Scatter plot of metric values for the candidate RVDs with  $X_0 > X_{0kim} = 0.0037$ . The color of the circles on the scatter plot vary with  $R_1$ , and the size of the circles vary with  $z_0$ . In Figure 101a the original method for computing the cross-polarization is used for calculating  $M$ , and the RVD chosen with the alternate method is shown with the  $X$  marker. In Figure 101b the alternate method for computing the cross-polarization is used, and the  $X$  marks the RVD chosen with the original method.

The alternate cross-polarization calculation is applied to the numerical modeling data. The following results should provide insights into what advantages the alternate cross-polarization can provide for near-field applications.

Contour graphs of alternate cross-polarization are shown in Figure 102. The alternate cross-polarization has improved symmetry. The contours in Figure 102 appear almost circular. The improvement is noticeable on both the Kim RVD and the optimized RVD. Since

there is no analogous alternate co-polarization, the alternate co-polarization can only be compared with the original co-polarization to identify target geometries.

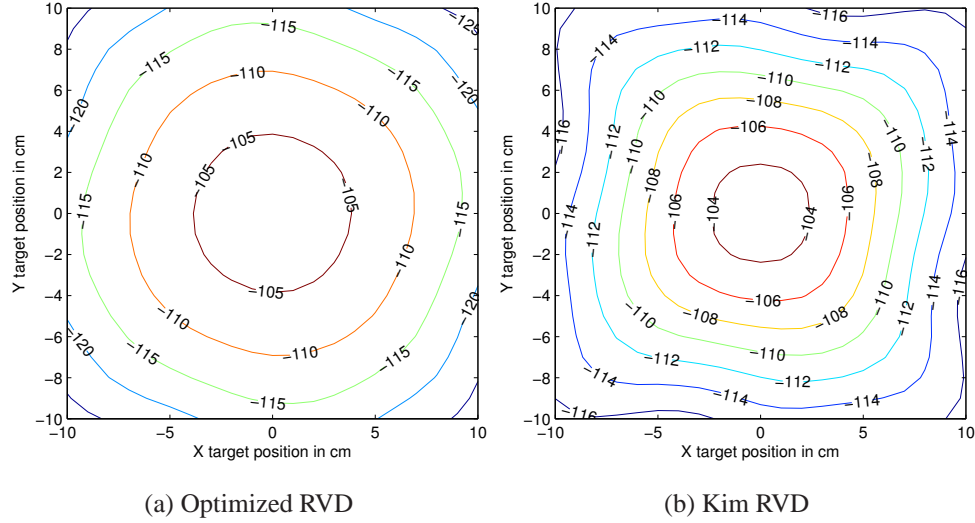


Figure 102: Alternate cross-polarization contours for scans over a small loop target. Results are shown for both the Kim RVD and the optimized RVD. Contours are in dB.

The co-polarization to cross-polarization ratios were recalculated using the alternate cross-polarization. Contour graphs of the co-polarization to alternate cross-polarization ratios are shown in Figure 103. The quadrant asymmetry does not change much for the co-polarization to cross-polarization ratios. For the optimized RVD the quadrant asymmetry seems to barely improve, and the values for the co-polarization to cross-polarization ratio appear to have slightly increased.



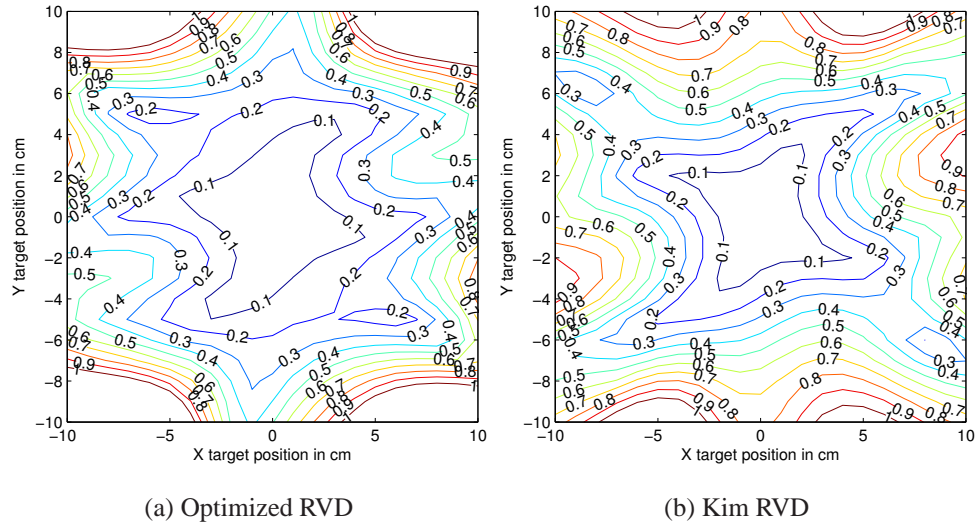


Figure 103: Co-polarization to cross-polarization ratio contours for scans over a small loop target. The alternate cross-polarization calculation was used to produce the data.

False color maps made from the alternate cross-polarization are shown in Figure 104. There appears to be barely any change for the optimized RVD. For the Kim RVD, the alternate cross-polarization improves the target identification for the positive-X values, but the Kim RVD still does not perform as well as the optimized RVD.

The alternate cross-polarization seems promising with the improved quadrant symmetry, but without lower co-polarization to cross-polarization ratios or a way to also improve the quadrant symmetry of the co-polarization near fields, it may not be too useful for the application of wire target detection and discrimination.

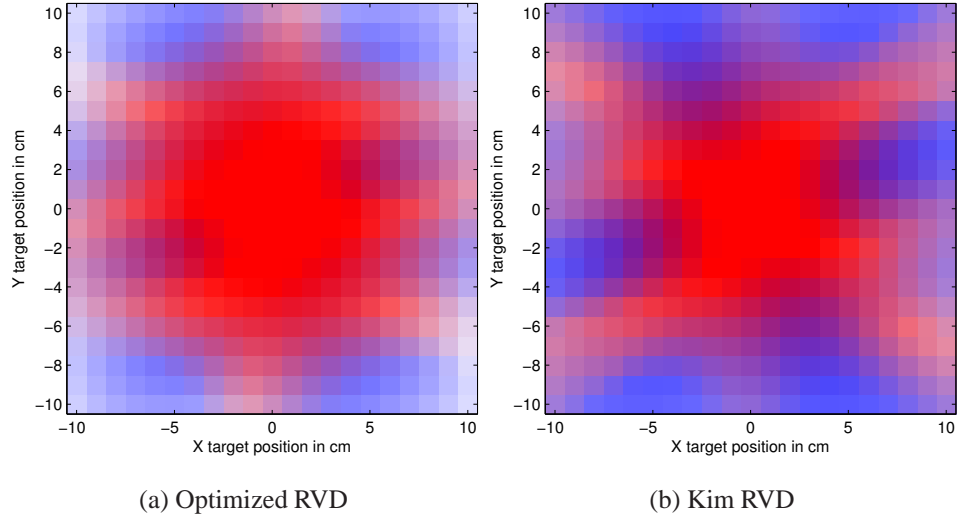


Figure 104: False color maps for scans over a small loop target. This data uses the alternate cross-polarization calculation. Red indicates a high alternate cross-polarization to co-polarization ratio, and blue indicates a low alternate cross-polarization to co-polarization ratio.

Another method for improving the computation of co-polarization and cross-polarization is developed. For this method the cross-polarization S-parameter is calculated with

$$S_{xpolavg} = S_{21} + S_{43} + j\left(\frac{S_{23}+S_{42}}{2} - \frac{S_{41}+S_{31}}{2}\right), \quad (40)$$

and the co-polarization S-parameter is calculated with

$$S_{copolavg} = S_{21} - S_{43} + j\left(\frac{S_{23}+S_{42}}{2} + \frac{S_{41}+S_{31}}{2}\right). \quad (41)$$

In the far zone,  $S_{23} = S_{42}$  and  $S_{41} = S_{31}$ . Therefore, Equations 40 and 41 are equivalent to the original method of computing co-polarization and cross-polarization shown in Equations 16 and 15. Contour graphs of the averaged co-polarization and cross-polarization responses for the small symmetric scatterer reciprocity model are shown in Figure 105. There may be some improvement in the symmetry of the cross-polarization, but Equation 39 provides even better symmetry. There is no significant improvement in the co-polarization to cross-polarization ratio. The main disadvantage of this method is that it requires the measurement of additional S-parameters.

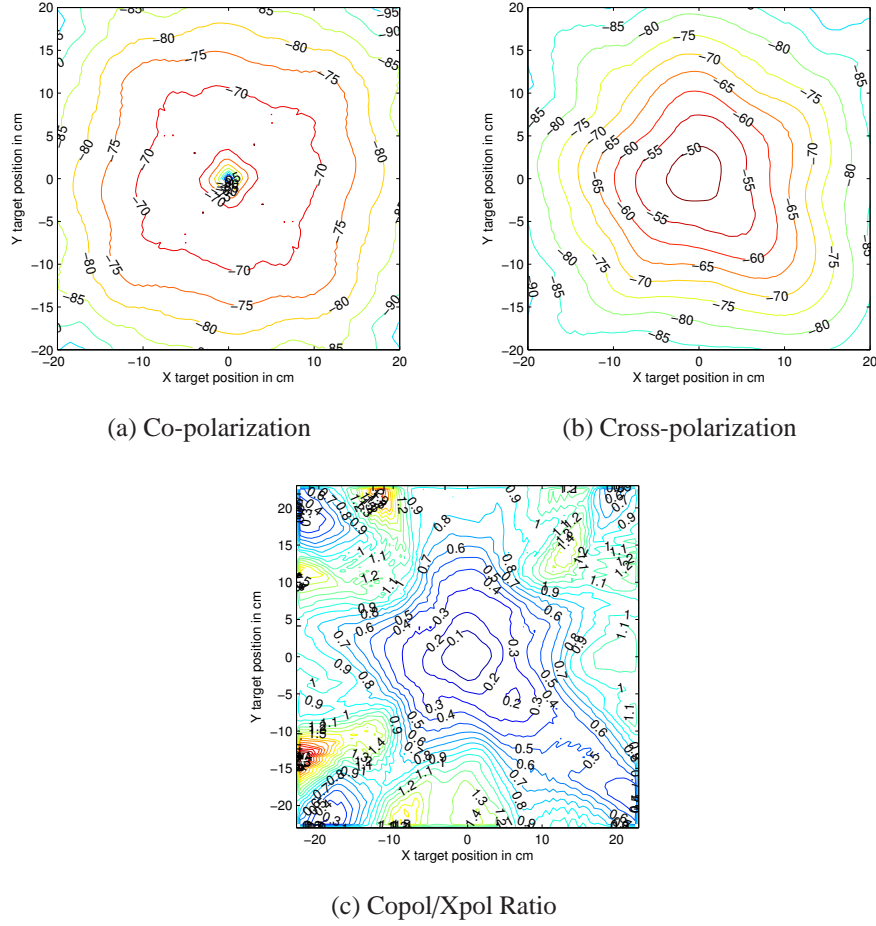


Figure 105: Contour graphs for scans over a small loop target. These results are from the reciprocity model for the optimized RVD. The averaging method for calculating the co-polarization and cross-polarization is used. The top row of figures are in dB.

The cross-polarization of Equation 39 was used with the co-polarization of Equation 41 to produce the false color maps in Figure 106. The results in Figure 106 are numerical results for the Kim RVD-based CP antenna. The target responses have improved symmetry in these false color maps compared to Figure 26. The response of the wire target varies very little when the wire target is rotated. The response of the loop target has nearly perfect radial symmetry. Equation 39 and Equation 41 appear to be better for computing cross-polarization and co-polarization than Equation 16 and Equation 15. This method requires

the measurement of two additional S-parameters, which complicates the measurement process and takes more time to perform the measurements. It is possible to transmit on one antenna and simultaneously receive on the other three, but it requires two measurements to obtain four S-parameters or three measurements to obtain six S-parameters. The original method for calculating cross-polarization and co-polarization is faster than the alternate method.

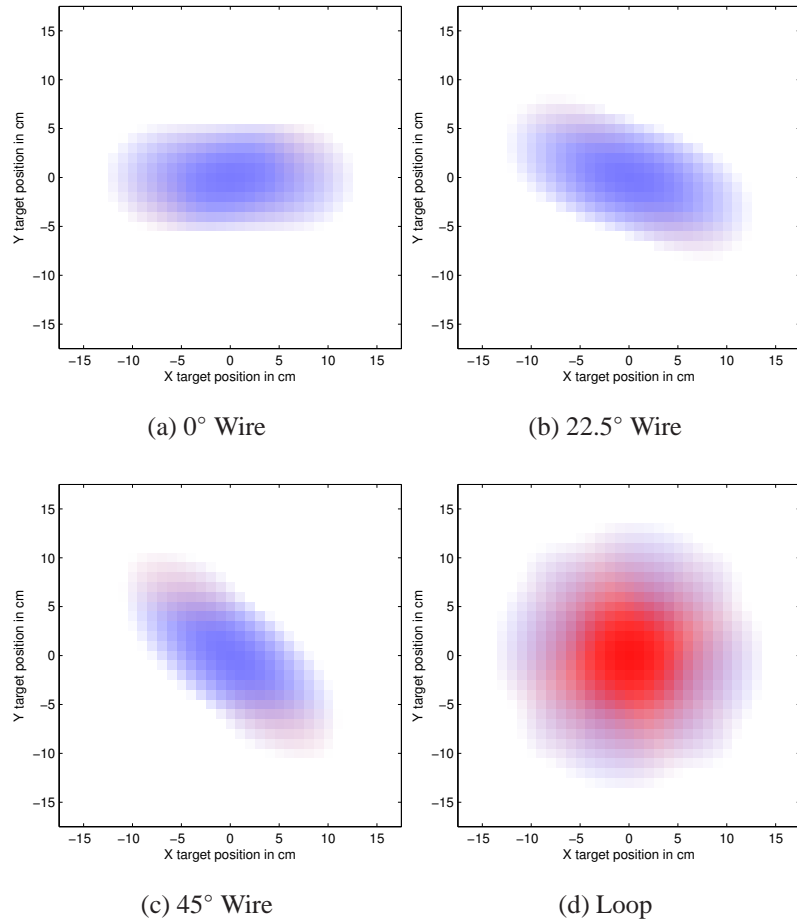


Figure 106: False color maps indicating the detection of targets obtained using the cross-polarization of Equation 39 and the co-polarization of Equation 41. White indicates that no target is detected, blue indicates that a linear type of target has been detected, and red indicates that a radially symmetric type of target has been detected.

## **CHAPTER 5**

### **WIRE TARGET ORIENTATION ANGLE ESTIMATION**

Once a linear target has been detected, it may be useful to know the spatial orientation. For example if a straight buried wire were detected, then knowing the spatial orientation would be very useful in finding the ends of the wire. In this chapter three methods for estimating the orientation angle of a linear target are presented. The first method uses linearly polarized scattering to search for angles that maximize the target response. This method is called the linear polarization sweep. The second method computes the angle of the linear target directly from the co-polarized and cross-polarized responses. This method is called the dual circular polarization phase comparison. The third method is similar to the phase comparison method, except that the phases of the co-polarized and cross-polarized responses are compared in the time-domain rather than the frequency domain. This method is called the instantaneous phase method.

#### **5.1 Linear Polarization Sweep Method**

When a linearly polarized wave is incident on a linear target, the scattered response depends greatly on the orientation angle of the linear target relative to the angle of polarization of the incident wave. When the linear target is parallel to the polarization direction of the incident wave, the scattered response is at a maximum. When the linear target is orthogonal to the polarization direction of the incident wave, the scattered response is at a minimum. This observation motivates the linear polarization sweep. By rotating the angle of incident linear polarization, the orientation angle of the linear target can be found by searching for the angle that produces the greatest scattered response. One way to achieve this would be to use linearly polarized antennas and physically rotate the antennas incrementally between measurements. While this approach would work, it would take a long time to repeat all of those measurements and perform the incremental antenna rotations. The linear polarization

sweep leverages the arbitrary polarization capabilities of the RVD-based CP antenna from Equation 19 to greatly speed up the process.

A diagram for the linear polarization sweep is shown in Figure 107. The transmitting and receiving antennas have both been rotated by angle  $\phi$  and are both parallel. The linear target is oriented at angle  $\theta$ . The response from the target is at a maximum when  $\phi = \theta$ .

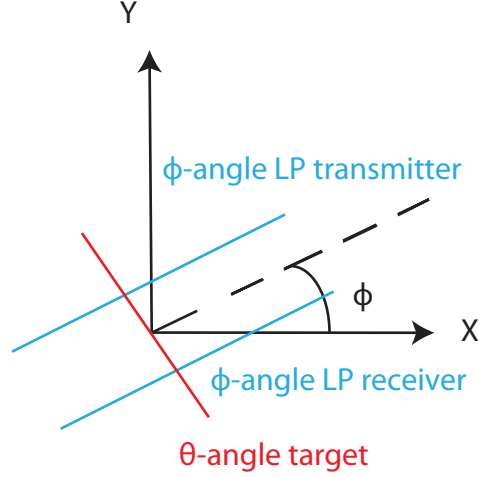


Figure 107: A diagram for the LP sweep method. The transmitting and receiving antennas have both been rotated by  $\phi$ . The linear target is at angle  $\theta$ .

For this method it is necessary to compute the angle- $\phi$  S-parameter corresponding to transmission and reception of linear polarization for antennas that have been rotated by  $\phi$ . To begin, the  $\phi$ -angle LP transmitter E field matrix is given by

$$E_{T\phi} = \cos(\phi)E_1 + \sin(\phi)E_3 = \begin{bmatrix} \cos(\phi)\alpha \\ \sin(\phi)\alpha \end{bmatrix} \frac{V}{L}, \quad (42)$$

where  $V$  is the input voltage, and  $\alpha$  is a constant. The transmitted E field matrix for the  $\phi$ -angle LP receiver is given by

$$E_{R\phi} = \cos(\phi)E_2 + \sin(\phi)E_4 = \begin{bmatrix} \cos(\phi)\alpha \\ \sin(\phi)\alpha \end{bmatrix} \frac{V}{L}. \quad (43)$$

The angle- $\phi$  S-parameter in terms of the four measurement pairs is

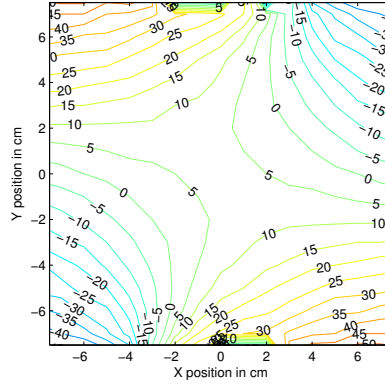
$$\begin{aligned}
S_\phi &= b \begin{bmatrix} \cos(\phi)\alpha & \sin(\phi)\alpha \end{bmatrix} \begin{bmatrix} p_{xx} & p_{xy} \\ p_{yx} & p_{yy} \end{bmatrix} \begin{bmatrix} \cos(\phi)\alpha \\ \sin(\phi)\alpha \end{bmatrix} \\
&= \cos^2(\phi)b\alpha^2 p_{xx} + \sin^2(\phi)b\alpha^2 p_{yy} + \sin(\phi)\cos(\phi)b\alpha^2 p_{xy} + \sin(\phi)\cos(\phi)b\alpha^2 p_{yx} \\
&= \cos^2(\phi)S_{21} + \sin^2(\phi)S_{43} + \sin(\phi)\cos(\phi)(S_{23} + S_{41}). \quad (44)
\end{aligned}$$

Equation 44 uses the same four measurement pairs as the co-polarization and cross-polarization measurements. Estimating the angle of a linear target can be done by finding the  $\phi$  which maximizes  $S_\phi$ . Because  $S_\phi$  is a frequency-domain quantity, the time-domain response peak-to-peak amplitude obtained from  $S_\phi$  is used instead. This results in a single estimate for the wire angle, rather than an estimate that varies with frequency.

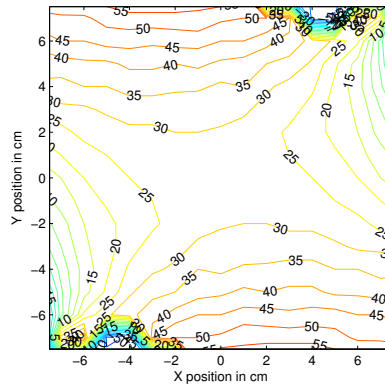
### 5.1.1 Numerical Results

The linear polarization (LP) sweep has been applied to numerical results from Chapter 2. The numerical results were produced in NEC2d. Since the orientation of the linear targets is precisely known for the numerical results, the accuracy of the LP sweep angle estimation can be evaluated. The LP sweep method is not applied to radially symmetric targets because radially symmetric targets do not have orientation angles.

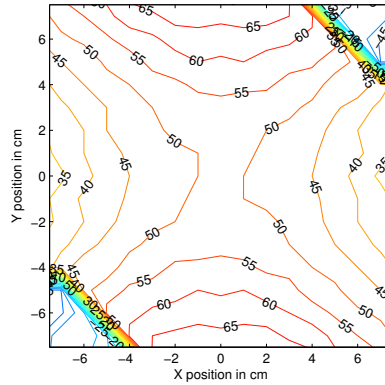
To estimate the angle of the linear target,  $S_\phi$  is computed at each measurement position, and  $\phi$  is varied from  $0^\circ$  to  $180^\circ$  in  $1^\circ$  steps. After  $S_\phi$  is computed for each  $\phi$ , the corresponding time-domain responses are computed. The  $\phi$  value which produces the greatest peak-to-peak amplitude in the time-domain response is selected as the best angle estimate. The antenna coupling is subtracted to focus on the response of the target. Contour graphs of angle estimates for 2D scans over wire targets are shown in Figure 108. The  $0^\circ$  wire is shown in Figure 108a, the  $22.5^\circ$  wire is shown in Figure 108b, and the  $45^\circ$  wire is shown in Figure 108c.



(a)  $0^\circ$  Wire Angle Estimate



(b)  $22.5^\circ$  Wire Angle Estimate



(c)  $45^\circ$  Wire Angle Estimate

Figure 108: Orientation angle LP sweep estimates (in degrees) for wire targets from numerical results.

When the antennas are directly over the target, and the target is at boresight, the angle estimation is its most accurate. The LP sweep estimates the orientation angles to be  $6^\circ$  for



the  $0^\circ$  wire,  $28^\circ$  for the  $22.5^\circ$  wire, and  $50^\circ$  for the  $45^\circ$  wire. The error in the LP sweep method seems to be approximately  $5^\circ$ . While the LP sweep method does not provide very precise orientation angle estimates, but the estimates are still quite useful.

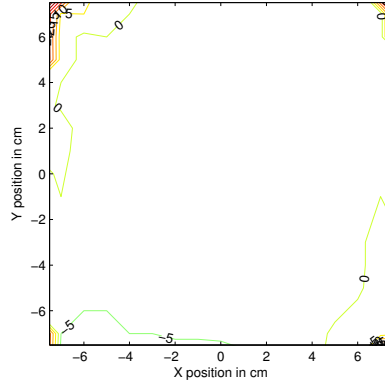
### 5.1.2 Experimental Results

The LP sweep has been applied to experimental results. The angle estimate is computed with the same method as for the numerical results. Contour graphs of angle estimates for 2D scans over wire targets in air are shown in Figure 109. The  $0^\circ$  wire is shown in Figure 109a, the  $22.5^\circ$  wire is shown in Figure 109b, and the  $45^\circ$  wire is shown in Figure 109c. All of the targets have an angle estimate that varies little over an area approximately 10 cm wide. This is not a serious problem. The area of the accurate angle estimate overlaps the area that the RVD-based CP antenna is capable of effectively distinguishing linear and radially symmetric targets. This means that angle estimates are available for identifiable linear targets.

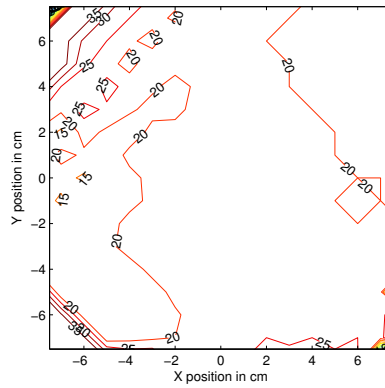
When the antenna is in the center of the scanning area and directly above each target, the angle of the  $0^\circ$  wire is estimated to be  $-3^\circ$ , the angle of the  $22.5^\circ$  wire is estimated to be  $21^\circ$ , and the angle of the  $45^\circ$  wire is estimated to be  $49^\circ$ . These angle estimates are fairly accurate, and they have about the same accuracy as the estimates for the numerical results.

Contour graphs of angle estimates for 2D scans over buried wire targets in sand are shown in Figure 110. The  $0^\circ$  wire is shown in Figure 110a, the  $22.5^\circ$  wire is shown in Figure 110b, and the  $45^\circ$  wire is shown in Figure 110c. For the buried targets, the response from the ground was time-gated away, so that the ground response would not interfere with the target angle estimates.

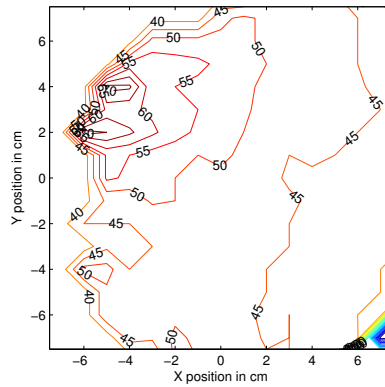
With the antenna directly above each target, the angle of the  $0^\circ$  wire is estimated to be  $-4^\circ$ , the angle of the  $22.5^\circ$  wire is estimated to be  $21^\circ$ , and the angle of the  $45^\circ$  wire is estimated to be  $50^\circ$ . These estimates are only slightly less accurate than those for targets in air.



(a)  $0^\circ$  Wire Angle Estimate

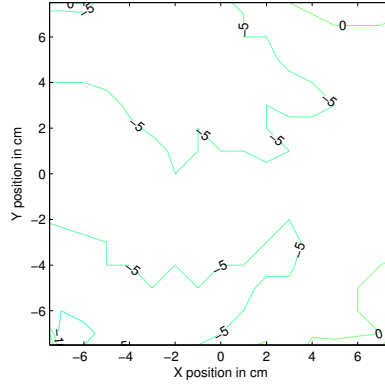


(b)  $22.5^\circ$  Wire Angle Estimate

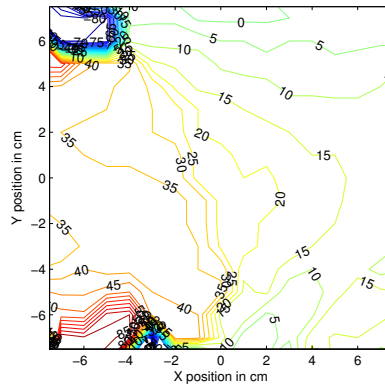


(c)  $45^\circ$  Wire Angle Estimate

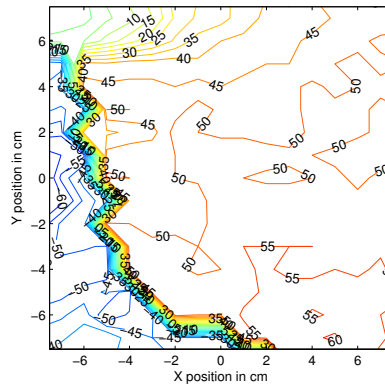
Figure 109: Orientation angle estimates for wire targets in air from experimental results.



(a)  $0^\circ$  Wire Angle Estimate



(b)  $22.5^\circ$  Wire Angle Estimate



(c)  $45^\circ$  Wire Angle Estimate

Figure 110: Orientation angle estimates (in degrees) for wire targets under ground from experimental results.

## 5.2 Dual CP Phase Comparison Method

The Phase Comparison method examines the effect of the angle of a linear target on the co-polarized and cross-polarized responses. While a linear target has co-polarized and cross-polarized responses that are equal in magnitude, the co-polarized and cross-polarized responses can differ in phase. The goal of this method is to determine how the angle of the linear target influences the phase difference between the co-polarized and cross-polarized responses. The angle estimate could be computed directly from the phase difference between the co-polarized response and the cross-polarized response.

The co-polarization and cross-polarization S-parameters from Equation 15 and Equation 16 must be redeveloped to find the  $\phi$ -dependence of  $S_{copol}$  and  $S_{xpol}$ . Instead of a generic polarizability matrix, the polarizability matrix is now

$$P = \begin{bmatrix} p\cos^2(\phi) & p\cos(\phi)\sin(\phi) \\ p\sin(\phi)\cos(\phi) & p\sin^2(\phi) \end{bmatrix}, \quad (45)$$

where  $\phi$  is the orientation angle of the ideal linear target and  $p$  is a constant. With the new scattering matrix, The co-polarization S-parameter becomes

$$\begin{aligned} S_{copol} &= \frac{b}{2} \begin{bmatrix} \alpha & j\alpha \end{bmatrix} \begin{bmatrix} p\cos^2(\phi) & p\cos(\phi)\sin(\phi) \\ p\sin(\phi)\cos(\phi) & p\sin^2(\phi) \end{bmatrix} \begin{bmatrix} \alpha \\ j\alpha \end{bmatrix} \\ &= \frac{\alpha^2 b p \cos^2(\phi) - \alpha^2 b p \sin^2(\phi) + j(\alpha^2 b p \cos(\phi)\sin(\phi) + \alpha^2 b p \sin(\phi)\cos(\phi))}{2} \\ &= \frac{\alpha^2 b p}{2} (\cos^2(\phi) - \sin^2(\phi) + j2\sin(\phi)\cos(\phi)). \end{aligned} \quad (46)$$

Similarly, the cross-polarization S-parameter is given by

$$\begin{aligned} S_{xpol} &= \frac{b}{2} \begin{bmatrix} \alpha & -j\alpha \end{bmatrix} \begin{bmatrix} p\cos^2(\phi) & p\cos(\phi)\sin(\phi) \\ p\sin(\phi)\cos(\phi) & p\sin^2(\phi) \end{bmatrix} \begin{bmatrix} \alpha \\ j\alpha \end{bmatrix} \\ &= \frac{\alpha^2 b p \cos^2(\phi) + \alpha^2 b p \sin^2(\phi) + j(\alpha^2 b p \cos(\phi)\sin(\phi) - \alpha^2 b p \sin(\phi)\cos(\phi))}{2} \\ &= \frac{\alpha^2 b p}{2}. \end{aligned} \quad (47)$$

It is worth noting that

$$|S_{copol}| = \frac{\alpha^2 bp}{2} = |S_{xpol}|, \quad (48)$$

as expected for the linear target. Although  $\angle S_{xpol} = 0$ , it is still necessary to get the co-polarization and cross-polarization phase difference because  $\angle S_{xpol}$  serves as a reference angle. So now the co-polarization S-parameter may be written as

$$S_{copol} = \frac{\alpha^2 bp}{2} e^{j\zeta}. \quad (49)$$

Now the  $\phi$ -dependence of  $\zeta$  may be expressed as

$$\begin{aligned} \angle S_{copol} - \angle S_{xpol} &= \zeta \\ &= \tan^{-1} \left( \frac{2\sin(\phi)\cos(\phi)}{\cos^2(\phi) - \sin^2(\phi)} \right) \\ &= \tan^{-1}(\tan(2\phi)) \\ &= 2\phi \end{aligned} \quad (50)$$

Therefore the orientation angle of the linear target is half of the phase difference between the co-polarization and cross-polarization responses. This provides a simple method for estimating the orientation angle for a linear target. Obtaining the actual phase difference between the co-polarization and cross-polarization responses may not be quite as simple. The coupling, clutter and noise would contribute to the phases of the co-polarization and cross-polarization measurements. The response of the wire target would have to be isolated. Equation 50 depends on frequency, since both  $\angle S_{copol}$  and  $\angle S_{xpol}$  depend on frequency. Therefore, it would be necessary to find a suitable range of frequencies to use for angle estimation and average the estimates over that frequency range.

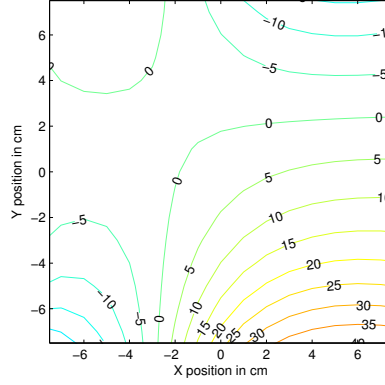
### 5.2.1 Numerical Results

The phase comparison method has been applied to numerical results from Chapter 2. To estimate the angle, first the co-polarization and cross-polarization were developed into the time-domain with the coupling subtracted. Next, the co-polarization and cross-polarization

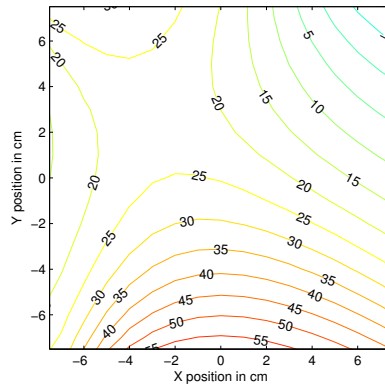
responses were FTed. Then the ratio of the responses was taken and the complex angle of the result was calculated. The result was divided by 2 to obtain orientation angle estimates. Finally, these estimates were averaged between 1 GHz and 4 GHz to produce a single estimate for the orientation angle.

Contour graphs of angle estimates for 2D scans over wire targets are shown in Figure 111. The  $0^\circ$  wire is shown in Figure 111a, the  $22.5^\circ$  wire is shown in Figure 111b, and the  $45^\circ$  wire is shown in Figure 111c. For all three targets, the estimates are accurate when the antenna is in a scanning position that is almost directly over the target.

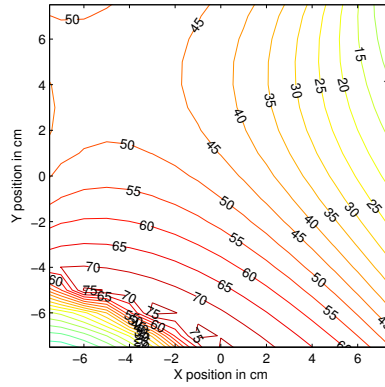
When the antenna is centered and the targets are at boresight, the phase comparison method estimates the orientation angles to be  $2^\circ$  for the  $0^\circ$  wire,  $25^\circ$  for the  $22.5^\circ$  wire, and  $47^\circ$  for the  $45^\circ$  wire. The error in the phase comparison method seems to be approximately  $2 - 3^\circ$ . This accuracy is slightly better than that of the LP sweep method.



(a)  $0^\circ$  Wire Angle Estimate



(b)  $22.5^\circ$  Wire Angle Estimate



(c)  $45^\circ$  Wire Angle Estimate

Figure 111: Orientation angle phase comparison estimates (in degrees) for wire targets from numerical results.

### 5.2.2 Experimental Results

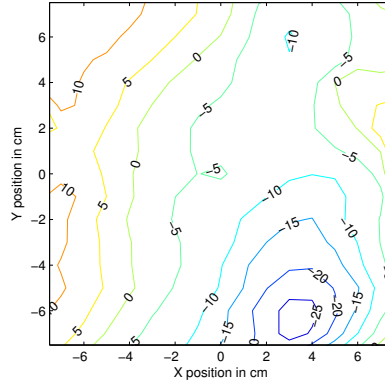
The phase comparison method has been applied to experimental results for targets in air and buried underground. The angle estimate is computed with the same method as for the numerical results. Contour graphs of angle estimates for 2D scans over wire targets in air are shown in Figure 112. The  $0^\circ$  wire is shown in Figure 112a, the  $22.5^\circ$  wire is shown in Figure 112b, and the  $45^\circ$  wire is shown in Figure 112c.

When the antenna is in the center of the scanning area and directly above each target, the angle of the  $0^\circ$  wire is estimated to be  $-4.7^\circ$ , the angle of the  $22.5^\circ$  wire is estimated to be  $26.4^\circ$ , and the angle of the  $45^\circ$  wire is estimated to be  $28.8^\circ$ . The accuracy is reduced compared to the numerical results, particularly for the  $45^\circ$  wire.

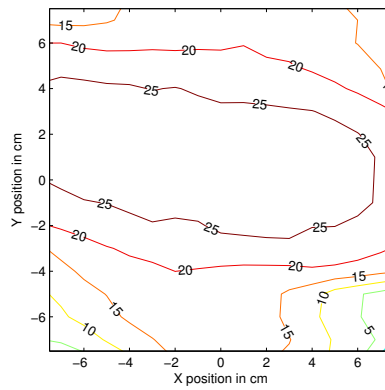
Contour graphs of angle estimates for 2D scans over wire targets in the ground are shown in Figure 113. The  $0^\circ$  wire is shown in Figure 113a, the  $22.5^\circ$  wire is shown in Figure 113b, and the  $45^\circ$  wire is shown in Figure 113c.

At the center of each scanning area, the angle estimates are  $-15.1^\circ$  for the  $0^\circ$  wire,  $13.1^\circ$  for the  $22.5^\circ$  wire, and  $48.3^\circ$  for the  $45^\circ$  wire. These estimates are a little bit less accurate, but they could still be valuable when compared to the case when no angle information is available.

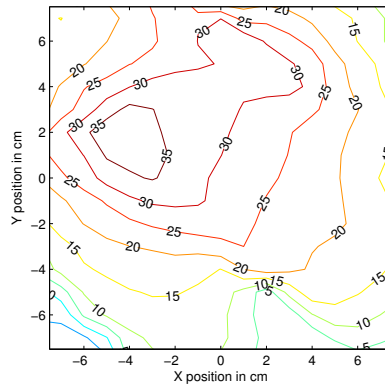




(a)  $0^\circ$  Wire Angle Estimate

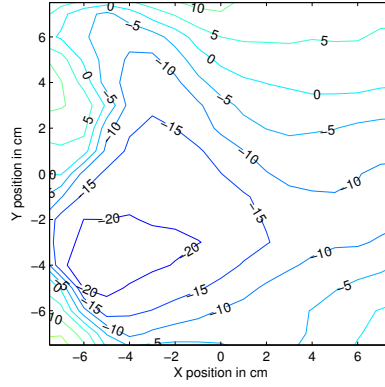


(b)  $22.5^\circ$  Wire Angle Estimate

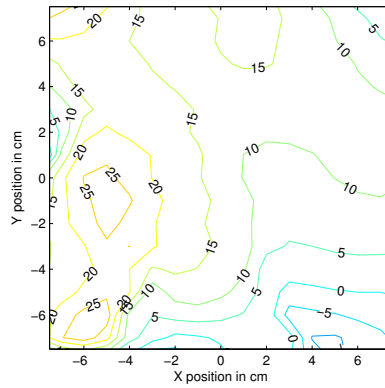


(c)  $45^\circ$  Wire Angle Estimate

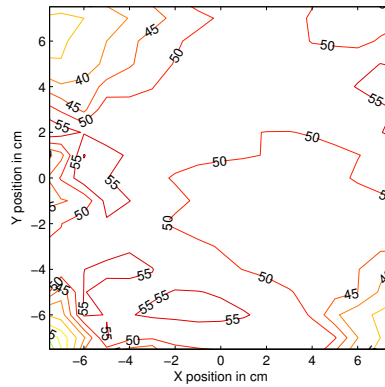
Figure 112: Orientation angle phase comparison estimates (in degrees) for wire targets in air from experimental results.



(a)  $0^\circ$  Wire Angle Estimate



(b)  $22.5^\circ$  Wire Angle Estimate



(c)  $45^\circ$  Wire Angle Estimate

Figure 113: Orientation angle phase comparison estimates (in degrees) for wire targets under ground from experimental results.

### 5.3 Instantaneous Phase Method

The Instantaneous Phase Method is similar to the Phase Comparison Method. This method uses another way to find  $\zeta$  and  $\phi$  in Equation 50. Rather than comparing the phases in the frequency-domain, the instantaneous phases of the co-polarization and cross-polarization responses are computed in the time-domain. This method should avoid any errors that arise from time-gating the wire target response and averaging the estimate for the orientation angle over a range of frequencies.

To compute the instantaneous phase, the Hilbert transform from Chapter 2 is used. The cross-polarization analytic signal is given by

$$s_{xpol}(t) = p_{xpol}(t) + jq_{xpol}(t), \quad (51)$$

where  $p_{xpol}(t)$  is the time-domain cross-polarization response, and  $q_{xpol}(t)$  is the Hilbert transform of  $p_{xpol}(t)$ . Similarly, the co-polarization analytic signal is given by

$$s_{copol}(t) = p_{copol}(t) + jq_{copol}(t), \quad (52)$$

where  $p_{copol}(t)$  is the time-domain co-polarization response, and  $q_{copol}(t)$  is its Hilbert transform. From Equation 50

$$P_{copol}(\omega) = P_{xpol}(\omega)e^{j\zeta}, \quad (53)$$

where  $P_{copol}(\omega)$  is the Fourier transform of  $p_{copol}(t)$ , and  $P_{xpol}(\omega)$  is the Fourier transform of  $p_{xpol}(t)$ . From linearity of Fourier transforms, it is also true that

$$s_{copol}(t) = s_{xpol}(t)e^{j\zeta}. \quad (54)$$

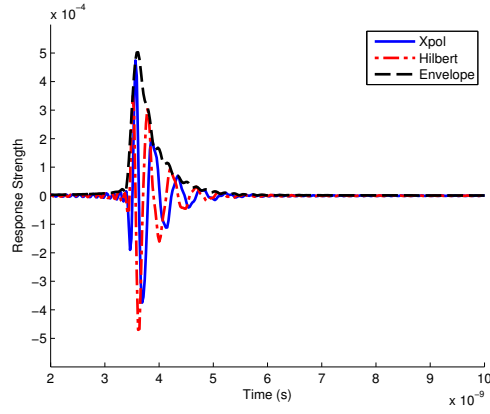
Therefore,  $\zeta$  may be computed as a function of time with

$$\zeta(t) = \arg \left( \frac{p_{copol}(t) + jq_{copol}(t)}{p_{xpol}(t) + jq_{xpol}(t)} \right). \quad (55)$$

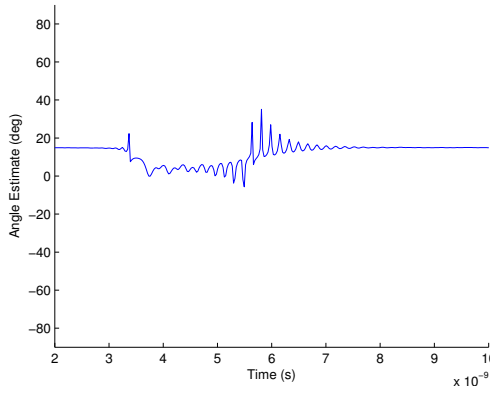
The orientation angle is half of  $\zeta$ . This method avoids having to guess a range of frequencies for the estimates. For this method a single orientation angle is estimated by finding the value of  $\frac{\zeta(t)}{2}$  at the time when  $|s_{xpol}(t)|$  reaches its maximum value.

### 5.3.1 Numerical Results

The Instantaneous Phase Method has been applied to the numerical results to obtain orientation angle estimates for the wire targets. In Figure 114 the instantaneous phase is compared to the cross-polarization response, its Hilbert transform, and its envelope signal. The angle estimate varies with time, but the valid angle estimates should occur between 3.5 ns and 4.0 ns when the cross-polarization response is its strongest. The angle estimate appears to be about  $15^\circ$  most of the time, but the angle estimate gets closer to  $0^\circ$  when the wire target response occurs.



(a) Xpol Signals

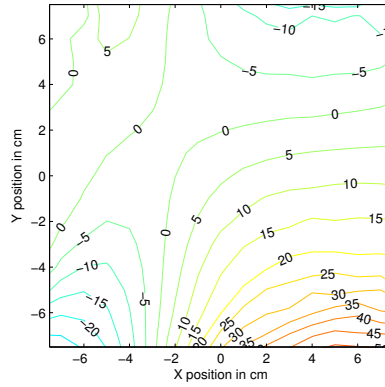


(b) Instantaneous Phase

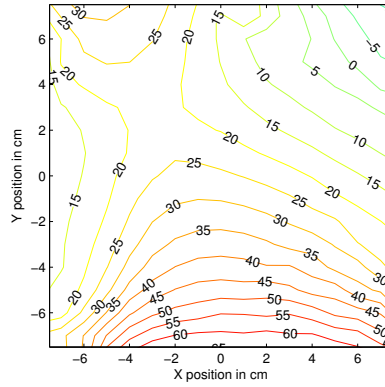
Figure 114: Time-domain pulses and the corresponding Instantaneous Phase of a  $0^\circ$  wire target.

Contours for the orientation angle estimates with the Instantaneous Phase Method are

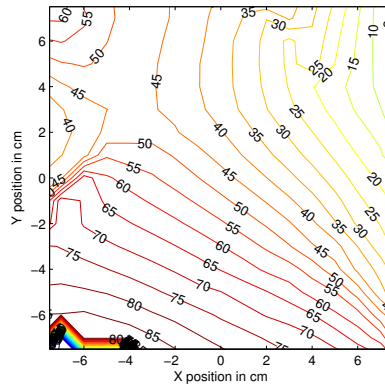
shown in Figure 115.



(a)  $0^\circ$  Wire Angle Estimate



(b)  $22.5^\circ$  Wire Angle Estimate



(c)  $45^\circ$  Wire Angle Estimate

Figure 115: Orientation angle estimates (in degrees) with the Instantaneous Phase Method for wire targets from numerical results.

When the antenna is centered and the targets are at boresight, the phase comparison

method estimates the orientation angles to be  $8^\circ$  for the  $0^\circ$  wire,  $26^\circ$  for the  $22.5^\circ$  wire, and  $47^\circ$  for the  $45^\circ$  wire. The error in the phase comparison method seems to be approximately  $2^\circ$ . This accuracy is a slight improvement over the LP sweep method.

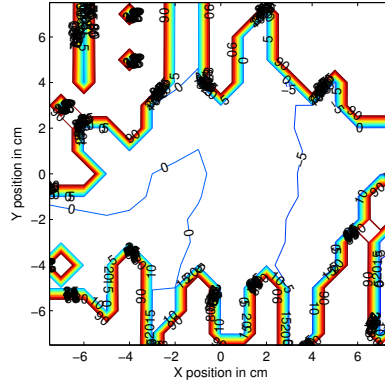
### **5.3.2 Experimental Results**

The Instantaneous Phase Method was applied to the experimental results of the wire targets in air. Contour graphs of the wire angle estimates over the scanning area are shown in Figure 116.

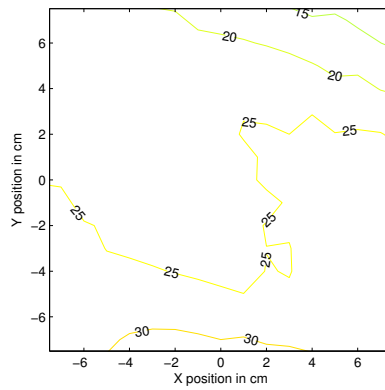
When the antenna is centered over the wire target, the angle estimates are  $-0.4^\circ$  for the  $0^\circ$  wire,  $22.9^\circ$  for the  $22.5^\circ$  wire, and  $46.4^\circ$  for the  $45^\circ$  wire. The estimates are all off by less than  $2^\circ$ . These estimates are very accurate, but there may be some small error in the positioning of the wire targets. Therefore, a significant amount of the error in the estimates could be due to error in positioning the wires.

The Instantaneous Phase Method was applied to the experimental results of the buried wire targets. Contour graphs of the wire angle estimates over the scanning area are shown in Figure 117.

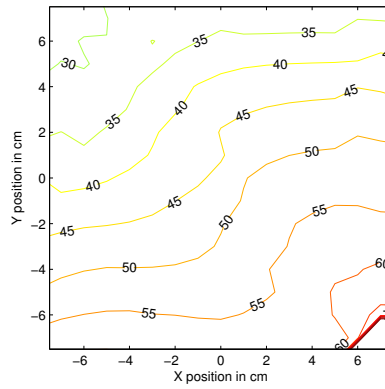
When the antenna is centered over the wire target, the angle estimates are  $-15^\circ$  for the  $0^\circ$  wire,  $23^\circ$  for the  $22.5^\circ$  wire, and  $44^\circ$  for the  $45^\circ$  wire. These estimates are fairly accurate.



(a)  $0^\circ$  Wire Angle Estimate

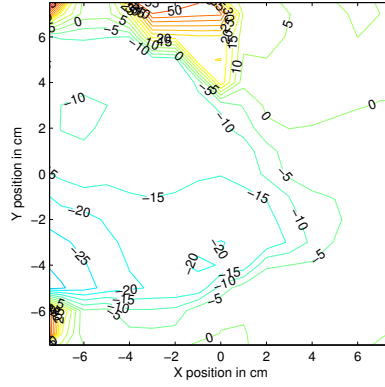


(b)  $22.5^\circ$  Wire Angle Estimate

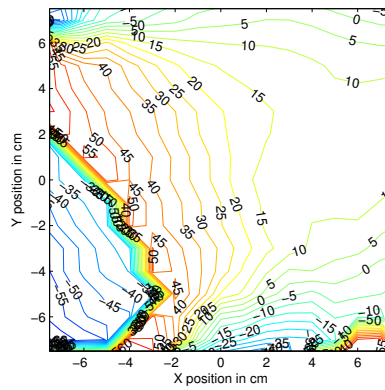


(c)  $45^\circ$  Wire Angle Estimate

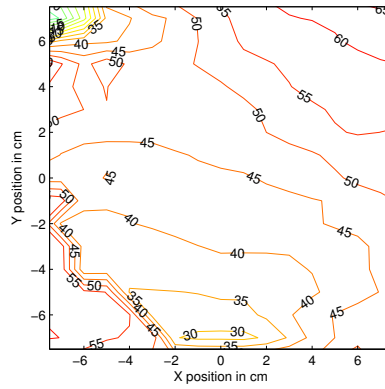
Figure 116: Orientation angle Instantaneous Phase Method estimates (in degrees) for wire targets in air from experimental results.



(a)  $0^\circ$  Wire Angle Estimate



(b)  $22.5^\circ$  Wire Angle Estimate



(c)  $45^\circ$  Wire Angle Estimate

Figure 117: Orientation angle Instantaneous Phase Method estimates (in degrees) for wire targets under ground from experimental results.



## 5.4 Method Comparison

To compare the three methods, the average errors are calculated for each method and summarized in Table 2. The phase comparison method has less error in the numerical results, but the LP sweep method has less error for the experimental results. The Instantaneous Phase method performed very well for the air experiments and performed better than the Phase Comparison method in both the ground and air experiments. The LP sweep method and Instantaneous Phase method also appears to be more consistent than the Phase Comparison method, providing estimates with less the  $10^\circ$  in error.

Table 2: Average angle estimate errors for the three angle estimation methods.

	<i>LP Sweep</i>	<i>Phase Comp.</i>	<i>Inst. Phase</i>
<i>Numerical</i>	5.5°	2.2°	4.5°
<i>Exp. Air</i>	2.8°	8.3°	0.7°
<i>Exp. Ground</i>	3.5°	9.3°	5.5°

Beyond the estimation accuracy, there are other important differences in the methods. If the LP sweep method were to be applied to an antenna other than the RVD-based CP antenna, such an antenna would necessarily have to provide arbitrary polarization. The phase comparison only requires that the antenna be capable of dual circular polarization.

The LP sweep method requires greater computational resources than the other methods. The computational costs of the LP sweep method increase with the estimation precision because  $S_\phi$  has to be calculated for more values of  $\phi$ . It only takes a few seconds of computation to obtain LP sweep estimates for the scanning area, so the computational costs would not be problematic. The phase comparison and instantaneous phase methods are a bit faster because they use the same co-polarization and cross-polarization responses that are used to identify the linear target.

## CHAPTER 6

### RESISTIVELY LOADED MODULATED SCATTERERS

Measuring antenna radiation patterns underground is useful in observing the position dependency of buried targets in ground penetrating radar (GPR). Since GPR's generally have separate transmit and receive antennas, two-way patterns that include the effects of both antennas are generally more useful than patterns of the individual antennas. A buried scatterer can be used for measuring underground radiation patterns, but it must be detectable to the radar and distinguishable from the clutter in the soil. A modulated scatterer meets these criteria by modulating between two or more states so that it is easily distinguishable from the soil clutter while remaining detectable. The modulated scatterers are also useful for evaluating the effects that changing the soil properties will have on the GPR.

A modulated scatterer usually achieves different states by changing its impedance. These two states are typically achieved by biasing and unbiasing a diode. By differencing the reflected signal measurements from the scatterer at the two different states, the scatterer becomes very detectable. The direct reflections from the clutter are removed through the differencing. However, multiple reflections from the clutter and RLMS are not removed by differencing, but the multiple reflections are usually much weaker than the direct reflections from the clutter objects. Figure 118 depicts the antenna radiation scattering off of the ground surface, the RLMS, and the underground clutter.

Since the responses of GPR systems are usually interpreted in the time-domain, it is important that the reflections from the scatterer be compact in time. Modulated scatterers are usually based on unloaded dipoles which reflect a relatively strong signal in a relatively narrow band that is dependent upon the length of the scatterer. The narrow-band response causes the reflection from an unloaded dipole to ring, which is unacceptable for GPR applications. In this work resistive loading is used to reduce the ringing and make the reflected signal more compact in time. The cost of the reduced ringing is a reduction of the

amplitude of the reflected signal.

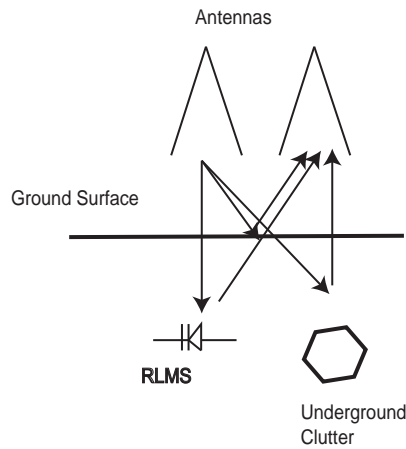


Figure 118: Scattering Diagram.

Considerable previous research has been performed using modulated dipole scatterers [43–51]. Modulated scatterers are typically used to measure near fields. Applications of modulated scatterers include near field testing for circuits and antennas [43]. One of the earliest applications of modulated scatterers was done by Cullen and Parr [44]. In their work, a spinning dipole scatterer was used to measure fields in free space. Modulated scatterers are typically detected over a narrow band of frequencies and viewed in the frequency-domain [45–47]. Modulated scatterers can be used in this way to measure the dielectric constant of the material that is embedded with a modulated scatterer. Lopez investigated optically and electrically modulated scatterers with and without resistive loading to detect the modulated scatterers between 2 GHz and 8 GHz [49]. Those modulated scatterers were toggled at 30 kHz and measured in the frequency domain, but their time-domain responses were not investigated. The modulated scatterers were detected in air and in sand, demonstrating that modulated scatterers could be useful in GPR applications. Muñoz has analyzed modulated scatterers in the time-domain [50, 51]. Those modulated scatterers were not resistively loaded, so the scattering was not compact in time. Inverse Fast Fourier Transforms (IFFT) were used to develop the swept frequency measurements

of this modulated scatterer into time-domain data. This modulated scatterer was measured both in air and oil. The modulated scatterer response was isolated with time-domain gating, then the modulated scatterer response was FFTed to observe the response in the frequency domain.

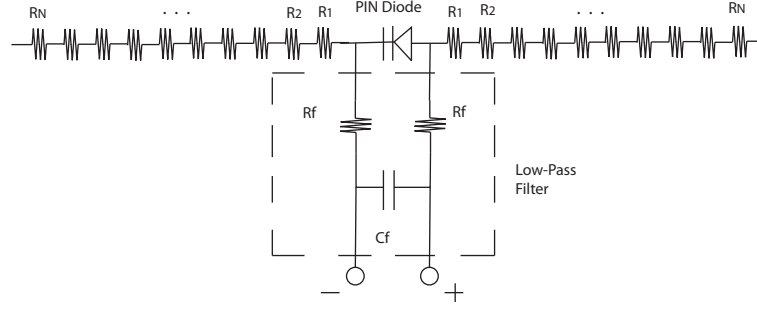
The following research uses a resistively-loaded modulated scatterer (RLMS). With measurements over a wide frequency range, the RLMS can be observed in the time domain through an IFFT. In this chapter, the RLMS resistive profile optimization is presented. The optimized resistive profile provides increased signal strength with low ringing. Next, the network analyzer measurement scheme is presented. The measurement scheme uses a standard network analyzer to reduce signal drift and obtain a relatively high signal-to-noise ratio for the RLMS response. Experimental results of the RLMS are presented from a Resistive-Vee Dipole radiation pattern experiment and from a GPR mini-hydrology experiment. Finally, the RVD-based CP antenna is used to detect the RLMS.

## 6.1 Modulated Scatterer Design Optimization

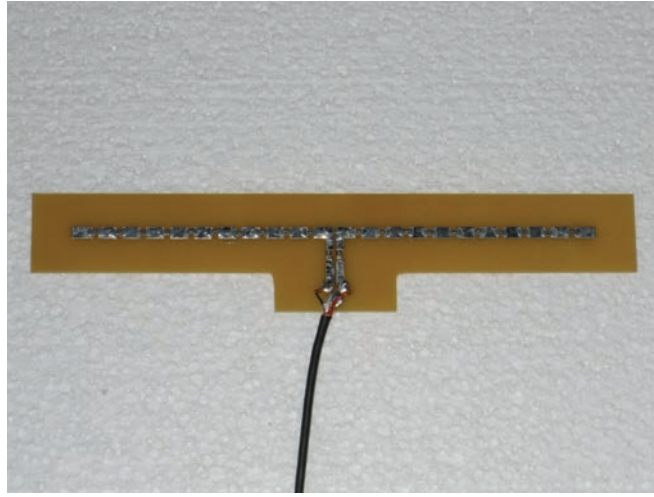
The Resistively-Loaded Modulated Scatterer (RLMS) is a modulated scatterer with a continuous resistive loading along the dipole arms. The resistive loading is achieved here by using surface mount resistors to approximate a conductivity taper along the dipole arms. The resistors along the dipole arms improve the bandwidth of the modulated scatterer at the cost of some signal strength.

The diagram for the RLMS is shown in Figure 119a and a photograph is shown in Figure 119. The RLMS is fabricated on a printed circuit board using surface mount components. An HPND-4005 PIN diode was selected to bridge the gap between the two RLMS arms because it has a low series resistance and a low capacitance. It behaves almost like a short circuit when biased and like an open circuit when unbiased. The RLMS arms are each 65 mm in length and have 10 resistors,  $R_1$  through  $R_{10}$ , spaced approximately 6 mm apart. A low-pass filter is used to isolate the RF signal from the biasing circuit. The low-pass filter

is formed from  $R_F$  and  $C_F$  with  $R_F = 240\ \Omega$  and  $C_F = 1.5\ nF$ .



(a) Circuit Diagram for the RLMS.



(b) Photograph of the RLMS.

Figure 119: Resistively-Loaded Modulated Scatterer (RLMS) designs.

The characteristics of the signal reflected from the scatterer can be adjusted by the choice of the resistors used to load the arms. The resistors are optimized to get a reasonable trade-off between the peak-to-peak amplitude and the amount of ringing of the reflected signal. The resistor values for the RLMS are chosen by discretizing the continuous modified Wu-King profile made by K. Kim [37], which is given by

$$R(z) = \left( \frac{1 - \frac{z}{h}}{R_1} + \frac{\left(1 - \frac{z}{h}\right)^2}{R_2} \right)^{-1}, \quad (56)$$

where  $z$  is the distance along the arm from the PIN diode,  $h$  is the length of each of the RLMS arms, and  $R_1$  and  $R_2$  are parameters varied to produce an optimum resistive profile.

To optimize the RLMS, it is modeled using NEC2d. An incident plane wave is simulated to travel perpendicularly to the RLMS arms. The RLMS was modeled in 10 MHz increments up to 8 GHz. The scattered electric field values are measured 1 m away from the RLMS to calculate the frequency-domain transfer function. The frequency-domain transfer function is multiplied by a frequency-domain Gaussian pulse of FWHM of  $2.65 \times 10^{-10}$  s and then IFFTed to obtain the time-domain reflected signal.

The RLMS was modeled for  $R_1$  and  $R_2$  values between  $0 \Omega$  and  $100 \Omega$ . The peak-to-peak field amplitude (PP) is defined as the difference between the maximum reflected signal value and the minimum reflected signal value. A metric for the time length of the reflected signal is defined as

$$C = \min_T m_n(T) = \min_T \int_{t=-\infty}^{\infty} |t - T| |S(t)| dt, \quad (57)$$

where  $t$  is time, and  $S(t)$  is given by

$$S(t) = \frac{U(t)}{\sqrt{\int_{t=-\infty}^{\infty} U(t)^2 dt}}, \quad (58)$$

where  $U(t)$  is the reflected signal. For reflected signals with very short durations,  $C$  is close to zero.

The correlation of  $C$  to the amount of ringing is demonstrated in Figure 120. The time-domain scattered fields have visibly less ringing when they also have a smaller value of  $C$ .

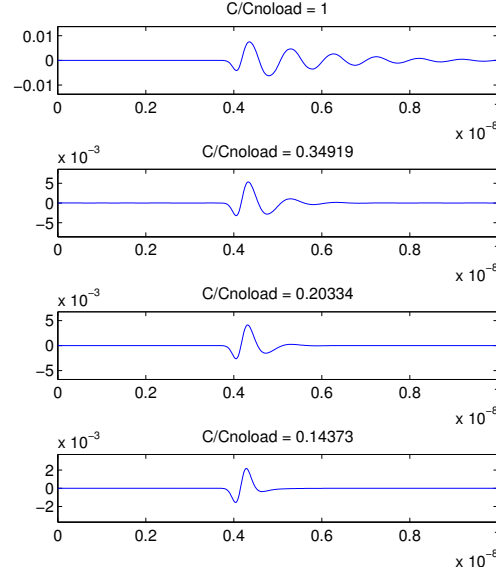


Figure 120: Time-domain scattered fields for a) unloaded modulated scatterer, b)  $R_1 = R_2 = 10 \Omega$ , c)  $R_1 = R_2 = 20 \Omega$ , and d)  $R_1 = R_2 = 60 \Omega$ .

Several of the  $R_1$  and  $R_2$  values that provide a balance of high peak-to-peak amplitude and low ringing are chosen as candidates for the optimized values. The time-domain reflected signals for the candidates are shown in Figure 121.

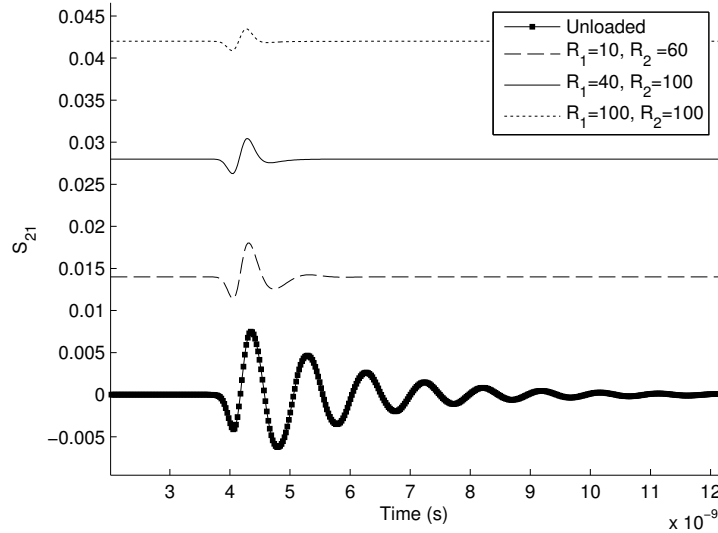


Figure 121: Reflected time-domain signals for the candidate resistor values.  $R_1 = 40 \Omega$  and  $R_2 = 100 \Omega$  (solid line) are chosen as the optimum parameter pair.

The parameter values  $R_1 = 40 \Omega$  and  $R_2 = 100 \Omega$  are selected empirically as the optimum parameters because they make the RLMS have low ringing, while the RLMS retains 30% of the peak-to-peak amplitude of the unloaded modulated scatterer. The other parameter values either result in too much ringing or insufficient peak-to-peak amplitude. These parameter values nearly maximize  $PP/C^{2.2}$  as shown in Figure 122. By tuning the exponent over  $C$ , it is possible to get a single metric that achieves a maximum value for the chosen resistive profile.

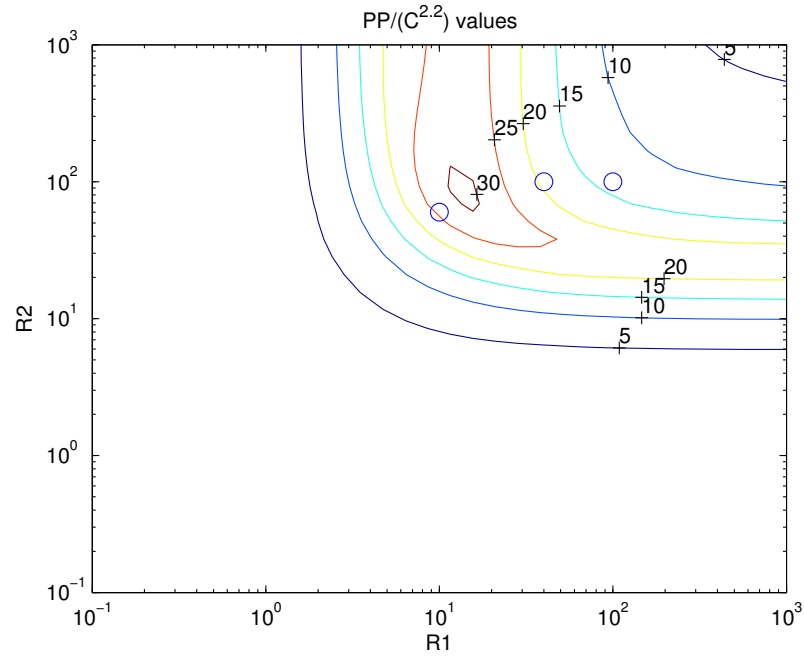


Figure 122: Contour plot of  $PP/C^{2.2}$ . The circle markers indicate the parameters for the resistive profiles selected in Figure 121.

The resistive profile is approximated with 10 surface mount resistors. These resistor values are shown in Table 3.



Table 3: Chosen resistor values and resistor positions along the arms for the RLMS.

	$R_1$	$R_2$	$R_3$	$R_4$	$R_5$	$R_6$	$R_7$	$R_8$	$R_9$	$R_{10}$
Position (mm)	6	12	18	24	30	36	42	48	54	60
Resistance ( $\Omega$ )	32	37	42	51	61	76	99	138	221	504

After the RLMS is assembled, it is sandwiched with silicone RTV between another piece of FR4. The sandwiching helps protect the electrical components of the RLMS when it is buried.

A diagram of the modulation circuitry is shown in Figure 123 and a photograph of the actual circuitry is shown in Figure 124.

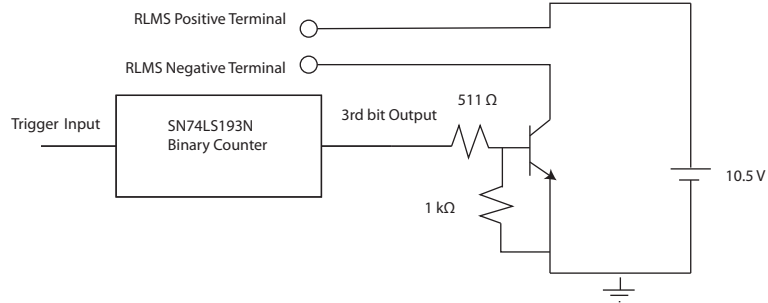


Figure 123: A diagram of the SN74LS193N binary counter and 2N 3904 transistor used to control the terminal voltage on the RLMS.

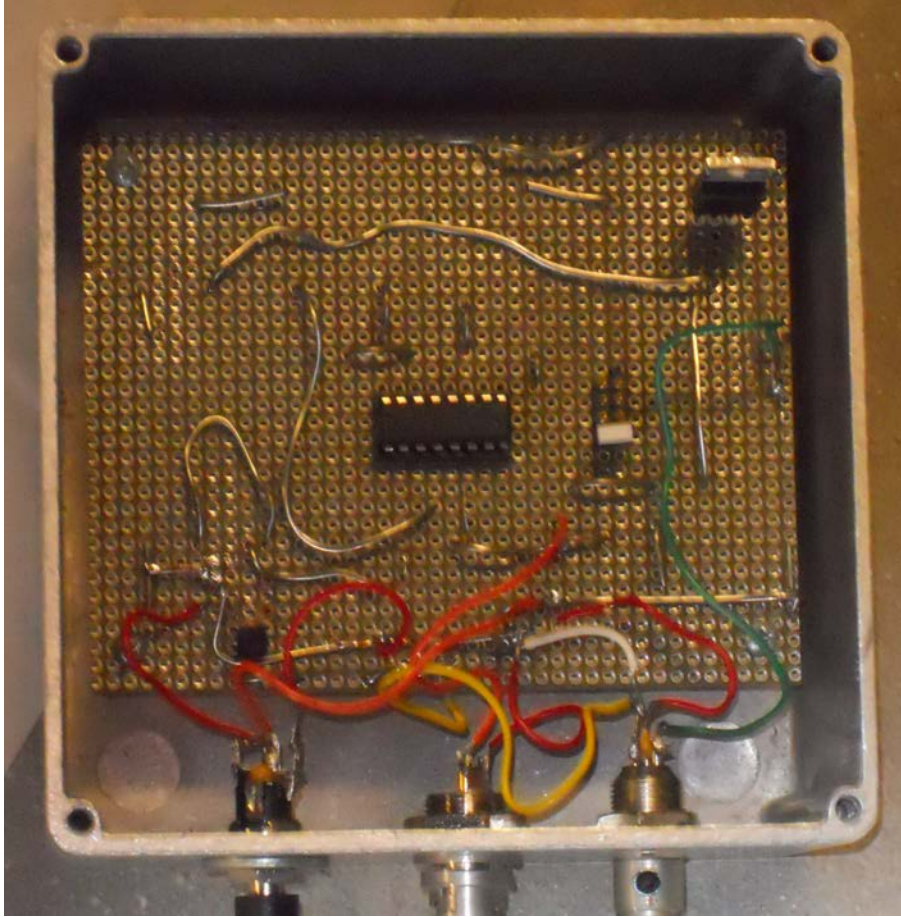


Figure 124: A photograph of the SN74LS193N binary counter and 2N 3904 transistor used to control the terminal voltage on the RLMS.

### 6.1.1 Measurement Setup

A pair of Resistive Vee Dipole (RVD) antennas detects the RLMS. These RVDs operate in bistatic mode, where one antenna transmits RF signals and the other receives them. The antennas are placed 0.165 m apart. RVD antennas were chosen because they work well over a wide range of frequencies and they have a low radar cross-section, which reduces multiple reflections. The RVD antennas were constructed for previous experiments by K. Kim [37]. The measurements are made using an Agilent Technologies E5071C Network Analyzer. The IF Bandwidth Network Analyzer is set to 1 kHz and the power is set to 10 dBm. The low IF Bandwidth and high power level improve the signal to noise ratio.

### 6.1.2 Resolving Time-Domain Reflected Signal

To demonstrate the RLMS, an experiment was set up using a pair of Resistive-Vee Dipole (RVD) antennas [37]. Usually a custom radar is used to measure the modulated scattering for this kind of experiment; however, in this work a method of using a standard network analyzer is developed. The method has several advantages such as having very broad bandwidth and being very well calibrated, but it has the disadvantage of being slower and less sensitive than a custom radar. These are acceptable trade-offs for a laboratory measurement. An Agilent Technologies E5071C network analyzer is used; the network analyzer measures the S-parameter,  $S_{21}$ , from 10 MHz to 8 GHz in 10 MHz increments with a 1 kHz IF bandwidth.

Normally the network analyzer makes a single measurement at each frequency, but for the modulated scatterer measurements, the network analyzer is set to make multiple measurements at each frequency. The external trigger output from the network analyzer is used to change the state of RLMS between measurements and keep the RLMS modulation synchronized with the measurements. At each frequency two ‘on’ measurements and two ‘off’ measurements are made. Then the network analyzer repeats the procedure for each frequency. The synchronization of the RLMS modulation and the network analyzer allows relatively rapid measurements of both RLMS states to reduce signal drift. A diagram of the measurement timing and modulation states is shown in Figure 125.

After the network analyzer measurements have been made, they must be processed to obtain time-domain reflected signals. At each frequency, the ‘on’ measurements are averaged, the ‘off’ measurements are averaged, and the difference of the two averages is taken. The differencing removes the antenna coupling and the undesired responses of the clutter. The incident pulse is chosen to be a Gaussian with a FWHM of  $2.65\text{e-}10$  s, and then the time-domain reflected signal is obtained from an IFFT.

The effect of toggling the RLMS on the measurements is shown in Figure 126.

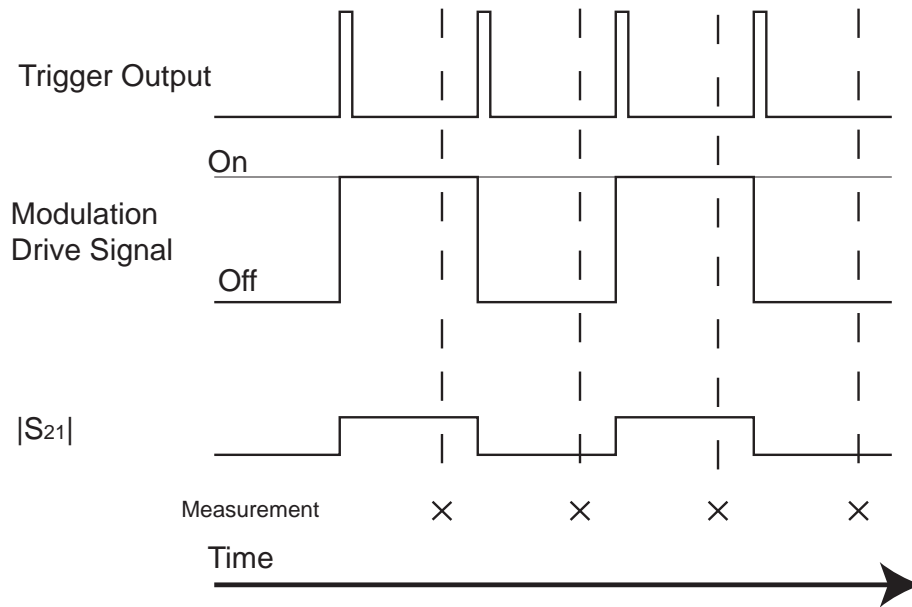


Figure 125: Measurement Timing Diagram.

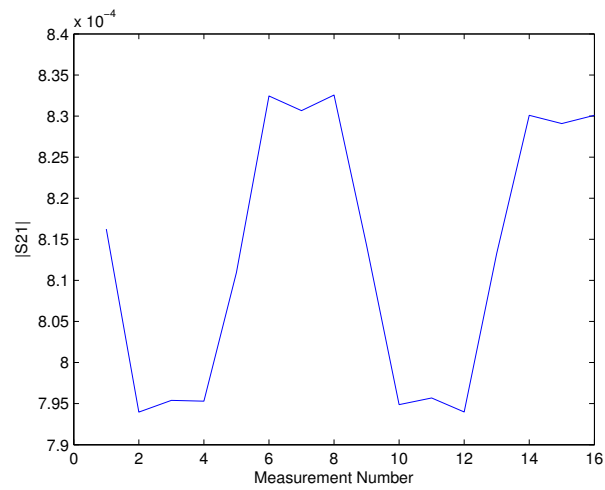


Figure 126:  $S_{21}$  magnitude measured at 2.5 GHz, RLMS 0.1016 m from antennas with the RLMS modulating.

An experiment was performed to demonstrate the RLMS. A diagram for the experiment is shown in Figure 127. The time-domain reflected signal for the RLMS is shown in Figure 128.

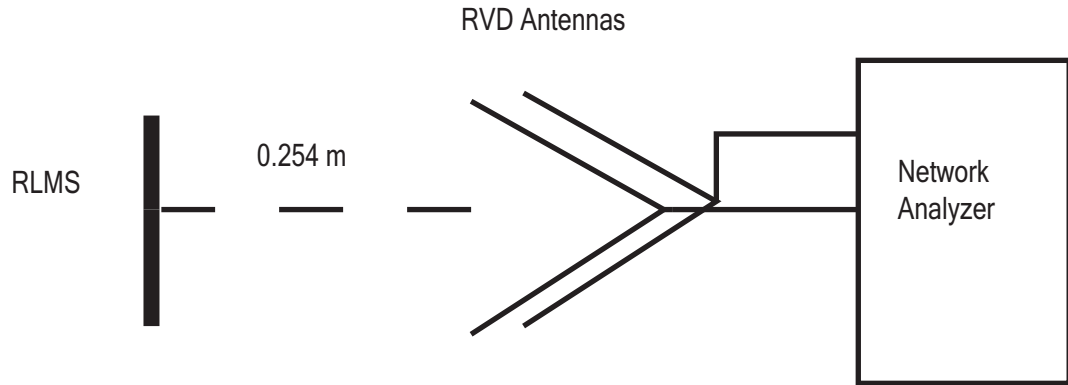


Figure 127: A diagram for an experiment with an RLMS positioned 0.254 m from the RVDs.

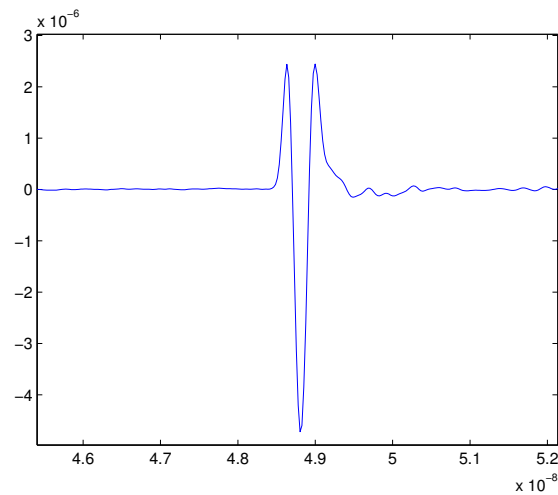


Figure 128: A Time-domain reflected signal from an RLMS positioned 0.254 m from the antennas.

For the example, the RLMS was positioned 0.254 m (10 in.) in front of the RVD antennas. The shape of the signal is no longer a Gaussian wave because the wave changes shape when it radiates from the first RVD antenna, when it scatters off of the RLMS, and when it is absorbed by the second RVD antenna.

## 6.2 Experimental Results

### 6.2.1 Biasing Network Analysis

The effects of the biasing network were investigated to try and further improve the performance of the RLMS. A new RLMS was designed to eliminate any effects the biasing network of the RLMS might have on the measurements. The resistance in the biasing network was significantly increased to meet this goal. The two  $240\ \Omega$  resistors that control the current to the RLMS PIN diode were replaced with  $750\ \Omega$  resistors. The voltage used to forward bias the PIN diode was increased from 10.5 V to 30 V. The  $750\ \Omega$  resistance was chosen to provide biasing current similar to the 10.5 Volt and  $240\ \Omega$  configuration.

The effects of increasing the resistances in the biasing network were modeled using NEC2d. Time-domain reflected signals for both the 10.5 Volt RLMS configuration and the 30 Volt RLMS configuration are shown in Figure 129.

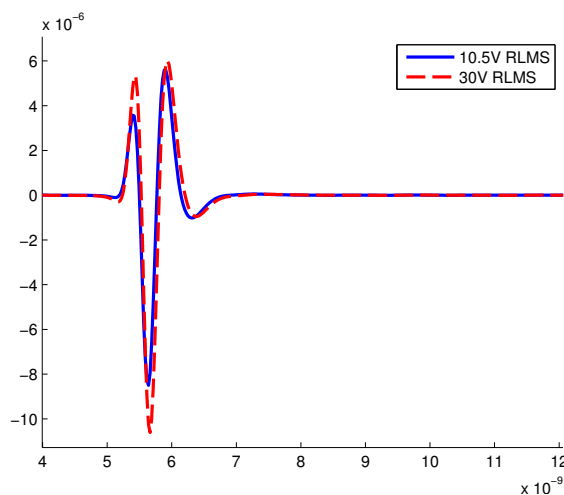


Figure 129: Time-domain reflected signals for the 10.5 Volt RLMS (solid blue line) and the 30 Volt RLMS (dashed red line) obtained from the NEC model.

The NEC2d model predicts that the 30 Volt RLMS shows up in the time-domain reflected signal with slightly higher peak-to-peak magnitude than the 10.5 Volt RLMS.

Experiments were performed to compare the 30 Volt RLMS to the 10.5 Volt RLMS. The RLMS's were measured with the RVD antennas from Section 6.1.2. The time-domain

reflected signals obtained from the measurements are shown in Figure 130.

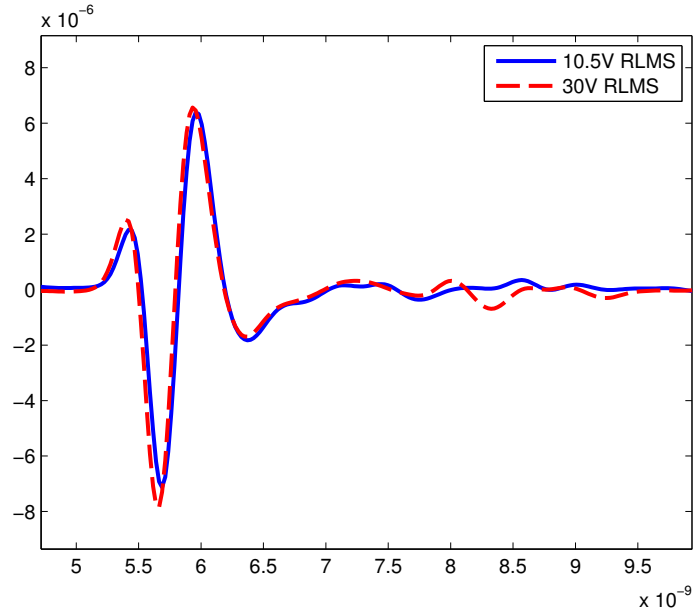


Figure 130: Time-domain reflected signals for the 10.5 Volt RLMS (solid blue line) and the 30 Volt RLMS (dashed red line) obtained experimentally.

The experimental results agree with the results predicted by the NEC model, but the 30 Volt RLMS does not significantly improve upon the 10.5 Volt RLMS. Since the 30 Volt RLMS does not perform much better than the 10.5 Volt RLMS and dissipates three times the power in the resistors, the following work assumes the use of the 10.5 Volt RLMS, except where it is stated otherwise.

### 6.2.2 Thin Substrate RLMS

A different RLMS was designed on a thin substrate. In the NEC2d models for the RLMS, the RLMS has no substrate because the NEC2d software is based on the Method of Moments and therefore does not support dielectrics. The thin substrate RLMS is meant to perform more like an RLMS with no substrate at all and demonstrate the value of comparing the NEC model RLMS to the RLMS with the thick substrate. The substrate is made from FR4 ( $\epsilon_r = 4.8$ ) as before, but it is now 0.0762 mm (0.003 in) thick. A photograph of the thin substrate RLMS is shown in Figure 131.

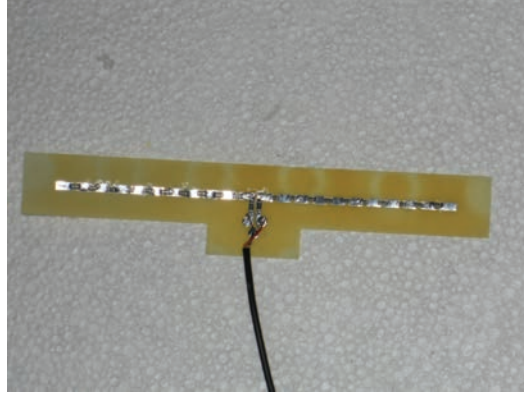


Figure 131: Photograph of the thin substrate Resistively-Loaded Modulated Scatterer

The thin RLMS has a few other changes as well. The terminal pads are closer to the dipole arms. The 1.5 nF capacitor is closer to the terminal pads. The 240  $\Omega$  resistors are closer to the capacitor and to the PIN diode. Experiments were performed to analyze the thin substrate RLMS. The RLMS was measured with the RVD antennas from Section 6.1.2. The time-domain reflected signals obtained from the thin substrate measurements and the NEC model are shown in Figure 132. For comparison, thick substrate time-domain reflected signals are shown in Figure 133.

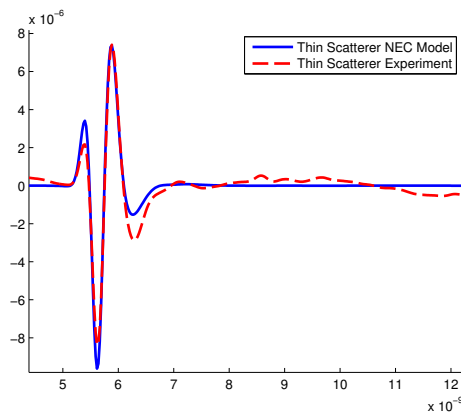


Figure 132: Time-domain reflected signals for the thin RLMS from an experiment (dashed red line) and a NEC model (solid blue line).



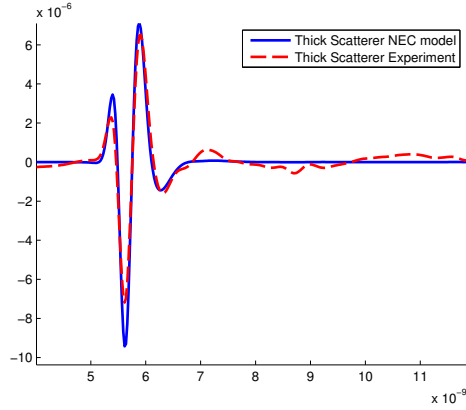


Figure 133: Time-domain reflected signals for the thick RLMS from an experiment (dashed red line) and a NEC model (solid blue line).

The thin RLMS measurements are in strong agreement with the NEC results during the 2nd and 3rd peaks in the time-domain reflected signal. The thick RLMS measurements show stronger agreement with NEC results mostly at the final peak. From these results, the thin RLMS does indeed provide a better match to the NEC model as predicted. Despite the limitation of not being able to model the substrate in the NEC software, NEC still produces a good model for the RLMS.

### 6.2.3 Resistive Vee Dipole Analysis

Using the RLMS developed in Section 6.1, the radiation pattern for the RVD antennas was measured. The antennas were used in bistatic mode. The RLMS was placed 0.356 m from the antennas. The RLMS was measured as it was moved 0.610 m to either side with measurements taken every 0.1016 m. The measurements were made with the procedure described in Section 6.1.2. Measurements were made from 10 MHz to 8 GHz in 10 MHz steps. A diagram of the experimental setup is shown in Figure 134.

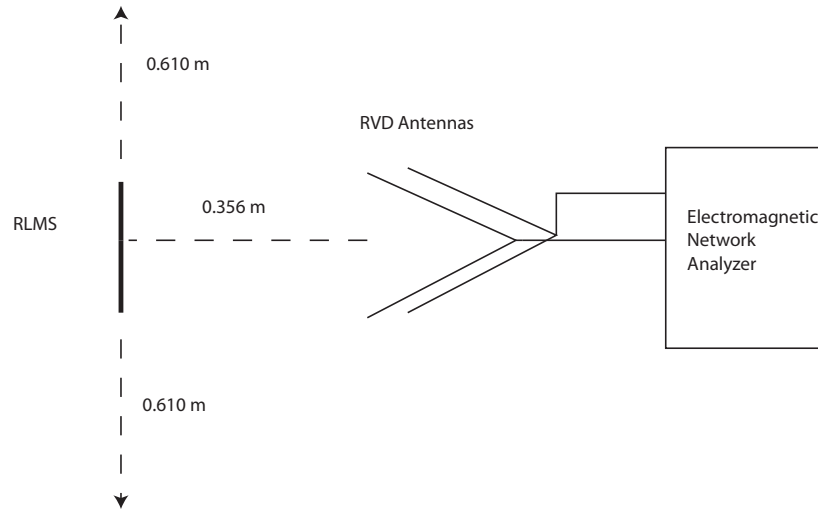


Figure 134: Experimental setup used for RVD radiation pattern measurements.

The results were reproduced with a NEC2d model. The experimental results and the simulation results are shown in Figure 135. In Figure 135, the signals from top to bottom were obtained by moving the RLMS from the left of the RVDs to the right in 0.1016 m increments, starting from 0.610 to the left of the RVDs.

As the RLMS moves away from the center, its reflected signal is delayed as the propagation distance increases. The signal loses strength as it moves away from the center because the signal attenuates over the increased propagation distance, and the RLMS scatters less energy as the angle between the incident E field and the RLMS arms increases.

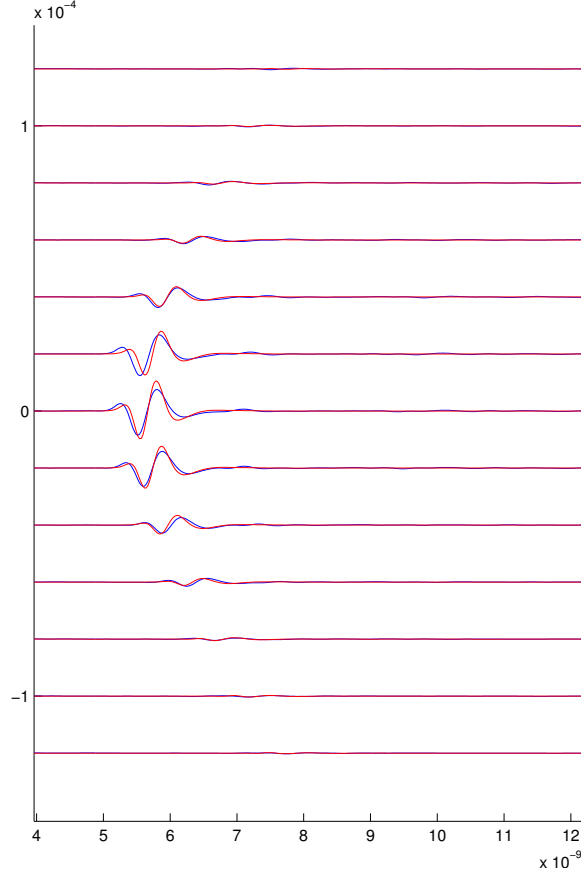


Figure 135: Experimental time-domain responses (blue) and simulation time-domain responses (red) for RVD radiation pattern measurements.

#### 6.2.4 Ground Penetrating Radar Hydrology Analysis

The hydrology studies in this work investigate the application of ground penetrating radar to the detection of underground water. There has been a significant amount of research done on ground water detection with radar systems.

There have been many studies on estimating volumetric water content based on measurements of the soil dielectric constant [52–57]. A model for the dielectric constant-water content relationship [58] is given by

$$\theta_v = -0.053 + 0.0292\epsilon - 5.5 * 10^{-4}\epsilon^2 + 4.3 * 10^{-6}\epsilon^3, \quad (59)$$

where  $\theta_v$  is the volumetric water content and  $\epsilon$  is the dielectric constant of the wet soil. It has been shown that bistatic measurements produce better estimates for volumetric water

content when the zenith angle and angle of incidence are both small [59]. Capacitance probes have been used to measure soil capacitance [56], which can be used to calculate the soil dielectric constant and the soil water content. The soil electrical parameters have also been calculated using network analyzer frequency-domain transfer functions [54].

Ground Penetrating Radar has been used to model the effects of the water content transition profile on ground water table detection [60,61]. The transition profile describes the soil saturation as a function of depth. The wet soil does not make a sharp interface with the dry soil. Above the water table, there is a layer of nearly saturated soil called the capillary fringe. The layer above the capillary fringe is the transition layer. In the transition layer, the saturation decreases continuously as depth decreases until the saturation reaches its minimum value. The transition layer can be 30 cm thick [60] or even 100 cm in some instances [61]. Thick transition layers reduce radar reflections, particularly those at high frequencies.

Another measurement technique uses neural networks to estimate soil moisture from radar backscatter measurements [62]. Surface soil moisture can be estimated with radar measurements made from an aircraft [63].

There have also been studies detecting the water table using Time-Domain Reflectometry (TDR). This method uses broadband radars to view reflected signals in the time domain [64,65]. TDR can provide measurements of propagation velocity, which can yield estimates of soil water content [65].

The work presented here uses a method similar to TDR, except that it differs in a very important way. While others use TDR to detect the wet soil interface, this work focuses on detecting the RLMS while trying to discriminate against other signals, such as the reflection off of the wet soil interface. The time-domain reflected signal from the RLMS contains information about the soil water content.

For the hydrology experiment, a cylindrical container 0.50 m high and 0.20 m in diameter was filled with sand. The RLMS was carefully buried 0.25 m deep into the sand.

Bistatic RVDs were positioned above the container facing downward. A diagram of the experiment is shown in Figure 136.

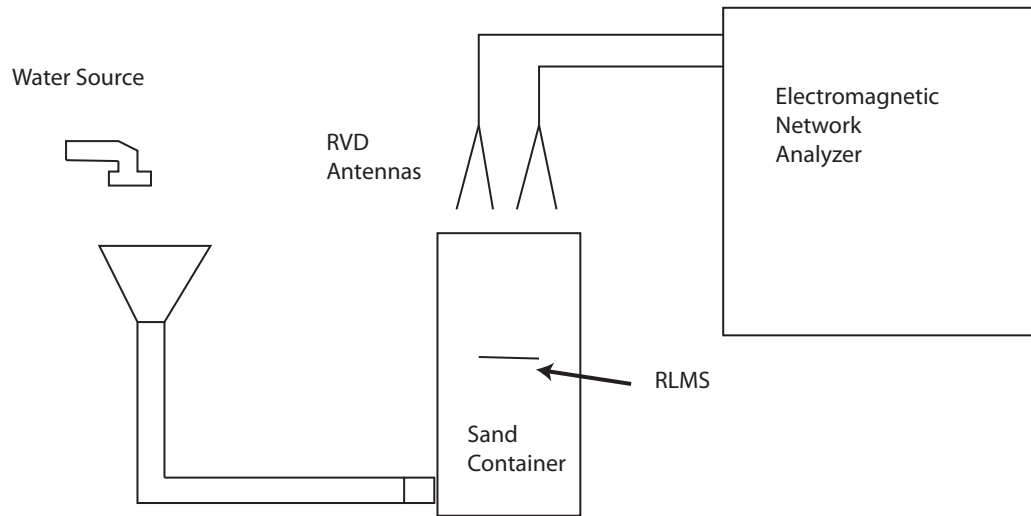


Figure 136: Experimental setup used for miniature hydrology experiment.

The container was very slowly filled with water from the bottom to the top. The RLMS was measured with the RVDs while the water slowly filled the container. Measurements started being recorded approximately 30 minutes prior to starting to fill the container with water.

The measurements for the hydrology experiment were performed according to the method described in Section 6.1.2 with a few exceptions. First, many measurements were performed consecutively to observe the container as it filled with water. Also, the first bit on the binary counter was used instead of the third bit to increase the speed of the measurements.

Increasing the speed of the measurements helps in two ways. First, it allows more measurements to be taken while the container fills with water. Second, it reduces the signal strength from reflection of the water interface. The water interface appears in the time-domain reflected signal because the switching function takes the difference of measurements taken at different times with slightly different water levels.

The results of the hydrology experiment are shown in Figure 137.

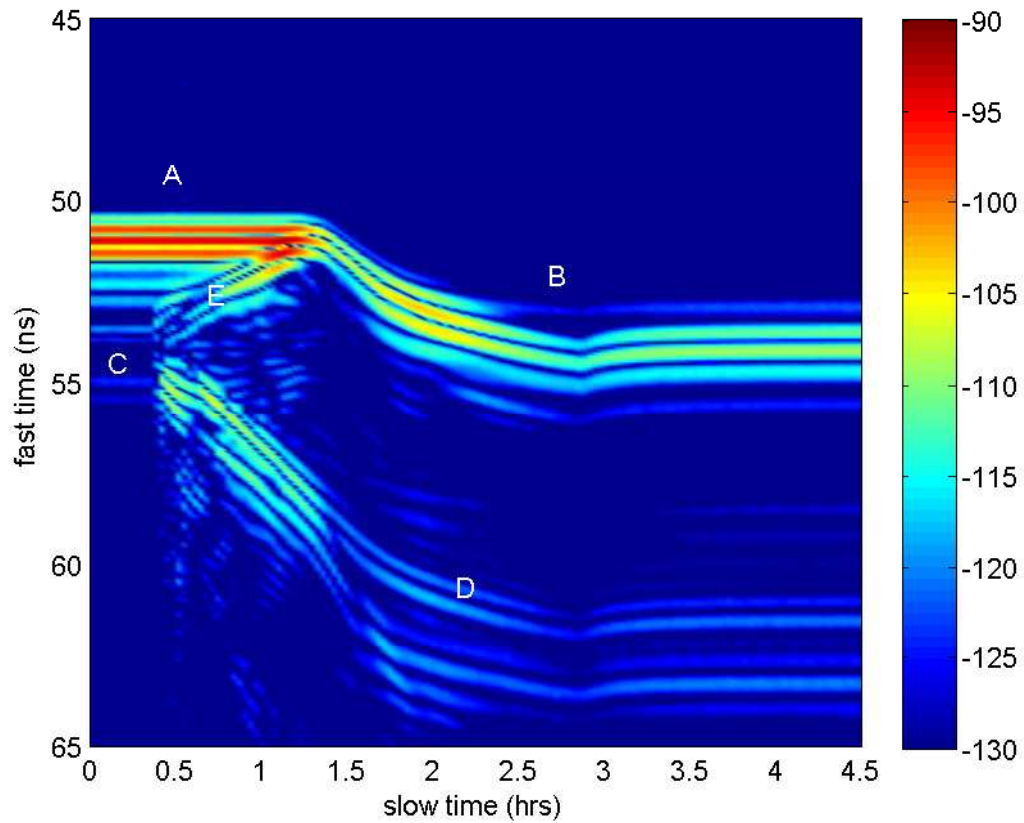


Figure 137: Experimental results from miniature hydrology experiment. The color scale goes from -130 dB to -90 dB.

Slow time is on the horizontal axis. Slow time refers to the time at which each time-domain reflected signal measurement was taken. Fast time is on the vertical axis. Fast time refers to the time over which the time-domain reflected signal varies. Each vertical cross-section of data represents a time-domain reflected signal measurement.

Initially, the response from the RLMS occurs at 51 ns (point A). The second response occurring at 54 ns is likely the shadow of the RLMS on the bottom of the container (point C). When the RLMS is 'on,' it scatters more energy and leaves a darker shadow. The shadow is visible because it changes when the RLMS modulates between states. After 0.5 hours of slow time, the water begins to fill the tank. The response at the bottom of the tank separates into two responses. As the water level rises past the RLMS, the reflected pulse

from the RLMS is delayed and weaker as a result of the lower propagation velocity and higher loss of the wet sand. Once the water level stops rising, the time-domain reflected signals stop changing. Initially, the response from the RLMS occurs at 51 ns. The second response occurring at 54 ns is likely the shadow of the RLMS on the bottom of the container. When the RLMS is 'on,' it scatters more energy and leaves a darker shadow. The shadow is visible because it changes when the RLMS modulates between states.

After 0.5 hours of slow time, the water begins to fill the tank. The response at the bottom of the tank separates into two responses. The first response is delayed as the water level in the tank rises. This response starts at about 54 ns, and it ends at about 62 ns. This response is likely the RLMS shadow on the bottom of the tank (point D). The delay is due to the lower propagation velocity in wet sand. The second response advances in fast time (point E). This response is caused by the wet sand and dry sand interface. Some of this response could be caused by the RLMS shadow on the wet sand interface, but it could also be caused by the small increase in water level between taking 'on' and 'off' measurements.

At about 2 hours, the water level rises past the RLMS, the reflected pulse from the RLMS is delayed and weaker as a result of the lower propagation velocity and higher loss of the wet sand (point B). Since the wet sand and dry sand interface is no longer visible after it rises past the RLMS, most of that response was caused by the RLMS shadow rather than the water level changes between measurements. The response of the RLMS is delayed from 51 ns to 53 ns.

After about 4.5 hours, the water is turned off. Once the water level stops rising, the time-domain reflected signals stop changing.

### **6.3 RLMS Measurements with the RVD-based CP Antenna**

A method is developed to extend the RLMS procedure in this chapter to work with a dual polarized antenna like the RVD-based CP antenna. The RVD-based CP antenna was then used to measure the response of the RLMS in the air and underground.

One significant issue with using CP on the RLMS is the increased measurement time. Measuring  $S_{21}$ ,  $S_{23}$ ,  $S_{41}$ , and  $S_{43}$  to synthesize CP would take four times as long as performing linearly polarized measurements with just  $S_{21}$ . It would be possible to increase the measurement speed by measuring  $S_{21}$  and  $S_{41}$  simultaneously and also measuring  $S_{23}$  and  $S_{43}$  simultaneously. By differencing the RLMS responses of different states, the RLMS becomes the only visible target. Therefore, geometry classification may not be useful for the RLMS.

A method was developed to perform measurements of the four S-parameters needed for CP while also toggling the RLMS. The measurement technique was implemented to detect the RLMS in the air and underground.

### **6.3.1 RLMS in Air**

For the RLMS in air experiment, the RLMS was placed onto a styrofoam pedestal above the ground. The RVD-based CP antenna was positioned 10 cm above the RLMS. A new measurement timing scheme was developed to synchronize the measurements with the RLMS state changes. The new measurement timing diagram is shown in Figure 138. The external trigger output of the network analyzer is set to produce a square wave pulse just before each measurement. The external trigger output is used to toggle the forward biasing of the RLMS PIN diode. At each frequency  $S_{21}$  is measured once while ‘on’ and once while ‘off,’ then this process is repeated three more times for each of the other S parameters. Next, the process is repeated for each frequency.



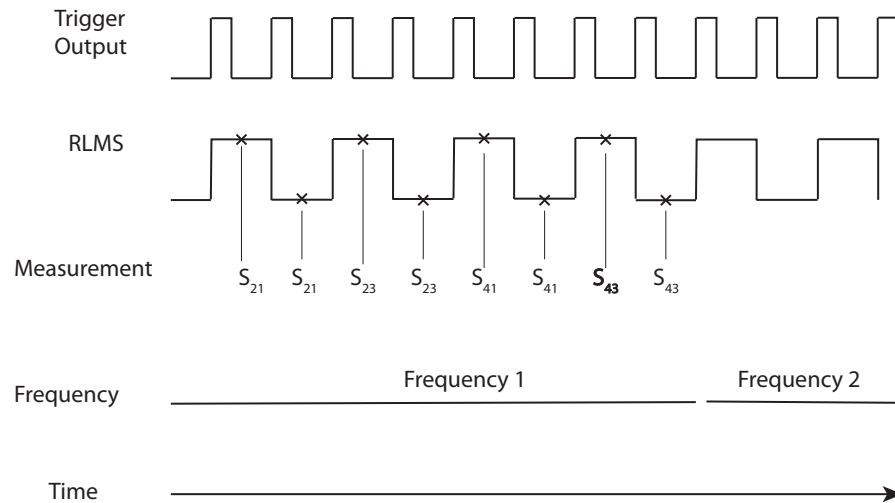


Figure 138: A timing diagram of the CP RLMS measurement.

Time-domain S-parameter responses are shown in Figure 139. The RLMS is mostly visible on  $S_{21}$  because RVDs 1 and 2 were parallel to the RLMS. The RLMS behaves like a linear target. The RLMS scatter gives the strongest response when it is parallel to the polarization of the transmitting and receiving antennas.

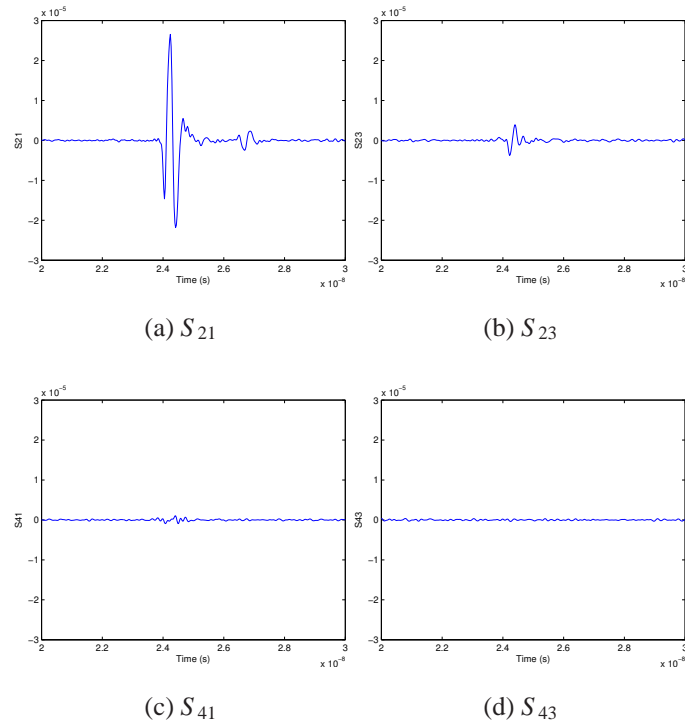


Figure 139: Four S-parameter time-domain responses of the RLMS.

Co-polarization and cross-polarization responses for the RLMS are shown in Figure 140. The RLMS has even cross-polarization and co-polarization, therefore the RLMS is a linear target.

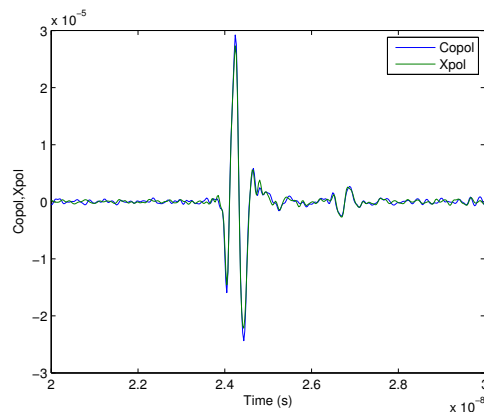


Figure 140: Co-polarization (blue) and cross-polarization (green) time-domain responses of the RLMS.

Lane scan results over the RLMS in air are shown in Figure 141. The RLMS shows up very clearly in both the co-polarization and cross-polarization responses. The second, much weaker response in both figures is likely the shadow of the RLMS on the ground. When the RLMS strengthens it's response by turning 'on,' it blocks some radiation from reaching objects by the RLMS. When the 'on' and 'off' measurements are differenced, the shadow is visible as well as the RLMS.

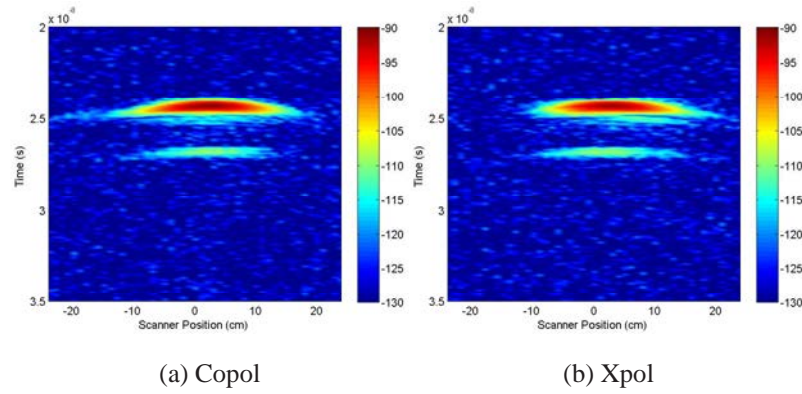


Figure 141: Co-polarization and cross-polarization responses versus time and position for the RLMS.

The results show that the CP detection of the RLMS works well.

### 6.3.2 RLMS in Ground

For the RLMS in ground experiment, the RLMS was buried 10 cm beneath the surface of the ground. The antenna was positioned 10 cm above the surface of the ground.

Time-domain S-parameter responses of the buried RLMS are shown in Figure 142. The RLMS is mostly visible on  $S_{21}$  because RVDs 1 and 2 were parallel to the RLMS.

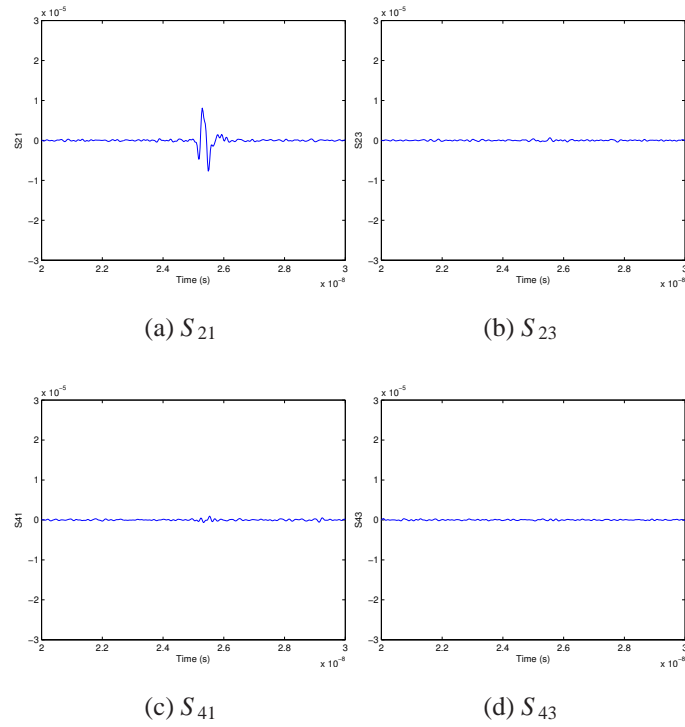


Figure 142: Four S-parameter time-domain responses of the buried RLMS.

Co-polarization and cross-polarization responses for the RLMS are shown in Figure 143. The RLMS appears clearly as in Figure 140, except that the response is weaker due to the longer path length.

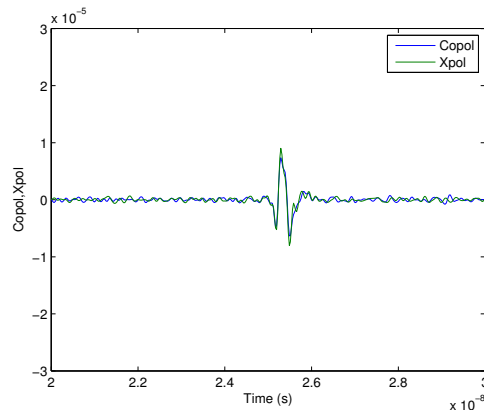


Figure 143: Co-polarization (blue) and cross-polarization (green) time-domain responses of the buried RLMS.

Center-lane scan results are shown in Figure 144. The RLMS appears clearly, and the response from the surface of the ground is not visible. These results show that the RLMS could be useful for measuring underground antenna radiation patterns.

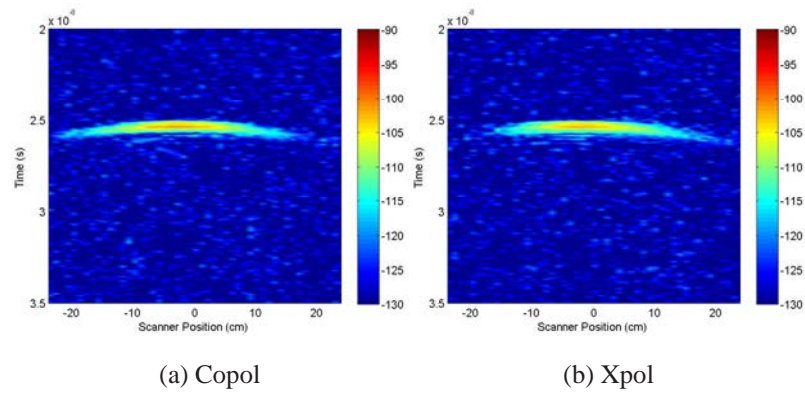


Figure 144: Co-polarization and cross-polarization responses versus time and position for the buried RLMS.

## CHAPTER 7

### CONCLUSIONS

In this thesis an RVD-based dual circularly polarized antenna is presented. The RVD is a very effective linearly polarized GPR antenna. The RVD-based CP antenna combines dual circular polarization capabilities with the GPR performance of the RVD. Using the dual CP measurements, the RVD-based CP antenna can accurately classify targets with linear geometry or radially symmetric geometry. The antenna provides effective target detection and target classification for GPR applications.

The main contribution of this work is development of the four-RVD dual CP antenna. Other antennas are capable of synthesizing dual CP, but the RVD-based CP antenna provides better performance for a GPR. The antenna is capable of making co-polarization and cross-polarization measurements that are suitable for comparison and use in geometry-based target classification. Other contributions are the new RVD design for improved CP synthesis and the three methods for estimating wire-target spatial-orientation angle. The main contribution of the resistively-loaded modulated scatterer work are the RLMS optimization of response strength and compactness. This design greatly improves the signal-to-noise ratio for the RLMS. The other contribution for the RLMS work is the network analyzer measurement procedure. The measurement procedure greatly reduces signal drift between the ‘on’ and ‘off’ measurements.

In Chapter 1 background information on the problem is presented. Previous methods for producing dual circular polarization are presented. The advantages of the RVD-based CP antenna are presented within the context of the previous methods. The advantages of the RVD-based CP antenna are low self clutter, a low radar cross-section, and wide-band performance.

In Chapter 2 the development of the RVD-based CP antenna is presented with numerical models. First, the configuration of the four RVDs is optimized to have low coupling

and provide good short range circular polarization. The coupling is lower with the RVDs farther apart, but the CP is better with the RVDs closer together. Through numerical modeling the optimized RVD configuration is found that efficiently reduces coupling and avoids losing circular polarization quality due to excessive spacing between the RVDs. Strong geometry-based target discrimination is shown in numerical models of the antenna with targets present.

In Chapter 3 a prototype antenna is constructed and used in experiments. The experiments are meant to show the accuracy of the numerical models and evaluate the performance of the antenna in GPR applications. Strong target discrimination is observed for targets in the air and targets in the ground. The antenna is shown to provide robust performance and fast target detection.

In Chapter 4 the design of the RVD is examined to further improve the circular polarization of the antenna. The shapes of the RVD arms and the resistive profile are optimized through numerical modeling to improve the circular polarization. The RVD redesign improves the off-boresight CP of the antenna for improved target classification of off-boresight targets.

In Chapter 5 three methods for estimating the orientation angle of a detected wire target are presented. The first method is the linear polarization sweep. It uses the arbitrary polarization capabilities of the antenna to synthesize linear polarization at all angles. The angle of linear polarization that has the largest response from the wire target has the same angle as the wire target. The second method is the phase comparison method. In this method the angle of the wire target is computed directly from the phase difference between the co-polarization and cross-polarization frequency-domain responses of the wire target. The third method is the instantaneous phase method. In this method the time-domain instantaneous phase difference of the co-polarization and cross-polarization responses is used to find the angle of the wire. All of the methods produce accurate angle estimates, but the instantaneous phase method is the more accurate method.

In Chapter 6 a broadband resistively-loaded modulated scatterer (RLMS) is developed for ground penetrating radar experiments. The RLMS is optimized to have a strong scattering response and a flat frequency response with linear phase variation. A method for detecting the RLMS with a standard network analyzer is presented. The measurement method reduces signal drift and improves the signal-to-noise ratio of the RLMS response. The RLMS is used to measure the two-way pattern of a pair of RVD antennas, and to measure the response of a scatterer in soil with a moving water table. The RVD-based CP antenna is used to improve detection of the RLMS.

One suggestion for future research is to improve the false color map in Chapter 2. It may be possible develop a new way to present the data that allows for more types of classification. It may also be possible to separate responses from targets that are very close together. Another suggestion for future research is to develop a multiple RLMS measurement setup. With multiple RLMS's buried underground at different depths, it could be possible to use the RLMS response to obtain estimates of the ground dielectric constant at different depths.



## REFERENCES

- [1] D. Daniels, *Surface-Penetrating Radar*. Institution of Electrical Engineers, 1996.
- [2] W. Sichak and S. Milazzo, "Antennas for circular polarization," *Proceedings of the IRE*, vol. 36, no. 8, pp. 997–1001, 1946.
- [3] G. Di Piazza, "Systems for resolving the sizes and centroid locations of buried objects," US Patent 3 775 765, 1973.
- [4] R. Dearnley, "High isolation dual polarized antenna using dipole radiating elements," US Patent 5 952 983, 1999.
- [5] G. Evans, "Antenna for producing circular polarization over wide angles," US Patent 3 541 559, 1970.
- [6] J.-W. Baik, K.-J. Lee, W.-S. Yoon, T.-H. Lee, and Y.-S. Kim, "Circularly polarised printed crossed dipole antennas with broadband axial ratio," *Electronics Letters*, vol. 44, no. 13, June 2008.
- [7] M. Gatti and D. Nybakken, "A circularly polarized crossed drooping dipole antenna," *Antennas and Propagation Society International Symposium, 1990. AP-S. Merging Technologies for the 90's. Digest. IEEE*, pp. 254–257, 1990.
- [8] E. Pelton and B. Munk, "Scattering from periodic arrays of crossed dipoles," *IEEE Transactions on Antennas and Propagation*, vol. 27, no. 3, pp. 323–330, May 1979.
- [9] B. Toh, "Understanding and measuring circular polarization," *IEEE Transactions on Education*, vol. 46, no. 3, 2003.

- [10] W.-S. Yoon, S.-M. Han, J.-W. Baik, S. Pyo, J. Lee, and Y.-S. Kim, "Crossed dipole antenna with switchable circular polarisation sense," *Electronics Letters*, vol. 45, no. 14, July 2009.
- [11] M. Zhang, Y. Chen, Y. Jiao, and F. Zhang, "Dual circularly polarized antenna of compact structure for rfid application," *Journal of Electromagnetic Waves and Applications*, vol. 20, no. 14, pp. 1895–1902, 2006.
- [12] J. Huang, "A technique for an array to generate circular polarization with linearly polarized elements," *IEEE Transactions on Antennas and Propagation*, vol. 34, no. 9, pp. 1113–1124, 1986.
- [13] T. Nakamura, "Circularly polarized crossed dipole," US Patent 6 163 306, 2000.
- [14] A. Eldek, A. Elsherbeni, and C. Smith, "Wide-band modified printed bow-tie antenna with single and dual polarization for c and x-band applications," *IEEE Transactions on Antennas and Propagation*, vol. 53, no. 9, pp. 3067–3072, September 2005.
- [15] J.-F. Li, B.-H. Sun, H.-J. Zhou, and Q.-Z. Liu, "Miniaturized circularly polarizing antenna using tapered meander-line structure," *Progress In Electromagnetics Research*, vol. 78, pp. 321–328, 2008.
- [16] K.-M. Mak, H. Wong, and K.-M. Luk, "A shorted bowtie patch antenna with a cross dipole for dual polarization," *IEEE Antennas and Wireless Propagation Letters*, vol. 6, pp. 126–129, 2007.
- [17] B. Kaswarra, W. Quddus, F. Scappuzzo, and M. S.N., "Circular polarization bandwidth for a bowtie turnstile over a ground plane," *Antennas and Propagation Society International Symposium, 2007 IEEE*, pp. 3544–3547, 2007.

- [18] S.-W. Qu, C. Chan, and Q. Xue, "Wideband and high-gain composite cavity-backed crossed triangular bowtie dipoles for circularly polarized radiation," *IEEE Transactions on Antennas and Propagation*, vol. 58, no. 10, pp. 3157–3164, October 2010.
- [19] V. Rumsey, "Frequency independent antennas," *In IRE International Convention Record*, vol. 5, pp. 114–118, March 1957.
- [20] A. Lestari, E. Bharata, A. Suksmono, A. Kurniawan, A. Yaravoy, and L. Ligthart, "A modified bow-tie antenna for improved pulse radiation," *IEEE Transactions on Antennas and Propagation*, vol. 58, no. 7, pp. 3157–3164, July 2010.
- [21] C. Van Coevorden, A. Bretones, M. Pantoja, F. Ruiz, S. Garcia, and R. Martin, "Ga design of a thin-wire bow-tie antenna for gpr applications," *IEEE Transactions on Geoscience and Remote Sensing*, vol. 44, no. 4, pp. 1004–1010, April 2006.
- [22] R. Kindt and D. Taylor, "Polarization correction in dual-polarized phased arrays of flared notches," *Antennas and Propagation (APSURSI), 2011 IEEE International Symposium on*, vol. 58, no. 10, pp. 1961–1964, July 2011.
- [23] T. Khuut, "Application of polarimetric GPR to detection of subsurface objects," Ph.D. dissertation, Tohoku University, 2009.
- [24] T. Nakamura, "Dual polarization vivaldi notch/ meander line loaded antenna," US Patent 6 842 154, 2005.
- [25] L. Ying and C. Ai-xin, "Design and application of Vivaldi antenna array," *Antennas, Propagation and EM Theory, 2008. ISAPE 2008. 8th International Symposium on*, pp. 267–270, 2008.
- [26] R. H. DuHamel, "Dual polarized sinuous antennas," US Patent 4 658 262, 1985.
- [27] M. Buck and D. Filipović, "Split-beam mode four-arm slot sinuous antenna," *IEEE Antennas and Wireless Propagation Letters*, vol. 3, pp. 83–86, 2004.

- [28] K. Saini and R. Bradley, “The sinuous antenna—a dual polarized element for wideband phased array feed application,” *Electronic Division Internal Memo N*, 1996.
- [29] R. O’Brien, “A log-periodic focal-plane architecture for cosmic microwave background polarimetry,” Ph.D. dissertation, University of California, Berkeley, 2010.
- [30] T. Hertel and G. Smith, “The conical spiral antenna over the ground,” *IEEE Transactions on Antennas and Propagation*, vol. 50, no. 12, pp. 1668–1675, 2002.
- [31] P. Lacko, C. Franck, M. Johnson, J. Ralston, M. Bradley, and B. McCummins, “Archimedean and log-spiral antenna comparison,” *Proceedings of SPIE*, vol. 4742, pp. 230–236, 2002.
- [32] J. Thaysen, K. B. Jakobsen, and H. R. Lenler-Eriksen, “Wideband cavity backed spiral antenna for stepped frequency ground penetrating radar,” *IEEE Symp. Antennas Propagation*, vol. 1B, pp. 418–421, 2005.
- [33] T. Iwasaki, A. Freundorfer, and K. Iizuka, “A unidirectional semi-circle spiral antenna for subsurface radars,” *IEEE Transactions on Electromagnetic Compatibility*, vol. 36, no. 1, February 1994.
- [34] M. McFadden, “Analysis of the equiangular spiral antenna,” Ph.D. dissertation, Georgia Institute of Technology, 2009.
- [35] J. Dyson, “The equiangular spiral antenna,” *IRE Transactions on Antennas and Propagation*, vol. 7, no. 2, pp. 181–187, 1959.
- [36] —, “The unidirectional equiangular spiral antenna,” *IRE Transactions on Antennas and Propagation*, vol. 7, no. 4, pp. 329–334, 1959.
- [37] K. Kim and W. Scott, “Design of a resistively-loaded vee dipole for ultra-wideband ground-penetrating radar applications,” *IEEE Transactions on Antennas and Propagation*, vol. 53, no. 8, pp. 2525–2532, 2005.

- [38] T. Wu and W. King, "The cylindrical antenna with nonreflecting resistive loading," *IEEE Transactions on Antennas and Propagation*, vol. 13, no. 3, pp. 369–373, 1965.
- [39] T. Counts, "Multistatic ground-penetrating radar experiments," *IEEE Transactions on Geoscience and Remote Sensing*, vol. 45, no. 8, pp. 2544–2553, 2007.
- [40] J. Venkatesan, "Investigation of the double-y balun for feeding pulsed antennas," Ph.D. dissertation, Georgia Institute of Technology, 2004.
- [41] J. Sustman and W. R. Scott, "A resistive-vee dipole based polarimetric antenna," *Antennas and Propagation Society International Symposium (APSURSI), 2013 IEEE*, pp. 888–889, 2013.
- [42] ———, "Polarimetric antenna for ground penetrating radar based on the resistive-vee dipole," *SPIE Defense, Security, and Sensing*, pp. 870 912–870 912, 2013.
- [43] J. Bolomey and F. Gardiol, *Engineering Applications of the Modulated Scatterer Technique*. Artech House Inc., 2001.
- [44] A. Cullen and J. Parr, "A new perturbation method for measuring microwave fields in free space," *Proceedings of IEE*, vol. 102, pp. 836–844, 1955.
- [45] D. Hughes and R. Zhougi, "A novel method for determination of dielectric properties of materials using a combined embedded modulated scattering and near-field microwave techniques-part ii: Dielectric property recalculation," *IEEE Transactions on Instrumentation and Measurement*, vol. 54, no. 6, pp. 2398–2401, 2005.
- [46] G. Freiburger and R. Zhougi, "Dielectric material characterization by complex ratio of embedded modulated scatterer technique states," *Instrumentation and Measurement Technology Conference 2005*, pp. 67–71, 2005.

- [47] G. Hygate, "A modulated scatterer for measuring microwave fields," *IEE Colloquium on Calibration of Antennas for Close Range Measurements*, vol. 24, no. 3, pp. 1–4, 1990.
- [48] F. Smith, R. Thompson, W. Liang, R. Clarke, and P. Lederer, "Use of a surface wave cell and an optically modulated scatterer to evaluate the propagation properties of surface waves," *IEEE Transactions on Antennas and Propagation*, vol. 52, no. 7, pp. 1871–1878, 2004.
- [49] R. Lopez and W. S. Jr., "Measurement of ground-penetrating radar antenna patterns using modulated scatterers," *Proceedings of SPIE*, vol. 5794, pp. 459–469, 2005.
- [50] K. Munoz and R. Zhougi, "Improvement of probe response extraction using time domain gating for embedded modulated scatterer technique," *Materials Evaluation*, vol. 66, no. 10, pp. 1084–1090, 2008.
- [51] —, "Application of swept frequency measurements to the embedded modulated scatterer technique," *Proc. of the 3rd International Conference on Electromagnetic Near-Field, Characterization and Imaging*, pp. 176–181, 2007.
- [52] J. Curtis, "Moisture effects on the dielectric properties of soils," *IEEE Transactions on Geoscience and Remote Sensing*, vol. 39, no. 1, pp. 125–128, January 2001.
- [53] V. Kleskchenko, S. Komarov, V. Mironov, and A. Romanov, "Dielectric properties of salted grounds in microwave band," *1998 IEEE International Geoscience and Remote Sensing Symposium Proceedings*, vol. 2, pp. 992–994, July 1998.
- [54] J. Minet, S. Lambot, G. Delaide, J. Huisman, H. Vereecken, and M. Vanclooster, "A generalized frequency domain reflectometry modeling technique for soil electrical properties determination," *Vadose Zone Journal*, vol. 9, pp. 1063–1072, 2010.

- [55] Y. Nakashima, H. Zhou, and M. Sato, "Estimation of groundwater level by gpr in an area with multiple ambiguous reflections," *Journal of Applied Geophysics*, vol. 47, pp. 241–249, 2010.
- [56] R. Van Overmeeren, S. Sariowan, and J. Gehrels, "Ground penetrating radar for determining volumetric soil water content; results of comparative measurements at two test sites," *Journal of Hydrology*, vol. 197, pp. 316–338, 1997.
- [57] G. Topp and J. Davis, "Measurement of soil water content using time-domain reflectometry (tdr): A field evaluation," *Soil Science Society of America Journal*, vol. 49, no. 1, pp. 19–24, 1984.
- [58] G. Topp, J. Davis, and A. Annan, "Electromagnetic determination of soil water content: Measurements in coaxial transmission lines," *Water Resources Research*, vol. 16, no. 3, pp. 574–582, 1980.
- [59] N. Pierdicca, L. Pulvirenti, F. Ticonni, and M. Brogioni, "Radar bistatic configurations for soil moisture retrieval: A simulation study," *IEEE Transactions on Geoscience and Remote Sensing*, vol. 46, no. 10, pp. 3252–3264, October 2008.
- [60] M. Bano, "Effects of the transition zone above a water table on the reflection of gpr waves," *Geophysical Research Letters*, vol. 33 L13309, 2006.
- [61] A. Saintenoy and J. Hopmans, "Ground penetrating radar: Water table detection sensitivity to soil water retention properties," *IEEE Journal of Selected Topics in Applied Earth Observations and Remote Sensing*, vol. 4, no. 4, pp. 748–753, December 2011.
- [62] M. Dawson, A. Fung, and M. Manry, "A robust statistical-based estimator for soil moisture retrieval from radar measurements," *IEEE Transactions on Geoscience and Remote Sensing*, vol. 35, no. 1, pp. 57–67, January 1997.

- [63] U. Narayan, V. Lakshmi, and E. Njoku, “A simple algorithm for spatial disaggregation of radiometer derived soil moisture using higher resolution radar observations,” *2004 IEEE International Geoscience and Remote Sensing Symposium Proceedings*, vol. 3, no. 1, pp. 1877–1879, September 2004.
- [64] G. Vellidis, M. Smith, D. Thomas, and L. Asmussen, “Detecting wetting front movement in a sandy soil with ground-penetrating radar,” *Transactions of the American Society of Agricultural Engineers*, vol. 33, no. 6, pp. 1867–1874, December 1990.
- [65] B. Di Pasquo, E. Pettinelli, G. Vannaroni, A. Di Matteo, E. Mattei, A. De Santis, P. Annan, and D. Redman, “Design and construction of a large test site to characterize the GPR response in the vadose zone,” *2007 4th International Workshop on Advanced Ground Penetrating Radar*, pp. 106–109, June 2007.



## VITA



James Sustman [REDACTED] He attended high school at the Paideia School and graduated in 2003. He received a Bachelor's of Science degree with majors in Mathematics and Physics from Emory University in 2007. He received a Master's of Science in Electrical and Computer Engineering degree from the Georgia Institute of Technology in 2008. He received Honorable Mention in the 2013 IEEE International Symposium on Antennas and Propagation Student Paper Competition. His research interests include broadband ground penetrating radar systems and numerical modeling of antennas.